A 3D Computational Study of Soot Formation in Gasoline Direct-Injection Engines during Transient Operation

Zur Erlangung des akademischen Grades Doktor-Ingenieur (Dr.-Ing.)
Genehmigte Dissertation von Florian Held, M.Sc. aus Bad Schwalbach
Tag der Einreichung: 15.08.2023, Tag der Prüfung: 17.10.2023

1. Gutachten: Prof. Dr.-Ing. Christian Hasse
2. Gutachten: Prof. Dr. tech. Christian Beidl
Darmstadt, Technische Universität Darmstadt

TECHNISCHE
UNIVERSITÄT
DARMSTADT

STFS Simulation of reactive Thermo-Fluid Systems

Mechanical Engineering
Department

A 3D Computational Study of Soot Formation in Gasoline Direct-Injection Engines during Transient Operation

Accepted doctoral thesis by Florian Held, M.Sc.

Date of submission: 15.08.2023
Date of thesis defense: 17.10.2023

Darmstadt, Technische Universität Darmstadt

Bitte zitieren Sie dieses Dokument als:
URN: urn:nbn:de:tuda-tuprints-269708
URL: http://tuprints.ulb.tu-darmstadt.de/26970
Jahr der Veröffentlichung auf TUprints: 2024

Preface / Vorwort

Die vorliegende Dissertationsschrift entstand während meiner Tätigkeit als wissenschaftlicher Mitarbeiter am Fachgebiet Simulation reaktiver Thermo-Fluid Systeme der Technischen Universität Darmstadt unter der Leitung von Prof. Dr.-Ing. Christian Hasse.

Wesentliche Teile der Arbeit wurden im Rahmen des FVV[1]-Forschungsvorhabens 1324 "CFD-Analyse der Partikelbildung während des transienten Motorbetriebs" erarbeitet und durch das Programm zur Förderung der industriellen Gemeinschaftsforschung (IGF 20040 BG) vom Bundesministerium für Wirtschaft und Klimaschutz (BMWK) über die Arbeitsgemeinschaft industrieller Forschungsvereinigungen (AiF) e.V. aufgrund eines Beschlusses des Deutschen Bundestages gefördert.

Weitere Teile dieser Arbeit wurden in folgender Publikation veröffentlicht:

[1] **F. Held**, J. Reusch, S. Salenbauch, and C. Hasse. "A 3D Computational Study of the Formation, Growth and Oxidation of Soot Particles in an Optically Accessible Direct-Injection Spark-Ignition Engine Using Quadrature-Based Methods of Moments". In: *Fuel Processing Technology* 254 (Feb. 2024), p. 107923. DOI: `10.1016/j.fuproc.2023.107923`

Die in dieser Arbeit vorgestellten numerischen Berechnungen wurden auf dem Hochleistungsrechner Lichtenberg der TU Darmstadt durchgeführt. Dieser wird auf Grundlage der Beschlüsse der GWK zum Nationalen Hochleistungsrechnen an Hochschulen (NHR) durch das Bundesministerium für Bildung und Forschung und die am NHR beteiligten Landesregierungen (www.nhr-verein.de/unsere-partner) gefördert.

Softwarelizenzen für die Simulationsumgebung und den Strömungslöser ANSYS® CFX® wurden von Ansys, Inc. im Rahmen des Ansys Academic Partner Programms zur Verfügung gestellt.

---

[1] Forschungsvereinigung Verbrennungskraftmaschinen e.V.

An dieser Stelle möchte ich meinen aufrichtigen Dank an all diejenigen richten, deren Unterstützung und Mitwirkung unerlässlich für die Realisierung dieser Arbeit war:

Zunächst möchte ich meinem Doktorvater, Prof. Dr.-Ing. Christian Hasse, meinen Dank aussprechen. Seine stetige Unterstützung, seine motivierenden Worte und fachlicher Expertise, aber auch seine Beharrlichkeit und Geduld haben diese Arbeit erst ermöglicht. Danken möchte ich außerdem Prof. Dr. Christian Beidl für die Übernahme des Koreferats. Seine konstruktiven Anmerkungen während unseres Forschungsvorhabens waren äußerst wertvoll und haben maßgeblich zur Verbesserung dieser Arbeit beigetragen.

Mein weiterer Dank gilt meinen Projektpartnern. Ich möchte mich bei Christian Riegelbeck für die sehr gute Zusammenarbeit sowohl auf fachlicher als auch menschlicher Ebene bedanken. Viele der Ergebnisse dieser Arbeit basieren auf seinen Messdaten und den gemeinsamen Diskussionen rund um den untersuchten Motor. Ganz besonders möchte ich mich außerdem bei Dr. Wolfgang Bauer bedanken, der mir über den gesamten Zeitraum der Promotion bei softwarebezogenen Fragen als Ansprechpartner zur Seite stand.

Schließlich möchte ich mich bei all meinen Kolleginnen und Kollegen am STFS und RSM bedanken. Die einzigartige Arbeitsatmosphäre mit Input aus den verschiedensten Schwerpunkten, aber auch die vielfältigen Ablenkungen und Aktivitäten, haben meine Promotionszeit unvergesslich werden lassen. Speziell möchte ich die Motorengruppe hervorheben, die mir trotz teils unterschiedlicher Simulationsansätze immer mit Rat und Tat zur Seite stand. Vielen Dank Andrea, Magnus, Jannis, Max und Paul. Ebenso gilt mein Dank Steffen Salenbauch, ohne dessen exzellente Vorarbeit diese Arbeit nicht möglich gewesen wäre. In diesem Zusammenhang möchte ich mich auch bei Robert, Federica und Philipp für ihre geteilte Expertise bei der Modellierung von Rußpartikeln bedanken. Ebenfalls hervorheben möchte ich Hanna und Hendrik, die mich sowohl fachlich als auch moralisch während meiner Zeit am STFS unterstützt haben.

Ein großer Dank gilt außerdem meinen Freunden, die mich stets unterstützt haben, mir immer mit einem offenen Ohr zur Seite standen und während des Promotionsstresses für willkommene Ablenkung sorgten.Ganz besonders möchte ich mich bei Carina bedanken, die sich nicht nur Zeit für die Korrektur dieser Arbeit genommen hat, sondern auch eine wesentliche Stütze in der letzten Phase meiner Promotion war.

Abschließend möchte ich mich bei meiner Familie bedanken, die mich während meines gesamten akademischen Laufbahn und all meinen Entscheidungen bedingungslos unterstützt hat. Vielen Dank für eure Geduld, Rücksichtnahme und uneingeschränkte Unterstützung.

Darmstadt, den 17. Oktober 2023 Florian Held

Zusammenfassung

Feinstaub hat schädliche Auswirkungen auf die Umwelt und die menschliche Gesundheit. Ein wesentlicher Teil der anthropogenen Feinstaubquellen stammt aus dem Verkehrssektor. Aus diesem Grund gelten weltweit gesetzliche Grenzwerte zur Begrenzung der Feinstaubemissionen. Teil der EU-Gesetzgebung ist seit 2017 auch die Prüfung der sogenannten Real Driving Emissions (RDE), also der Emissionen im praktischen Fahrbetrieb auf der Straße. Die Einhaltung der Grenzwerte nach diesen neuen Normen kann nicht nur durch die Optimierung der Partikelemissionen im stationären Motorbetrieb erreicht werden, sondern erfordert auch die Berücksichtigung der Partikelemissionen im hochdynamischen Motorbetrieb. Aus diesem Grund rücken hochdynamische transiente Motorszenarien immer mehr in den Fokus aktueller Forschung und Entwicklung.

Während sich die 3D-CFD (Computational Fluid Dynamics) als Entwicklungswerkzeug in der Motorenentwicklung insbesondere für stationäre Betriebspunkte etabliert hat, wird sie für instationäre Betriebspunkte nur selten oder gar nicht eingesetzt. Dies liegt zum einen an der mangelnden Verfügbarkeit geeigneter Modelle zur Analyse der relevanten Phänomene entlang der gesamten motorischen Wirkkette. Zum anderen sind die für die 3D-CFD notwendigen Randbedingungen in der Regel nicht ausreichend genau charakterisiert. Hinzu kommt der enorm hohe Rechenaufwand bei der Berechnung konsekutiver Motorzyklen.

Nichtsdestotrotz kam es in den vergangenen Jahren zu einer stetigen Weiterentwicklung verfügbarer Methoden und Modelle. Zusammen mit der kontinuierlichen Zunahme der verfügbaren Rechenressourcen ist die 3D-CFD Simulation von instationären Motorszenarien immer greifbarer geworden. In dieser Arbeit soll deshalb demonstriert werden wie mit den aktuell verfügbaren Modellen und Ressourcen die 3D-CFD Simulation zur Analyse der Partikelemissionen in transienten Motorszenarien eingesetzt werden kann.

Hierzu wird zunächst ein vollständiges Framework zur Simulation von Rußpartikelemissionen in einem direkteinspritzenden Verbrennungsmotor vorgestellt. Das Framework, bestehend aus einer Reihe teils motorspezifischer Submodelle, wird um ein detailliertes QMOM (Quadrature Method of Moments) Rußmodell erweitert, um eine genaue Abbildung der Partikelbildungskette zu gewährleisten. Die Evaluierung des Frameworks erfolgt am stationären Betriebspunkt eines optisch zugänglichen Forschungsmotors und auf Basis verfügbarer Rußlumineszenz- und

Extinktionsmessungen. In einem nächsten Schritt wird das Framework für die Simulation von konsekutiven Mehrzyklussimulationen und die Anwendung in transienten Motorszenarios erweitert. Der Fokus liegt dabei auf der genauen Charakterisierung des transienten Szenarios in der virtuellen Motorumgebung. Bestandteile dieser Erweiterung sind die Einführung einer Methodik zur Mittelung multipler Prüfstandsrealisierungen, eine modifizierte 1D-Ladungswechselanalyse zur Berechnung kurbelwinkelaufgelöster Randbedingungen sowie eine Parallelisierungsstrategie zur effizienten Berechnung konsekutiver Motorzyklen. Das erweiterte Framework wird schließlich auf ein RDE-relevantes und rußemissionskritisches transientes Fahrszenario angewendet um die Partikelentstehung zu untersuchen. In einer Wirkungskettenanalyse auf Basis von 30 aufeinanderfolgenden Motorzyklen werden die Ursachen für erhöhte Partikelemissionen identifiziert. Die gewonnenen Erkenntnisse werden anschließend genutzt, um Optimierungspotenziale zu identifizieren.

Zusammenfassend wird in dieser Arbeit ein umfassendes Framework zur Untersuchung der Rußpartikelbildung im transieten Motorbetrieb direkteinspritzender Ottomotoren präsentiert. Das Framework eignet sich in Kombination mit experimentellen Untersuchungen als diagnostisches Werkzeug zur Identifikation und Analyse der Ursachen erhöhten Rußpartikelaufkommens und zur Ableitung von Optimierungspotenzialen individueller Szenarien.

Abstract

Particulate matter has harmful effects on the environment and human health. A significant share of anthropogenic sources of particulate matter originate from the transport sector. For this reason, legal limits are in place worldwide to limit particulate matter emissions. Since 2017, part of the EU legislation includes testing of real driving emissions (RDE), i.e., emissions measured during real-world driving. Compliance with the limits according to these new standards cannot only be achieved by optimizing particulate emissions during stationary engine operation but also requires consideration of particulate emissions during highly dynamic engine operation. Hence, the focus of current research and development is increasingly shifting toward highly dynamic transient engine scenarios.

While 3D Computational Fluid Dynamics (CFD) is an already established design tool for engine development, especially for steady-state operating points, it is rarely or never used for investigating transient engine operation. On the one hand, this is due to the lack of availability of suited models for analyzing the relevant phenomena along the entire engine cause-and-effect chain. On the other hand, the boundary conditions required for 3D-CFD are usually not characterized in sufficient detail. Added to this is the enormously high computational effort required for the calculation of consecutive engine cycles.

Nevertheless, the available methods and models have continuously evolved in recent years. Together with the continuous increase of available computational resources, 3D-CFD simulation of transient engine scenarios is becoming more and more feasible. This paper will therefore demonstrate how, with the currently available models and resources, 3D-CFD simulation can be utilized to analyze particulate emissions in transient engine scenarios.

For this purpose, a complete framework for the simulation of soot particle emissions in a gasoline direct-injection engine is presented. The framework, consisting of a number of engine-specific submodels, is extended by a detailed QMOM (Quadrature Method of Moments) soot model to ensure an accurate representation of the particle formation chain. The framework is first evaluated at the steady-state operating point of an optically accessible research engine and on the basis of available soot luminescence and extinction measurements. In a next step, the framework is extended for the simulation of consecutive multi-cycle simulations and the application in transient engine scenarios. The primary emphasis is placed on the accurate characterization of the transient scenario in the virtual engine environment. Parts of this extension are the introduction of a methodology for averaging data from multiple test bench realizations, a modified 1D gas exchange analysis for calculating crank angle resolved boundary conditions and a parallelization strategy for the efficient calculation of consecutive engine cycles. Finally, the extended framework is applied to an RDE-relevant and soot emission-critical transient driving scenario to study particle formation. A cause-and-effect chain analysis on 30 consecutive engine cycles is performed to identify the root causes of increased particulate emissions. The novel insights gained are then used to identify optimization potential.

In summary, this thesis presents a comprehensive framework for the investigation of soot particle formation in transient engine operation of gasoline direct-injection engines. Combined with experimental studies, the framework is suitable as a diagnostic tool for identifying and analyzing the root causes of increased soot particle generation and deriving optimization potentials of individual scenarios.

Contents

1. Introduction

Particulate matter has harmful effects on the environment and human health. Studies have shown that high concentrations of particulate matter can lead to respiratory and cardiovascular problems, lung cancer, impaired lung function, asthma, and severe mortality [2]. The sources of particulate matter are extremely diverse. In addition to natural origins such as dust drifts, volcanic eruptions, and forest fires, human activities are the primary contributors. These anthropogenic sources include emissions from industrial processes, construction sites, and vehicle exhaust. In this context, the transport sector accounts for a significant share of the anthropogenic source of particulate matter [3]. For this reason, legal limits are in place worldwide to restrict particulate matter emissions.

While diesel engines in particular were known for their high particulate emissions in the past, nowadays gasoline engines also come into the focus of regulations concerning particulate emissions with the advent of direct injection. The current European emission standard for passenger cars (EURO 6d), for example, sets emission limits for both particulate mass and particulate number in the direct-injection gasoline engine [4]. A further tightening of the legal regulations is planned [5].

Since 2017, part of this legislation also includes testing of so-called Real Driving Emissions (RDE), i.e., emissions during practical driving on the road. Compliance with the thresholds according to these new standards can be achieved not only by optimizing particulate emissions in steady-state engine operation but also requires consideration of particulate emissions during highly dynamic engine operation. The associated high complexity of the development process calls for new methods and tools.

1.1. Scientific Questions and Placement of this Work

In recent years, 3D Computational Fluid Dynamics (3D-CFD) has become more and more established in the development process of internal combustion engines. 3D-CFD serves as an efficient method for virtual analysis and optimization. It offers the possibility to gain extended insights into the complex flow and combustion processes inside the engine, which are challenging to access with conventional experimental techniques. Thus, 3D-CFD can be used not only for accompanying analysis and diagnosis but also for cost reduction in the development process through virtual prototyping. These methods are mainly used for the investigation of steady-state operating points. This allows an individual adjustment of single model parameters specifically adapted to the respective operating point. In order to address the issues arising from the current legal situation, there is an initiative to use 3D-CFD methods also for the investigation and optimization of transient operation.

Highly transient engine operation is characterized by sudden changes in the engine's operating conditions. These include rapid load and speed changes, as well as engine cold start [6]. Real driving conditions involve arbitrary combinations and superpositions of all these conditions, making a general characterization very challenging. Engine studies during RDE runs have shown that increased pollutant emissions are detected, especially during these highly transient operating phases. This is due to the rapidly changing transient boundary conditions, which often do not allow the engine to be operated in its optimum state.

To comprehensively study pollutant emissions through 3D-CFD, it's essential to encompass the entire cause-and-effect chain of the engine, as these emissions stem from a complex interplay of numerous preceding processes. This requires detailed models, especially in the context of transient simulations, which allow physical and chemical processes to be correctly represented depending on the transient conditions present. This applies in particular to the modeling of soot particle formation at the end of the cause-and-effect chain and the resulting dependence of all preceding processes. The modeling of soot requires not only an accurate modeling of the underlying gas phase chemistry up to large polycyclic aromatic hydrocarbons but also an accurate description of the polydisperse system of soot particles.

Another challenge of transferring transient engine phenomena into 3D-CFD is the aforementioned characterization of the scenario. Transient engine phenomena are strongly dependent on the existing boundary conditions. Thus, different driving styles, environmental influences, and driving histories can lead to distinct emission characteristics in what would appear to be an identical transient. The quality of the results of the 3D-CFD simulation depends significantly on the quality of these boundary conditions. Ensuring reproducible conditions and compiling a representative set of boundary conditions is therefore essential, albeit difficult, for successfully representing such a scenario in the simulation.

A further difficulty in the simulation of transient engine scenarios is the high computing time. The duration of individual transient engine phenomena can last from a few tenths of a second to several seconds. While such time scales can be handled on the test bench with comparatively little effort, a complete simulation of such a scenario involves the calculation of several hundred consecutive interdependent engine cycles. Typical computation times of just one cycle can range from one day to several weeks, depending on the model selection and geometrical discretization. The resulting computational effort of a consecutive engine simulation is enormous and in most cases exceed the time frame of a project.

The purpose of this work is to address the elaborated problems that exist in the current numerical flow simulation of particulate emissions in transient engine operation. To this extent, three scientific questions are posed, which result from a detailed investigation of the existing challenges:

- Are existing numerical submodels suitable to address current questions in the context of transient engine scenarios?
- How can experimental test bench data be processed and used for the characterization and provision of boundary conditions for 3D-CFD?
- Can 3D-CFD simulations of transient engine operation be successfully applied at a reasonable cost?

These scientific questions serve as a basis for the outline and objective of this work. In order to adequately answer these questions, some crucial topics need to be addressed. These topics are the evaluation of a CFD framework for the simulation of particulate emissions from gasoline direct-injection engines, the adaption of existing methodology for transient engine operation and the application of such an extended methodology for investigating realistic emission-critical events.

In the course of this work, the topics will be examined in detail successively in order to answer the questions posed above. Ultimately, this leads to a better understanding of the numerical simulation of soot formation in gasoline direct-injection engines in transient operation and thus forms the basis for the aim of this work: demonstrating the potential of 3D-CFD simulations as a tool for the targeted analysis of transient engine scenarios.

1.2. Thesis Outline

In **Chapter 2**, an introduction to the fundamentals relevant to this work is given. Starting from the fundamentals of the internal combustion engine, the methods and models of computational fluid dynamics (CFD) relevant in this work are presented, which finally lead to the description and modeling of soot particle emissions.

In **Chapter 3**, the gasoline direct-injection engines investigated numerically in this thesis are described in detail. The chapter starts with the optically accessible research engine at the FAU Erlangen-Nuremberg. The test bench, based on a production engine, was expanded to include a transparent cylinder liner and piston window, enabling optical measurements of soot luminescence and extinction. The second engine considered for transient engine operation investigations is a four-cylinder series production engine from BMW. Transient particulate emission measurements of this engine conducted on the test bench of the Institute for Internal Combustion Engines at TU Darmstadt were provided for this thesis.

In **Chapter 4**, the underlying framework for simulating gasoline direct-injection engines is explained. Particular emphasis is placed on the coupling of a detailed moment-based soot model with the flow solver. The entire methodology is evaluated using available soot luminescence and extinction measurements from the optically accessible research engine.

Next, in **Chapter 5**, the existing methodology for investigating transient engine operation is expanded. The handling of measured boundary conditions is addressed first. To provide these boundary conditions, the existing 1D gas exchange simulation approach for multi-cycle analysis is extended. For the efficient calculation of consecutive transient cycles, a thread-based simulation approach is presented.

Finally, in **Chapter 6**, the methodology for analyzing transient engine operation, combined with the moment-based soot model presented in Chapter 4, is applied to study a “Real Driving Emission” (RDE) relevant transient engine scenario. The conducted combined experimental-numerical analysis allows the identification of emission-critical events and phenomena along the scenario and leads to the derivation of primary measures for emission reduction.

Chapter 7 summarises the results of this work and places them in the context of the scientific questions posed at the beginning. Lastly, the work is concluded with an outlook.

2. Theoretical Background

2.1. Engine Fundamentals

A basic understanding of the processes taking place in the internal combustion engine is necessary for the investigations carried out in this thesis. For this reason, this section first describes the basic functioning of the internal combustion engine. The processes taking place in the combustion chamber as part of the engine cause-and-effect chain are then explained in detail. Finally, various operating strategies of the internal combustion engine are discussed. The nomenclature introduced in this section is used in the following chapters to describe all observed phenomena.

2.1.1. Basic Principles of the Direct-Injection Four-Stroke Engine

The reciprocating internal combustion engine (ICE) is a thermodynamic machine that converts chemical energy into mechanical work in a cyclic process via combustion and heat release. Figure 2.1 (left) provides an overview of the layout of a typical combustion chamber of an ICE, using a gasoline direct-injection engine (GDI) as an example.

A single cylinder of the internal combustion engine consists of the cylinder head (1) with intake (2) and exhaust ports (3), intake (4) and exhaust valves (5), a cylinder liner (9), and a moving piston (10) connected to the crankshaft (13) via a connecting rod (12). Furthermore, the gasoline direct-injection engine is equipped with a fuel injector (6) for the injection of an atomized fuel spray and a spark plug (7) for the ignition of the air-fuel mixture. The basic idea can be described as follows: By drawing in fresh air from the intake port (2) and injecting fuel, a combustible mixture is formed in the combustion chamber (8). After closing all valves and reaching a piston position near the top dead center (TDC), the combustion of the mixture is initiated by the spark plug. The heat release associated with combustion and the resulting increase in pressure in the combustion chamber pushes the piston downwards toward the bottom dead center (BDC) and drives the crankshaft.

The realization of a complete thermodynamic cycle, including gas exchange via the intake and exhaust valves, can be based on the two-stroke or four-stroke principle, with one stroke

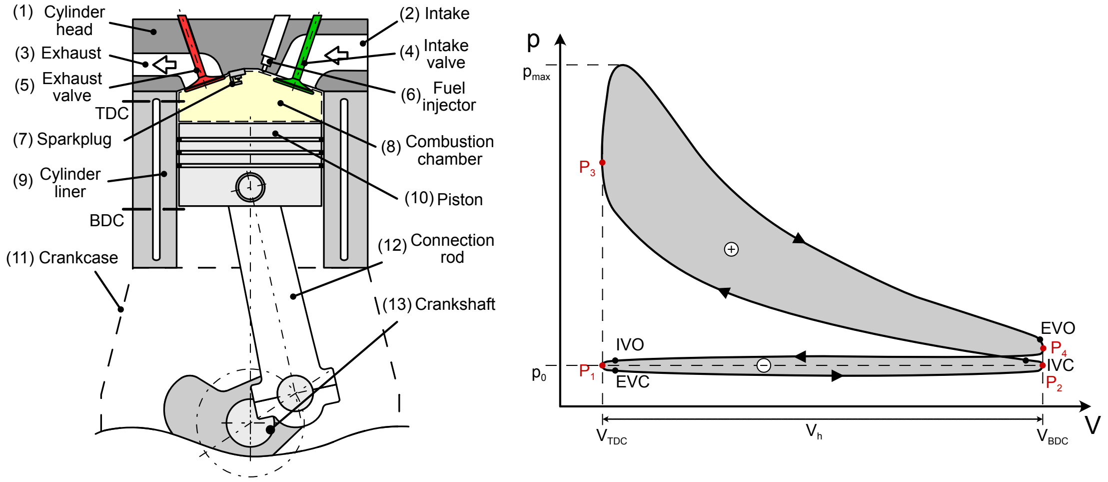

Figure 2.1.: Schematic description of an internal combustion engine cylinder (left) and the corresponding thermodynamic cycle in the p-v diagram (right).

describing the downward/upward movement of the piston, respectively. In the two-stroke principle the entire cycle is thus completed in one crankshaft revolution, while in the four-stroke principle two crankshaft revolutions are required. Although the principle of two-stroke engines allows them to achieve a higher output, the four-stroke principle has prevailed in modern internal combustion engines in the passenger car sector due to its versatility in gas exchange and increasing demands on efficiency and emission behavior. Therefore, the corresponding thermodynamic cycle is shown as an example for a gasoline engine in Figure 2.1 (right) in the pressure-volume (p-V) diagram. The individual strokes along the cycle are briefly explained in the following according to Stone [7]:

P1-P2 **The induction stroke.** Starting from P1 in the p-V diagram, the piston is at the top dead center (TDC) of the cylinder. As the cylinder volume expands, fresh air (charge) is drawn into the cylinder interior through the open intake valve. In gasoline direct-injection engines, fuel is also injected into the cylinder by means of the injector during this stroke and possibly also during the subsequent compression stroke in order to mix with the intake air mass and form a combustible mixture.

P2-P3 **The compression stroke.** The piston has reached the bottom dead center (BDC), the maximum cylinder volume is achieved and the intake valves close (IVC). The air-fuel mixture that was previously drawn in is now compressed. When the top dead center (TDC) is reached, the combustible mixture is ignited using the spark plug. The initiated combustion of the mixture results in a rapid heat release and pressure increase in the combustion chamber.

P3-P4 **The expansion/power stroke.** The high pressure caused by the combustion drives the piston downwards. The volume work performed is transferred in the form of mechanical work by means of the piston and connecting rod to the crankshaft.

P4-P1 **The exhaust stroke.** The maximum cylinder volume is reached again. The exhaust valves are opened (EVO), and the upward-moving piston pushes the burnt residual gas out of the combustion chamber into the exhaust port. At the end of the cycle, a small amount of exhaust gas remains, which is diluted by reopening the intake valves (IVO) in the subsequent cycle and drawing in fresh air.

The total work balance of the cylinder during one engine cycle can be calculated from the work gained, represented by the enclosed area of the high-pressure loop (P2-P4), and the work conducted, represented by the gas exchange loop (P4-P2). A representative measure of the overall work of the cycle is the indicated mean effective pressure (commonly abbreviated as $imep$):

$$imep = \frac{1}{V_d} \oint pdV \,. \tag{2.1}$$

This relates the work of the cylinder to the displacement volume of the cylinder V_d and serves as a relative engine performance measure. The total indicated power of the engine can be calculated in a similar manner as a function of the engine speed n according to:

$$P_i = izn \oint pdV \,, \tag{2.2}$$

where z indicates the number of engine cylinders and i indicates the number of cycles per crankshaft revolution. For a four-stroke engine, i has a value of 0.5 and for a two-stroke engine a value of 1.

On the other hand, brake power describes the usable power delivered by the engine at the crankshaft. It can be calculated based on the torque T at the crankshaft and the engine speed according to:

$$P_b = T2\pi n \,. \tag{2.3}$$

In analogy to equation 2.2, a brake mean effective pressure $bmep$ can be determined from the measured brake power. This is directly proportional to the applied torque and, thus, a measure of the load applied to the cylinder.

To evaluate the fuel consumption of the engine independent of the engine size, the specific fuel consumption sfc is defined as:

$$sfc = \frac{\dot{m}_f}{P_b} \,, \tag{2.4}$$

with $\dot{m}_f$ as the consumed fuel mass flow. The fuel conversion efficiency of the engine η_f is calculated in a similar manner. It is defined as the ratio of benefit to effort, i.e., the ratio of indicated/brake power of the engine to the energy supplied in the form of fuel mass flow $\dot{m}_f$:

$$\eta_f = \frac{P_b}{\dot{m}_f LHV} = \frac{1}{sfc\, LHV}\,, \tag{2.5}$$

where LHV is the lower heating value of the fuel.

2.1.2. The Cause-and-Effect Chain of the Internal Combustion Engine

The thermodynamic machine the internal combustion engine is a highly complex multiphysical system in which a large number of physical phenomena occur and interact with each other. The evaluation and interpretation of engine behavior is considered challenging since the interaction of all phenomena must be taken into account.

Considering a single engine cylinder, the cause-and-effect chain of a gasoline direct-injection engine can be explained in more detail along an engine cycle using Figure 2.2. Starting at the induction stroke (cf. P_1 in Figure 2.1 (right)), fresh air is drawn into the expanding cylinder volume, bypassing the disk-shaped intake valves. The resulting complex flow field is characterized by flow separation at the valve surface and the formation of a subsequent turbulent intake jet. Furthermore, the flow around the valve stems promotes irregularities and vortex shedding. The oblique inflow of the flow at high velocity also induces a large-scale charge movement in the combustion chamber, the so-called tumble motion, which has a significant influence on the subsequent mixture formation in the combustion chamber.

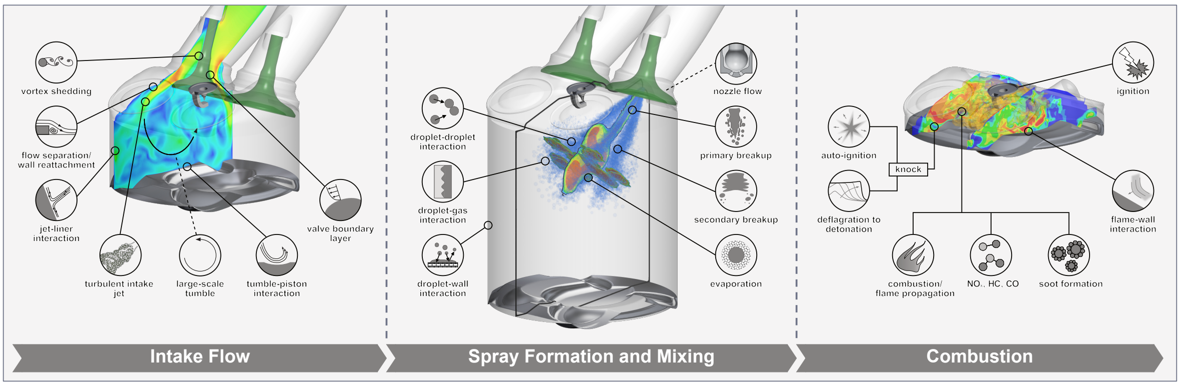

Figure 2.2.: The cause-and-effect chain of a gasoline direct-injection (GDI) engine. The three illustrations depict the representative states during one engine combustion cycle. [8]

In the further course of the engine cycle, fuel is injected into the domain, the intake valves close and the charge is compressed. Fuel injection and spray breakup depend on injector geometry, calibration and other operating conditions and occupy a separate subfield of engine research. By means of primary and secondary breakup mechanisms [9], the injected liquid fuel jet breaks down into a size distribution of small spray droplets which, depending on the ambient conditions, evaporate into the gas phase or hit the cylinder or piston surface (spray-wall interaction). The potential formation of liquid wall films and their local evaporation has a significant influence on the homogenization of the air-fuel mixture and can, in the worst case, lead to pyrolysis of the liquid wall film and locally increased soot particle formation [10], often referred to as pool fire. The homogenization of the mixture within the remaining engine cycle is thereby essentially dependent on turbulent mixing and the kinetic energy of the tumble motion. Furthermore, the direct injection of fuel into the combustion chamber results in a cooling of the cylinder charge and thus has a positive impact on the performance of the engine. In conclusion, the local distribution of the mixture has a significant influence on the combustion and subsequential pollutant formation inside the cylinder.

Ignition and flame propagation are highly dependent on the local flow field, degree of turbulence and the mixture ratio present. In the case of the GDI engine, the ignition of the mixture is initiated by the spark plug. The flame propagation speed, resulting reaction products, and heat release depend on local conditions, charge motion, pressures, temperatures, and mixture ratios inside the cylinder and are thus closely coupled to the preceding phenomena. In the case of high compression ratios and in-cylinder pressures, as well as insufficient charge air cooling, knocking (spontaneous ignition of local centers in front of the flame front) may also occur.

Resulting emissions such as NO_x or particulate emissions also vary depending on fuel, temperature and local air-fuel mixture composition. NO_x emissions typically occur in regions of lean combustion and high temperatures [11], while particulate emissions are particularly formed in rich air-fuel mixtures and incomplete combustion [11]. The different formation mechanisms oppose each other in the so-called Soot-NO_x trade-off since the reduction of one emission type can often only be achieved at the expense of increasing other emission types.

2.1.3. Operating Modes of an Internal Combustion Engine

A wide range of control parameters allows the gasoline direct-injection engine to be optimized with regard to various target parameters. In addition to properties such as high engine performance and good dynamic response, the main focus today is on low fuel consumption and minimum pollutant emissions [12].

Various combustion modes can be used to adjust to the operating point. The most widespread combustion modes in the GDI engine are *homogeneous combustion* and *stratified combustion*. Homogeneous combustion aims to burn a homogeneous mixture in the combustion chamber under stoichiometric conditions ($\lambda = 1$). To achieve this, the fuel is injected as early as possible during the intake stroke to ensure a sufficiently long period for mixture formation. Under ideal conditions, the fuel burns as cleanly as possible and low pollutant emissions can be achieved. For this, the amount of injected fuel and the air required must be adjusted to each other depending on the operating point. In part-load operation, where a lower energy output is required, the available air flow must therefore be reduced for homogeneous operation. This is typically achieved by either throttling the intake mass flow or manipulating the valve timing, with the former typically resulting in a loss of efficiency.

Stratified operation, on the other hand, aims to provide an ignitable mixture only in a reduced region of the combustion chamber. To this end, fuel is injected into the combustion chamber late in the compression stroke in order to generate a stoichiometric mixture in the region of the spark plug at the time of ignition. In the part-load range, this process makes it possible to largely avoid throttling the intake air, reduce losses and achieve globally lean combustion.

In addition to strict homogeneous and stratified operation, there are combinations of both modes as well as special modes of operation, such as *homogeneous stratified operation*, *homogeneous split mode* and *catalyst heating*. These modes are sometimes very complex and, like catalyst heating, for example, represent only a temporary mode of operation [13].

In the following, the influence of further operating parameters on engine combustion and pollutant formation is briefly discussed before an explicit look is taken at the influence on raw in-cylinder emissions.

Valve timing

Depending on the installed systems, both the amplitude of the valve lift and the position of the valve lift curve relative to the engine cycle can be adjusted to manipulate the cylinder charge. By overlapping both valve opening phases, the residual gas content in the combustion chamber can be varied (internal exhaust gas recirculation (EGR)) or the effective compression ratio can be changed (cf. Miller/Atkinson cycle). By reducing the maximum intake valve lift at part-load, flow losses due to throttling that would otherwise be required can be avoided. Additional swirl can be introduced into the in-cylinder flow by so-called *phasing*, i.e. different or delayed opening of the two intake valves, in order to improve air-fuel homogenization in low load ranges.

Fuel injection

The timing, duration and quantity of fuel injection have a significant impact on the mixture preparation/homogenization and charge stratification. Early injection in the intake stroke gives the mixture sufficient time to homogenize. However, due to the small combustion chamber volume at the time of injection, there is also an increased interaction of the fuel spray with the combustion chamber walls. In particular during the start-up phase of the engine and with cold cylinder walls, this can lead to the formation of long-lasting wall films and thus to pool fire and increased soot formation. Late fuel injection has the advantage of charge cooling due to fuel vaporization and thus a reduction of the risk of knocking.

Ignition timing shift

The ignition timing defines the start of the combustion. Its position in the compression-expansion cycle thus has a significant influence on efficiency as well as on the thermo-chemical conditions during combustion. An as early as possible ignition and flame propagation around the top dead center typically shows the highest efficiency. However, the risk of knocking combustion also increases with the associated high pressure and temperatures. The use of a knock sensor allows the engine to be operated at optimal ignition angles and therefore to be controlled as close to the knock limit as possible.

Influence of the operating conditions on the internal engine emission behavior

Unburnt hydrocarbons (HC) and carbon monoxide (CO) emissions are caused by incomplete combustion in the combustion chamber. Incomplete oxidation occurs, due to a lack of oxygen, especially in zones with a rich air-fuel mixture, but can also be caused by flame quenching near cold combustion chamber walls. High temperatures and thin quenching zones as well as high exhaust temperatures and the resulting post-reactions of the species contribute to a reduction of these emissions. The lowest emissions of HCs occur in the range of $\lambda = 1.05...1.2$. CO shows a linear increase with a decrease of λ below stoichiometry [14].

Nitrogen oxide emissions (NO_x) occur mainly at high combustion temperatures and a slight excess of air. For particularly rich and particularly lean fuel-air ratios, the emission potential decreases as lower combustion temperatures usually prevail. In the stratified combustion mode, the emissions are low compared to $\lambda = 1$ as only a part of the charge participates in the combustion. Nevertheless, a 3-way catalyst cannot convert the occurring NO_x emissions due to the excess air in this operation mode, which is why additional exhaust technology, such as storage catalysts, is required [14].

Due to its typically stoichiometric mode of operation, the gasoline engine usually exhibits only low **particulate emissions**. However, local inhomogeneities of the mixture, caused by insufficient mixture preparation, can have a significant influence on the formation of potential particulate emissions. Particularly critical in this regard is the wetting of component surfaces with a liquid fuel film. This especially occurs at low component temperatures, leading to slow local evaporation and the occurrence of diffusive combustion and pool fire. Highly complex operating modes such as those that occur in gasoline direct-injection engines are particularly affected by increased particulate emissions due to their susceptibility to mixture preparation by a variety of disturbances, especially in dynamic operation.

2.2. Fundamentals of Computational Fluid Dynamics (CFD)

This section gives an overview of the equations, modeling approaches and conventions in computational fluid dynamics (CFD) relevant to this work. Since internal combustion engine simulations combine a large number of physical phenomena, this section does not only cover the relevant equations for the cold flow but also specific modeling approaches for the injection of liquid particles and premixed combustion in technical applications.

2.2.1. Governing Equations

In the following, we first take a look at the conservation equations relevant for the description of reacting multicomponent flows as well as the treatment of thermodynamic properties and transport coefficients.

Conservation of mass

The conservation of mass is given by

$$\frac{\partial \rho}{\partial t} + \frac{\partial \left(\rho u_i\right)}{\partial x_i} = \dot{S}_m \,, \tag{2.6}$$

where ρ describes the gas density and u_i the velocity in i direction. The source term $\dot{S}_m$ takes into account mass change, e.g., due to phase change during evaporation of liquid fuel droplets.

Conservation of momentum

Analogously, the conservation of momentum is given by

$$\frac{\partial \left(\rho u_i\right)}{\partial t} + \frac{\partial \left(\rho u_i u_j\right)}{\partial x_j} = \frac{\partial \tau_{ij}}{\partial x_j} - \frac{\partial p}{\partial x_i} + \rho g_i + \dot{S}_{u,i} \,, \tag{2.7}$$

where p is the pressure and τ_{ij} the viscous stress tensor. Besides temporal change and convective transport of momentum, additional forces are considered on the right-hand side of the equation in terms of viscous and pressure forces. Moreover, external volume forces ρg_i, e.g. due to gravity, are included in the equation. In most cases, however, these can be neglected. The term $\dot{S}_{u,i}$ includes the momentum exchange with other phases, e.g. liquid fuel droplets. The viscous stress tensor τ_{ij} is fluid-dependent. For Newtonian fluids it can be defined as:

$$\tau_{ij} = 2\mu S_{ij} - \frac{2}{3}\mu\delta_{ij}\frac{\partial u_k}{\partial x_k} \quad \text{with} \quad S_{ij} = \frac{1}{2}\left(\frac{\partial u_i}{\partial x_j} + \frac{\partial u_j}{\partial x_i}\right) , \tag{2.8}$$

where S_{ij} is the rate of strain tensor and μ the dynamic viscosity. The second term describes the isotropic compression/expansion of the fluid and appears only for compressible fluids. The expression δ_{ij} is defined as unity for $i = j$, zero otherwise, and is often referred to as the *Kronecker delta* in literature.

Species Balance

The description of multicomponent systems requires not only the mass and momentum balance but also the description of the local species composition. For this purpose, an additional differential equation can be solved for the mass fraction of each species Y_k in the mixture:

$$\frac{\partial\left(\rho Y_k\right)}{\partial t} + \frac{\partial\left(\rho u_j Y_k\right)}{\partial x_j} = -\frac{\partial\left(\rho Y_k V_{k,j}\right)}{\partial x_j} + \dot{\omega}_k + \dot{S}_{m,k} , \tag{2.9}$$

where $V_{k,j}$ describes the diffusion velocity of the species k in the mixture. The additional source terms on the right-hand side account for the change in species due to a chemical reaction ($\dot{\omega}_k$) and the change due to a phase change ($\dot{S}_{m,k}$), respectively.

Conservation of energy

The conservation of energy is usually expressed in terms of enthalpy. The specific enthalpy h is defined as the sum of specific internal energy e and the product of pressure and specific volume:

$$h = e + \frac{p}{\rho} . \tag{2.10}$$

For multicomponent fluids with N_c species, it can be constructed from the enthalpies of each species k according to:

$$h = \sum_{k=1}^{N_c} h_k Y_k = \sum_{k=1}^{N_c}\left(\int_{T_0}^{T} c_{p,k}\, dT + \Delta h^0_{f,k}\right) Y_k . \tag{2.11}$$

The first term on the right-hand side of the equation is referred to as the sensible enthalpy and quantifies the change in temperature. The second term accounts for the energy needed to form the molecules of the species k. The specific total enthalpy used in this work additionally considers the kinetic energy $h_t = h + \frac{1}{2}u_i u_i$. A conservation equation for h_t can be constructed as follows:

$$\frac{\partial\left(\rho h_t\right)}{\partial t}-\frac{\partial p}{\partial t}+\frac{\partial\left(\rho u_j h_t\right)}{\partial x_j}=-\frac{\partial q_j}{\partial x_j}+\frac{\partial \tau_{ij} u_i}{\partial x_j}+\dot{S}_{h_t}\,. \tag{2.12}$$

In this equation, $\dot{S}_{h_t}$ describes external heat sources (not to be confused with combustion). The term $\tau_{ij}\partial u_i/\partial x_j$ accounts for the work due to viscous stresses and is usually neglected. The energy flux in this equation q_j is composed of a heat diffusion expressed by Fourier's law ($\lambda\partial T/\partial x_j$) and the individual diffusion of species with different enthalpies:

$$q_j=-\lambda\frac{\partial T}{\partial x_j}+\rho\sum_{k=1}^{N_c} h_k Y_k V_{k,j}\,. \tag{2.13}$$

The term $V_{k,j}$ describes the diffusion velocity of species k. For multicomponent systems, these velocities are extremely difficult to calculate, so assumptions and models are often used. In this work, the unity Lewis number assumption is applied. Under the condition of equal diffusivities for all species, the diffusion velocity can be described by means of Fick's law and a diffusion coefficient. For a Lewis number of one, the species diffusion coefficient is $Le_k=\lambda/(c_p\rho D_k)=1$, with the species diffusivity D_k, resulting in the following for the diffusion velocity

$$V_{k,j}=-D_k\frac{1}{Y_k}\frac{\partial Y_k}{\partial x_j}\quad\text{or}\quad Y_k V_{k,j}=-\frac{\lambda}{\rho c_p}\frac{\partial Y_k}{\partial x_j}\,. \tag{2.14}$$

The unity Lewis number assumption is widely used in combustion modeling. However, for fuels prone to differential diffusion, such as hydrogen, other assumptions must be used. Finally, the conservation equation for total enthalpy can be summarized as follows:

$$\frac{\partial\left(\rho h_t\right)}{\partial t}-\frac{\partial p}{\partial t}+\frac{\partial\left(\rho u_j h_t\right)}{\partial x_j}=\frac{\partial}{\partial x_j}\left(\frac{\lambda}{c_p}\frac{\partial h}{\partial x_j}\right)+\dot{S}_{h_t}\,. \tag{2.15}$$

Transport coefficients and thermodynamic properties

In order to evaluate the given equations, the transport coefficients of the mixture have to be characterized first. They can be determined from the mass fraction-weighted values of the individual components to:

$$\mu=\sum_{k=1}^{N_c}\mu_k Y_k\quad\text{and}\quad\lambda=\sum_{k=1}^{N_c}\lambda_k Y_k\,. \tag{2.16}$$

The heat capacity at constant pressure c_p for the mixture can be determined in the same way from the heat capacities of the individual components:

$$c_p = \sum_{k=1}^{N_c} c_{p,k} Y_k \,. \tag{2.17}$$

The individual heat capacities of each component are temperature dependent and can be approximated from NASA polynomials [15]. The coefficients used in this work are taken from the Chemkin Thermodynamic Database [16].

Eventually, the law of ideal gases is utilized to close the system of equations. It describes the state of the thermodynamic system according to:

$$p = \rho \frac{R}{W} T \,, \tag{2.18}$$

with $R = 8.314\,\mathrm{J/K/mol}$ denoting the universal gas constant and W denoting the molecular weight of the ideal mixture. Again, the molar mass of the mixture can be calculated based on the mass fraction of every component of the mixture applying:

$$\frac{1}{W} = \sum_{k=1}^{N_c} \frac{Y_k}{W_k} \,. \tag{2.19}$$

2.2.2. Turbulence Modeling

For turbulence modeling, an Unsteady Reynolds Averaged Navier Stokes (URANS) approach is used in this work. This approach solves the Navier-Stokes equation for averaged quantities instead of the exact and instantaneous solutions. Furthermore, for compressible flows, a mass-weighted average (Favre-average) $\widetilde{\phi}$ is used:

$$\widetilde{\phi} = \frac{\overline{\rho \phi}}{\overline{\rho}} \quad \text{with} \quad \overline{\phi}(x_i) = \lim_{t \to \infty} \frac{1}{T} \int_0^T \phi(x_i, t) dt \,. \tag{2.20}$$

In this expression, the overline denotes the mean quantity and the tilde denotes the mass-weighted average. Using the Favre-average, the quantity can be decomposed similarly to the classic Reynolds decomposition by:

$$\phi = \widetilde{\phi} + \phi'' \quad \text{with} \quad \widetilde{\phi''} = 0 \,. \tag{2.21}$$

Introducing this formalism to the Navier-Stokes, species and energy equations yields:

$$\frac{\partial \overline{\rho}}{\partial t} + \frac{\partial \overline{\rho} \widetilde{u}_j}{\partial x_j} = 0 \,, \tag{2.22}$$

$$\frac{\partial \bar{\rho}\widetilde{u}_i}{\partial t} + \frac{\partial \bar{\rho}\widetilde{u}_i\widetilde{u}_j}{\partial x_j} = -\frac{\partial \bar{p}}{\partial x_i} + \frac{\partial}{\partial x_j}\left(\bar{\tau}_{ij} - \bar{\rho}\widetilde{u''_i u''_j}\right) , \tag{2.23}$$

$$\frac{\partial \bar{\rho}\widetilde{Y}_k}{\partial t} + \frac{\bar{\rho}\widetilde{Y}_k\widetilde{u}_j}{\partial x_j} = \frac{\partial}{\partial x_j}\left(\overline{\rho D_k \frac{\partial Y_k}{\partial x_j}} - \bar{\rho}\widetilde{Y''_k u''_j}\right) + \dot{\bar{\omega}}_k + \dot{\bar{S}}_{m,k} , \tag{2.24}$$

$$\frac{\partial \bar{\rho}\widetilde{h}_t}{\partial t} - \frac{\partial \bar{p}}{\partial t} + \frac{\bar{\rho}\widetilde{h}_t\widetilde{u}_j}{\partial x_j} = \frac{\partial}{\partial x_j}\left(\overline{\frac{\lambda}{c_p}\frac{\partial h}{\partial x_j}} - \bar{\rho}\widetilde{h''_t u''_j}\right) + \dot{\bar{S}}_{h_t} . \tag{2.25}$$

Compared to the system of equations of instantaneous quantities 2.6, 2.7, 2.9 and 2.15, the application of the averaging operation introduces a number of new unclosed terms that require modeling.

The averaged molecular diffusion terms of both scalar transport equations for species and enthalpy are usually approximated by the averaged gradient [17]:

$$\overline{\rho D_\phi \frac{\partial \phi}{\partial x_j}} = \bar{\rho}\overline{D_\phi}\frac{\partial \widetilde{\phi}}{\partial x_j} , \tag{2.26}$$

where ϕ is an arbitrary transported scalar.

Other unclosed terms arise from the nonlinearity of the convective transport. The term $-\bar{\rho}\widetilde{u''_i u''_j}$ in the momentum equation is the Reynolds stress tensor. In addition to approaches to describe the tensor by means of its separate differential equation, a modeling of the tensor in analogy to the molecular stress tensor has become established. In the turbulent viscosity hypothesis also called the Boussinesq hypothesis, the deviatoric part of the Reynolds stress tensor is modeled proportionally to the deviatoric mean rate of strain tensor:

$$\bar{\rho}\widetilde{u''_i u''_j} - \frac{2}{3}\bar{\rho}\delta_{ij}k = -\mu_t\left(\frac{\partial \widetilde{u}_i}{\partial x_j} + \frac{\partial \widetilde{u}_j}{\partial x_i} - \frac{2}{3}\delta_{ij}\frac{\partial \widetilde{u}_k}{\partial x_k}\right) . \tag{2.27}$$

The isotropic part of the Reynolds stress tensor contains the definition of the turbulent kinetic energy k, which is:

$$k = \frac{1}{2}\widetilde{u''_i u''_i} . \tag{2.28}$$

A close examination of equation 2.27 shows that the effect of the turbulent stresses can also be interpreted as a diffusive force with an unknown turbulent viscosity μ_t. This means that the effect of mixing caused by convective transport in turbulent eddies is replaced by an artificial increase of diffusivity. The combination of both molecular viscosity and turbulent viscosity is often referred to as effective viscosity:

$$\mu_{eff} = \mu + \mu_t \, . \tag{2.29}$$

A similar approach can be applied to every other scalar quantity. The gradient assumption for the enthalpy-velocity correlation and species-velocity correlation follows:

$$\overline{\rho}\widetilde{h_t'' u_j''} = -\frac{\mu_t}{Pr_t}\frac{\partial \widetilde{h}_t}{\partial x_j} \quad \text{and} \quad \overline{\rho}\widetilde{Y_k'' u_j''} = -\frac{\mu_t}{Sc_t}\frac{\partial \widetilde{Y}_k}{\partial x_j} \, , \tag{2.30}$$

where Pr_t is the turbulent Prandtl number and Sc_t the turbulent Schmidt number. In this work, both values were set to 0.9.

To finally close the system of equations, a model for μ_t has to be provided. Several modeling approaches for the description of μ_t, from algebraic expressions up to the deployment of additional transport equations, are available. The most common category of models are the two-equation models. These models provide a good balance between accuracy and numerical effort.

2-equation modeling approach

In this work, the Menter Shear-Stress-Transport (SST) model [18] is used. This two-equation model combines two independent models, the standard $k-\varepsilon$ model [19] and the Wilox $k-\omega$ model [20], to overcome their respective drawbacks. While the $k-\omega$ model has its advantage in the near wall region, the $k-\varepsilon$ model provides better freestream sensitivity [21]. The SST model applies further adaption for the improvement of the prediction of flow separation at smooth surfaces.

Both models are based on the transport equation of turbulent kinetic energy k and one additional characteristic turbulent quantity, the turbulent dissipation rate ε or the turbulent frequency ω. With the help of the relation $\omega \propto \varepsilon/k$, the two equations for ε and ω can be blended into each other. The transport equations for k and for ω in the SST model are as follows:

$$\frac{\partial\left(\overline{\rho}k\right)}{\partial t} + \frac{\partial\left(\overline{\rho}k\widetilde{u}_j\right)}{\partial x_j} = \frac{\partial}{\partial x_j}\left[\left(\mu + \frac{\mu_t}{\sigma_{k3}}\right)\frac{\partial k}{\partial x_j}\right] + P_k - \beta^*\overline{\rho}k\omega \, , \tag{2.31}$$

$$\frac{\partial\left(\overline{\rho}\omega\right)}{\partial t} + \frac{\partial\left(\overline{\rho}\widetilde{u}_j\omega\right)}{\partial x_j} = \frac{\partial}{\partial x_j}\left[\left(\mu + \frac{\mu_t}{\sigma_{\omega 3}}\right)\frac{\partial \omega}{\partial x_j}\right] + \left(1-F_1\right)2\overline{\rho}\frac{1}{\sigma_{\omega 2}\omega}\frac{\partial k}{\partial x_j}\frac{\partial \omega}{\partial x_j} + \alpha_3\frac{\omega}{k}P_k - \beta_3\overline{\rho}\omega^2 \, . \tag{2.32}$$

The transport equation for k can be directly derived from the momentum equation. Herein, the turbulent flux is modeled using a gradient assumption (cf. eq. 2.30). The production of turbulent kinetic energy is included with P_k. This term is dependent on the Reynolds stress tensor and can be modeled using the Boussinesq approximation (cf. eq. 2.27). The last term on the right-hand side describes the dissipation rate and is a direct result of the ε-ω relation $\varepsilon = \beta^* \overline{\rho} k \omega$.

The ω-equation follows the generic form of a transport equation. Production and dissipation of the turbulent frequency are modeled proportionally to the k-equation. The second term on the right-hand side is responsible for the blending between the ε and ω formulation of the model. The blending function F_1 is defined as:

$$F_1 = \tanh\left(arg_1^4\right) \tag{2.33}$$

with

$$arg_1 = \min\left(\max\left(\frac{\sqrt{k}}{\beta^* \omega y}; \frac{500\mu}{y^2 \omega \overline{\rho}}\right); \frac{4\overline{\rho}k}{CD_{kw}\sigma_{\omega 2} y^2}\right) \tag{2.34}$$

and

$$CD_{k\omega} = \max\left(2\overline{\rho}\sigma_{\omega 2}\frac{1}{\omega}\frac{\partial k}{\partial x_j}\frac{\partial \omega}{\partial x_j}; 10^{-20}\right) . \tag{2.35}$$

The function F_1 is equal to one near the surface and decreases to zero outside the boundary layer. The distance to the wall y contributes directly to the argument of the blending function. The model parameters of the SST model are blended between ω and ε formulation according to:

$$\phi_3 = F_1 \phi_1 + (1 - F_1)\, \phi_2 \,, \tag{2.36}$$

where ϕ is an arbitrary model parameter. Table 2.1 contains a complete list of the model parameters of the SST model.

Table 2.1.: Model parameter of the SST turbulence model

$k - \omega$ formulation	$\sigma_{k1} = 2$	$\sigma_{\omega 1} = 2$	$\alpha_1 = 5/9$	$\beta_1 = 0.075$
$k - \varepsilon$ formulation	$\sigma_{k2} = 1$	$\sigma_{\omega 2} = 1/0.856$	$\alpha_2 = 0.44$	$\beta_2 = 0.0828$
Additional constants	$a_1 = 0.31$	$\beta^* = 0.09$	$\kappa = 0.41$	

The construction of the turbulent viscosity μ_t takes place via dimensional analysis of k and ω. In its simplest form it follows $\mu_t = \overline{\rho}\frac{k}{\omega}$. However, the formulation in the SST model in eq. 2.37 is adapted to improve the model behavior in predicting flow separation from smooth surfaces.

$$\frac{\mu_t}{\overline{\rho}} = \frac{a_1 k}{\max\left(a_1 \omega; S F_2\right)} \quad \text{with} \quad S = \sqrt{S_{ij} S_{ij}} \,. \tag{2.37}$$

The limiter in the denominator of the formulation contains the invariant measure of the strain rate S and the blending function F_2 similar to F_1. In this way, the model satisfies Bradshaw's assumption of proportionality of the turbulent shear stress with the turbulent kinetic energy k near the wall [18]. Effectively, an overestimation of the turbulent viscosity is prevented, and correct flow separation is predicted. The blending function F_2 is defined as

$$F_2 = \tanh\left(arg_2^4\right) \tag{2.38}$$

with

$$arg_2 = \max\left(\frac{2\sqrt{k}}{\beta^*\omega y}; \frac{500\mu}{y^2\omega\overline{\rho}}\right) . \tag{2.39}$$

It becomes unity in the near wall region and decreases with distance to the wall.

2.2.3. Spray Modeling

The consideration of fuel injection in 3D-CFD engine simulations requires the additional modeling of a dispersed liquid phase in the system. The dispersed phase is calculated in this work using a Lagrangian particle approach. Here, each fuel droplet is transported through the domain as a mass point and its velocity is influenced by forces acting from outside. During its course, the mass point can lose weight due to the evaporation of the droplet.

To avoid having to individually track the immense number of fuel particles occurring during injection, a reduced number of stochastic particles, so-called parcels, are transported in their place. Each parcel represents a set of individual fuel droplets with identical behavior and properties and is modeled analogously to a single droplet. In sum, the parcels reproduce the number density function of the entirety of the individual droplets of the fuel spray.

The motion of each parcel can be described according to:

$$m_p \frac{du_{p,i}}{dt} = F_{R,i} + F_{BA,i} + F_{B,i} + F_{D,i} + F_{VM,i} + F_{P,i} \tag{2.40}$$

with the mass of the parcel m_p and its velocity $u_{p,i}$ including rotational forces (coriolis and centripetal forces) $F_{R,i}$, the Basset force $F_{BA,i}$, the buoyancy force $F_{B,i}$, the drag forces $F_{D,i}$, the virtual mass force $F_{VM,i}$ and the pressure gradient force $F_{P,i}$.

In the context of this work, rotational forces and buoyancy forces can be neglected. Virtual mass and pressure forces can also be neglected since the fuel density is significantly larger than the gas phase density. The Basset force is not included in the used flow solver and is therefore also neglected in this work. Eventually, the equation reduces to:

$$m_p \frac{du_{p,i}}{dt} = F_{D,i} = m_p \frac{C_D}{\tau_p} \frac{Re_p}{24} u_{s,i} \quad \text{with} \quad u_{s,i} = u_{g,i} - u_{p,i} \, , \tag{2.41}$$

where the drag force can be described dependent on the drag coefficient C_D, a characteristic particle time scale τ_p, the particle Reynolds number Re_p and a slip velocity $u_{s,i}$ as the difference between gas phase velocity $u_{g,i}$ and particle velocity $u_{p,i}$. The particle Reynolds number is also expressed with the slip velocity as velocity scale and the parcel diameter d_p as length scale according to:

$$Re_p = \frac{|u_{s,i}| d_p \rho_g}{\mu_g} \tag{2.42}$$

with ρ_g and μ_g as gas phase density and dynamic viscosity. The particle time-scale is calculated as:

$$\tau_p = \frac{\rho_p {d_p}^2}{18 \mu_g} \,. \tag{2.43}$$

The drag coefficient is calculated with the Schiller-Naumann correlation [22]:

$$C_D = \max\left(\frac{24}{Re_p} \left(1 + 0.15\, {Re_p}^{0.687}\right) ; 0.44 \right) \,, \tag{2.44}$$

where the limiter of 0.44 guarantees a constant coefficient in the inertial regime for Reynolds numbers above $Re_p > 1000$.

Liquid evaporation model

The liquid droplet evaporation in this work is modeled regime-dependent for boiling and non-boiling conditions. Under which conditions evaporation takes place is dependent on the vapor pressure of the droplet composition. The vapor pressure for each component of the droplet is dependent on the particle temperature T_p and can be calculated using the Antoine equation:

$$\log_{10}\left(p_{vap,k}^{pure}(T_p)\right) = A_k - \frac{B_k}{T_p - C_k} \,, \tag{2.45}$$

where A_k, B_k and C_k are the Antoine model coefficients for the respective component k. The total vapor pressure p_{vap} for the droplet composition is a combination of vapor pressures of all components weighted with the component mole fraction X_k^L in the liquid phase:

$$p_{vap} = \sum_k^{N_c} X_k^L p_{vap,k}^{pure}(T_p) \,. \tag{2.46}$$

The evaporation regime is determined depending on the ratio of total vapor pressure to ambient pressure:

$$\begin{aligned} p_{vap} &\geq p_{ambient} && : \text{boiling regime} \\ p_{vap} &< p_{ambient} && : \text{non-boiling regime} \end{aligned}$$

Boiling regime

Evaporation in the boiling regime is driven by convective heat transfer Q_{conv} and the required latent heat for evaporation of each component $\Delta h_{v,k}$. It can be calculated as follows:

$$\frac{dm_p}{dt} = -\frac{Q_{conv}}{\sum_k^{N_c} X_{s,k}^V \Delta h_{v,k}} \,, \tag{2.47}$$

with a convective heat transfer

$$Q_{conv} = \pi d_p \lambda_g \, Nu \, (T_g - T_p) \ . \tag{2.48}$$

Herein, d_p describes the droplet diameter, λ_g the thermal conductivity of the surrounding gas phase and T_p and T_g the temperatures of the droplet and the gas phase, respectively. The Nusselt number Nu in this equation can be determined using the Ranz-Marshall correlation [23]:

$$Nu = 2 + 0.6 \, Re_p{}^{0.5} \left(\mu \frac{c_p}{\lambda}\right)_g^{1/3} \ . \tag{2.49}$$

The required latent heat for evaporation is obtained by the sum of the weighted latent heat of each species in the droplet. For this, the applied equilibrium vapor mole fraction at the droplet surface $X_{s,k}^V$ can be calculated according to Raoult's law:

$$\frac{p_{vap,k}}{p_{vap}} = \frac{X_k^L p_{vap,k}^{pure}}{p_{vap}} = X_{s,k}^V \, . \tag{2.50}$$

The evaporation rate for each component can be calculated from the total evaporation rate as follows:

$$\frac{dm_{p,k}}{dt} = X_{s,k}^V \frac{dm_p}{dt} \, . \tag{2.51}$$

Non-boiling regime

For ambient pressures above the total vapor pressure, the particles evaporate in a diffusion regime. The mass transfer in the diffusion regime can then be described as:

$$\frac{dm_p}{dt} = \sum_k^{N_c} \frac{dm_{p,k}}{dt} = \sum_k^{N_c} \pi d_p \rho D_k \, Sh \frac{W_{c,k}}{W_g} ln \left(\frac{1 - X_{s,k}^V}{1 - X_k^V}\right) \,, \tag{2.52}$$

where $W_{c,k}$ is the molecular weight of the vapor of component k and W_g is the molecular weight of the mixture in the continuum phase. X_k^V is the mole fraction of the vapor of component k in the continuum phase. The equilibrium vapor mole fraction of component k at the droplet surface is given for the diffusion regime by:

$$X_{s,k}^V = \frac{p_{vap,k}}{p_{ambient}} \,. \tag{2.53}$$

Furthermore, the mass transfer is dependent on the Sherwood number Sh. The Sherwood number can be calculated in analogy to the Nusselt number correlation as follows:

$$Sh = 2 + 0.6\, {Re_p}^{0.5} \left(\frac{\mu}{\rho D} \right)^{1/3} \,. \tag{2.54}$$

Spray Wall Interaction

A particularly important role in engine simulation is given to the interaction between fuel spray and cylinder and piston walls. Especially at very early or very late injection times and correspondingly very high piston positions in the cylinder, but also at large injected fuel quantities, it is not unlikely that the spray cone will hit a surface.

The processes involved depend on the wall temperature, the wall surface and roughness, the angle of impact, the impact velocity of the particle, the presence of a wall film, and a number of other parameters.

In this work, the Elsässer model implemented in ANSYS® CFX® is used for the treatment of spray-wall interaction [24, 25]. The approach is based on Bai and Gosmann's regime classification [26] and the introduction of two limiting temperatures, the *pure adhesion* temperature T_{pA} and the *pure rebound* temperature T_{pR}, to distinguish between three regimes:

Table 2.2.: Regime classification in the Elsässer model.

Regime	**Wall temperature range**
Cold wetting (CW) Cold wall with wall film	$T_{wall} \leq T_{pA}$
Hot wetting (HW) Hot wall with wall film	$T_{pA} < T_{wall} \leq T_{pR}$
Hot non-wetting (HNW) Hot wall without wall film	$T_{wall} > T_{pR}$

Within each regime, the interaction behavior is further distinguished according to the droplet Weber number, which relates to the ratio of deforming aerodynamic drag to the stabilizing surface tension. The droplet Weber number is defined as:

$$We_p = \frac{\rho_p u_p^2 d_p}{\sigma}\,, \tag{2.55}$$

where ρ_p, u_p and d_p denote the liquid fuel density, the droplet velocity and the droplet diameter, respectively. σ refers to the surface tension.

The **cold wetting regime (CW)** describes the droplet wall interaction for wall temperatures below the pure adhesion temperature T_{pA}. Within the regime, different forms of interaction are possible, depending on the particle Weber number. For Weber numbers smaller than a critical Weber number We_{crit} and the existence of a wall film, bouncing of the droplet occurs. In this case, the complete droplet with the same mass and kinetic energy is reflected by the wall film. If the Weber number is higher or no wall film exists, spreading or splashing can occur. The distinction between the two forms of interaction is controlled by a dimensionless parameter, which depends on the particle Weber number, Laplace number and other influencing parameters. In case of spreading, the impinging droplet is completely transferred into the wall film. For the solver ANSYS® CFX®, this means the particle type is changed from a regular particle to a wall particle. In contrast to spreading, splashing only transfers a part of the droplet into the wall film. The rest of the droplet is reflected by the wall and migrates back into the domain. Figure 2.3 illustrates the three scenarios that occur depending on the droplet Weber number.

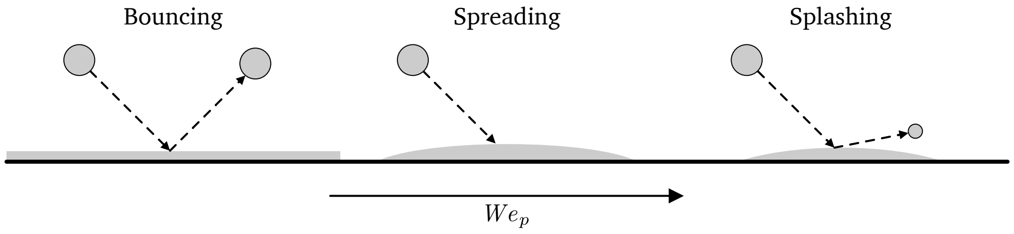

Figure 2.3.: Schematic spray-wall interaction for cold wall with wall film.

In between the two temperatures T_{pA} and T_{pR} the **hot wetting regime (HW)** applies. In this regime, in addition to the already known forms of interaction from the CW (bouncing, spreading and splashing in the presence of a wall film), boiling of the particle when it hits a non-wetted wall is also considered. Abrupt boiling of the droplet causes it to explode and a number of child droplets are ejected from the wall. For high droplet Weber numbers, this can occur combined with splashing and results in three reflected child particles. Schematically, the mechanisms are shown in Figure 2.4.

For wall temperatures higher than the pure rebound temperature T_{pR}, no wall film can exist and the **hot non-wetting regime (HNW)** is valid. In this regime, a distinction is made between rebound, rebound + breakup and breakup depending on the droplet Weber number. For low

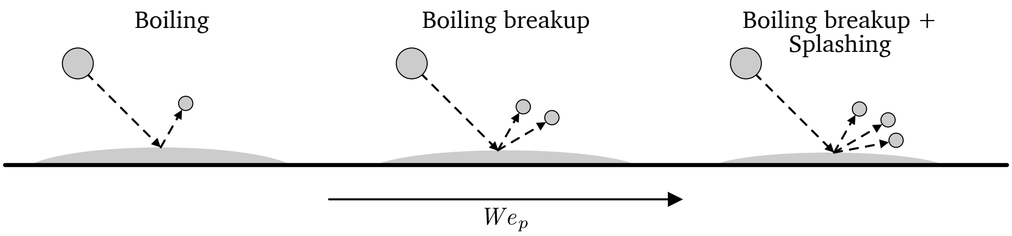

Figure 2.4.: Schematic spray-wall interaction for hot wall with wall film.

Weber numbers the droplet is completely reflected by the hot wall (rebound), while with increasing Weber numbers the droplet breaks up into a larger child droplet and several smaller child droplets (rebound + breakup), similar to the boiling mechanism. With further increasing Weber numbers, there finally is complete disintegration of the droplet into a large number of child droplets (breakup). These mechanisms are shown representatively in Figure 2.5.

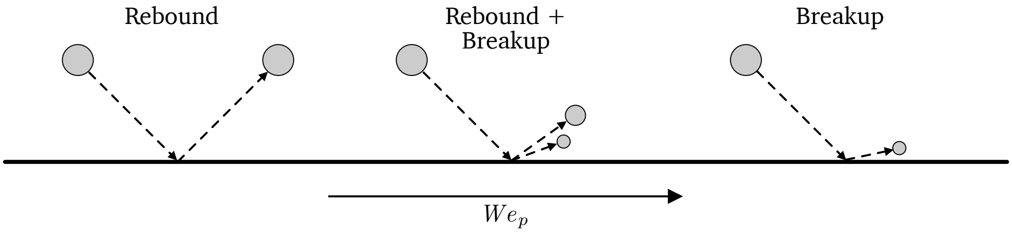

Figure 2.5.: Schematic spray-wall interaction for cold wall without wall film.

A detailed description of the Elsässer spray-wall interaction model and its implementation in ANSYS$^{®}$ CFX$^{®}$ can be found in Mühlbauer [27] and the corresponding software documentation of the flow solver [25].

Wall film modeling

Depending on local conditions (wall temperatures, Weber number, etc.), a thin wall film can form on the domain surface according to the modeling of the spray-wall interaction. To treat the heat and mass transfer of this wall film, the *quasi static wall film model* is used in ANSYS$^{®}$ CFX$^{®}$. The model neglects any movement of the film due to external forces and considers an interaction with the environment only by heat and mass transfer. A wall element is considered to be wetted as soon as a wall particle is created on the element surface.
The heat transfer of a single wall particle can be calculated using the following equation:

$$m_p c_p \frac{dT}{dt} = Q_{cond} + Q_{conv} + Q_{evap}\,. \tag{2.56}$$

In this equation, Q_{cond} is the conductive heat transfer between wall and wall film, Q_{conv} is the convective heat transfer between wall film and flow, and Q_{evap} is the heat transfer due to evaporation.

The conductive heat transfer is calculated accordingly:

$$Q_{cond} = hA_p \left(T_w - T_p\right) \tag{2.57}$$

with the wall particle temperature T_p and the wall temperature T_w. The wetted area A_p is calculated from the wall particle volume and the wall film thickness. The conductive heat transfer coefficient h is computed as $h = \lambda_p/\delta_f$ with the wall film thickness δ_f.

The convective heat transfer follows a similar calculation based on the gas temperature T_g:

$$Q_{conv} = hA_p \left(T_g - T_p\right) \ . \tag{2.58}$$

The heat transfer coefficient h is set according to the transfer coefficient calculated by the flow solver.

Heat loss due to evaporation is based on the enthalpy of evaporation:

$$Q_{evap} = \dot{m}_p \Delta h_v \ . \tag{2.59}$$

The evaporation rate depends on the temperature of the wall particle. If the wall particle is in the non-boiling regime, the rate is calculated according to the mass fractions:

$$\dot{m}_p = k \frac{Y_s - Y}{1 - Y_s} \tag{2.60}$$

with the transfer coefficient for scalars k from the flow solver, Y_s the mass fraction of the species at the film surface, and Y the mass fraction of the species calculated by the flow solver.

For boiling wall films, the mass flow is calculated based on the convective and conductive heat fluxes according to:

$$\dot{m}_p = \frac{-\left(Q_{cond} + Q_{conv}\right)}{\Delta h_v} \ . \tag{2.61}$$

The wall film thickness δ_f of each wall element can be calculated from the volume fraction of all wall particles in the wall element r_{pw}, the volume of the wall element Vol_{cv} and the wall surface of the wall element $A_{w,cv}$.

$$\delta_f = \frac{r_{pw}\, Vol_{cv}}{A_{w,cv}} \ . \tag{2.62}$$

2.2.4. Combustion Modeling

In general, combustion can be described as a chemical conversion of a fuel that undergoes a rapid oxidation reaction releasing energy in the form of heat and light. The process requires three essential ingredients [17]: (1) a fuel, (2) an oxidizer, and (3) a high temperature. When these three ingredients are present together in the same location, combustion can occur, resulting in the exothermic conversion of the reactants into combustion products. Depending on whether the two reactants, fuel and oxidizer, are completely mixed prior to combustion or whether they are present in two separate streams that only mix at the flame front, a distinction is made between *premixed* and *non-premixed* combustion.

Premixed combustion is characterized by a more intense but less pollutant flame in comparison to non-premixed combustion. However, because a flammable mixture is already present from the beginning, a single local high-temperature region can lead to spontaneous ignition and undesirable combustion, which is why this class of combustion is usually considered the more dangerous. However, a premixed flame can only burn within a specific flammability limit and will not propagate in very lean or very fuel-rich mixtures. On the other hand, non-premixed combustion is characterized by a low burning rate limited by the diffusion of the reactants into the flame front. The combustion occurs in the mixture's stoichiometric region, leading to higher maximum temperatures and potentially higher pollutant formation. Contrary to premixed combustion, flammability is not limited by the flow rate of the fuel or oxidizer stream since a flammable mixture is always reached in the mixing zone.

The relevant combustion process for this work takes place in the gasoline direct-injection (GDI) engine and can be classified as turbulent premixed combustion. The next section will therefore elaborate on the aspects of turbulent premixed combustion.

Stoichiometry

Chemical reactions are based on the principle of element conservation. The global reaction of the combustion of an arbitrary single-component hydrocarbon fuel with m carbon atoms and n hydrogen atoms can be written as:

$$\nu'_F \, \mathrm{C}_m\mathrm{H}_n + \nu'_{\mathrm{O}_2} \, \mathrm{O}_2 \longrightarrow \nu''_{\mathrm{CO}_2} \, \mathrm{CO}_2 + \nu''_{\mathrm{H}_2\mathrm{O}} \, \mathrm{H}_2\mathrm{O} \, , \tag{2.63}$$

where ν'_k describes the stoichiometric coefficient of the reactant species k and ν''_k of the product species k. The index $k = F$ indicates the values of the fuel species.

Stoichiometry is defined as the ratio at which both fuel and oxidizer are completely consumed in the reaction to yield the products CO_2 and $\mathrm{H}_2\mathrm{O}$ [28]. By assuming an stoichiometric coefficient for $\nu'_F = 1$ all other coefficients can be calculated according to:

$$\nu'_F = 1\,, \quad \nu'_{\mathrm{O}_2} = m + \frac{n}{4}\,, \nu''_{\mathrm{CO}_2} = m\,, \nu''_{\mathrm{H}_2\mathrm{O}} = \frac{n}{2}\,. \tag{2.64}$$

Since the ratio of moles must be equal to the ratio of stoichiometric coefficients of fuel and oxidizer, the ratio of unburnt (u) mass fractions for stoichiometric combustion can be calculated as:

$$\left.\frac{Y_{\mathrm{O}_2,u}}{Y_{F,u}}\right|_{st} = \frac{\nu'_{\mathrm{O}_2}}{\nu'_F}\frac{W_{\mathrm{O}_2}}{W_F} = \nu\,, \tag{2.65}$$

where W_k is the molar mass of species k and ν is called the stoichiometric mass ratio.
With the consumption of fuel and oxidizer during combustion, the mass fraction of both reduces according to the stoichiometric mass ratio. Hence, the relationship between the mass fractions at any given reaction progress and the mass fractions in the unburnt state can be written as follows:

$$\nu Y_F - Y_{\mathrm{O}_2} = \nu Y_{F,u} - Y_{\mathrm{O}_2,u}\,. \tag{2.66}$$

The concept of mixture fraction

The most common concept to describe the mixture of reactive flows is the introduction of the mixture fraction [28]. The mixture fraction can be defined for a system with two feed streams, a fuel stream (index 1) and an oxidizer stream (index 2), by the ratio of the fuel stream to the overall stream:

$$Z \equiv \frac{\dot{m}_1}{\dot{m}_1 + \dot{m}_2}\,. \tag{2.67}$$

Since both feed streams can carry inert gases, the fuel and oxidizer mass fraction of the overall mixture can be defined by the mass fraction of fuel and oxidizer in the respective feed streams:

$$Y_{F,u} = Y_{F,1}Z \quad \text{and} \quad Y_{\mathrm{O}_2,u} = Y_{\mathrm{O}_2,2}\left(1 - Z\right)\,, \tag{2.68}$$

where u indicates the mixture composition in the unburnt state and $Y_{F,1}$ and $Y_{\mathrm{O}_2,2}$ represent the mixture fraction of fuel and oxidizer in the respective stream. Combining both expressions with equation 2.66, a definition for the mixture fraction can be derived that combines both mass fractions of fuel and oxygen:

$$Z = \frac{\nu Y_F - Y_{\mathrm{O}_2} + Y_{\mathrm{O}_2,2}}{\nu Y_{F,1} + Y_{\mathrm{O}_2,2}}\,. \tag{2.69}$$

The mixture fraction required for stoichiometric combustion can be calculated based on the fuel and oxidizer stream composition of the system. Assuming that neither fuel nor oxidizer may remain after combustion under stoichiometric conditions, equation 2.69 can be simplified to calculate the stoichiometric mixture fraction Z_{st}:

$$Z_{st} = \frac{Y_{\mathrm{O_2},2}}{\nu Y_{F,1} + Y_{\mathrm{O_2},2}} \,. \tag{2.70}$$

In the internal combustion engine community, further formulations have become established to describe the mixture fraction. The air-fuel ratio is defined as the ratio of the air stream to the fuel stream:

$$AFR \equiv \frac{\dot{m}_{air}}{\dot{m}_{fuel}} \,. \tag{2.71}$$

Using the stoichiometric conditions as a reference, the more commonly used air-fuel equivalence ratio λ can be introduced:

$$\lambda = \frac{1}{\phi} = \frac{AFR}{AFR_{st}} \,, \tag{2.72}$$

with its reciprocal fuel-air equivalence ratio ϕ, usually referred to as 'equivalence ratio'. It is a commonly used post-processing variable in CFD and is used in this thesis for the interpretation of the local mixture. The equivalence ratio takes the value of 1 for stoichiometric mixtures, the value increases in fuel-rich mixtures, and the value decreases below 1 for lean mixtures. It is related to the mixture fraction Z by:

$$Z = \frac{Z_{st}\phi}{1 - Z_{st} + Z_{st}\phi} \quad \text{or} \quad \phi = \frac{Z}{1 - Z}\frac{(1 - Z_{st})}{Z_{st}} \,. \tag{2.73}$$

G-Equation Model

Modeling turbulent combustion requires not only a description of the flame front and the processes inside the flame but also a description of the flame-turbulence interaction. Over the years, a variety of models have been established for the description of turbulent flames.

A popular approach commonly used for practical applications is the geometrical description of the flame front by Williams [29] using a G-equation. In this approach, the flame front is treated as an interface between unburnt and burnt species and is spatially tracked by means of the isosurface of a scalar field G. It is based on the assumption of a thin flame and is thus closely related to the Flamelet assumption [30].

For laminar flows, the movement of the flame front $\mathbf{x}_f$ can be described by:

$$\frac{d\mathbf{x}_f}{dt} = \mathbf{u}|_{\mathbf{x}_f} + \mathbf{n}s_L \,. \tag{2.74}$$

In this equation, $\mathbf{u}|_{\mathbf{x}_f}$ indicates the flow velocity at the flame front and thus the convective transport of the flame, and s_L denotes the laminar burning velocity of the flame in the flame front normal direction $\mathbf{n}$.

To describe the movement in a continuous form, the scalar field G is introduced. The flame front is located at the isosurface of the scalar at $G(\mathbf{x}_f, t) = G_0$. To fulfill this condition, the transport equation for G can be stated as follows:

$$\frac{\partial G}{\partial t} + \frac{d\mathbf{x}_f}{dt} \cdot \nabla G = 0\,. \tag{2.75}$$

With this description, the flame front normal can be determined directly by the gradient of the scalar G:

$$\mathbf{n} = -\frac{\nabla G}{|\nabla G|}\,. \tag{2.76}$$

Combining both equation 2.75 and equation 2.74 yields the simplified G-equation for laminar flames:

$$\frac{\partial G}{\partial t} + \mathbf{u} \cdot \nabla G = s_L |\nabla G|\,. \tag{2.77}$$

It should be noted that this equation is valid only for the flame front.

A formulation of the equation for turbulent combustion in the context of RANS modeling using Favre-averaged quantities can be derived in a similar manner and is discussed extensively by Peters [31]. The transport equation for the Favre-averaged G-scalar $\widetilde{G}$ is given by:

$$\overline{\rho}\frac{\partial \widetilde{G}}{\partial t} + \overline{\rho}\widetilde{\mathbf{u}} \cdot \nabla\widetilde{G} = \left(\overline{\rho} s_T^0\right) |\nabla\widetilde{G}| - \overline{\rho} D_t' \widetilde{\kappa} |\nabla\widetilde{G}| \tag{2.78}$$

with the now unclosed turbulent unstretched flame velocity s_T^0 and the unclosed curvature term with turbulent diffusivity D_t'. The curvature κ can be determined directly from the definition of the G-scalar:

$$\kappa = \nabla \cdot \widetilde{\mathbf{n}}\,. \tag{2.79}$$

A transport equation can also be established for the variance of the G-scalar $\widetilde{G''^2}$:

$$\overline{\rho}\frac{\partial \widetilde{G''^2}}{\partial t} + \overline{\rho}\widetilde{\mathbf{u}} \cdot \nabla\widetilde{G''^2} = \nabla_{||} \cdot \left(\overline{\rho} D_t \nabla_{||}\widetilde{G''^2}\right) + 2\overline{\rho} D_t \left(\nabla\widetilde{G}\right)^2 - c_s \overline{\rho}\frac{\widetilde{\varepsilon}}{\widetilde{k}}\widetilde{G''^2}\,. \tag{2.80}$$

This formulation contains already modeled expressions on the right-hand side. for turbulent transport, turbulent production and destruction. The first term on the right-hand side describes the turbulent transport modeled by a mean gradient transport type of approach considering only the gradient tangential to the mean flame front $\nabla_{||}$. The second term on the right-hand side models turbulent production using the classical gradient flow hypothesis. In both approaches the turbulent diffusion D_t appears, which is related to the turbulent viscosity by:

$$D_t \equiv \frac{\mu_t}{\bar{\rho}\, Sc_t}\,. \tag{2.81}$$

The third term on the right-hand side, the flame brush thickness reducing term, includes the influence of kinematic restoration, which dominates in the corrugated flame regime, and scalar dissipation, which dominates in the thin reaction zone. It can be modeled according to Peters [32] by a unified approach depending on the turbulent time scales with an additional constant c_s.

The turbulent diffusivity in the curvature term of the G-Scalar equation is modeled in analogy to a mixing length approach using the turbulent flame-brush thickness as a length scale. The model constant is chosen to satisfy the balance of production and dissipation in the $\widetilde{G''^2}$ equation. Thus, for diffusivity, the result is:

$$D_t' = \sqrt{\frac{c_\mu c_s}{2\, Sc_t}} l_{f,t} k^{1/2}\,. \tag{2.82}$$

The variance of the G-scalar, $\widetilde{G''^2}$, can also be understood as a measure of the thickness of the turbulent flame brush. It is defined as:

$$l_{f,t} \equiv \frac{\sqrt{\widetilde{G''^2}}}{|\nabla \widetilde{G}|}\,. \tag{2.83}$$

Closure by means of turbulent flame speed

To close the system of equations, a model for the turbulent flame speed s_T is required. This can be modeled by means of the flame surface ratio σ_t based on the laminar flame speed according to:

$$s_T = s_L \left(1 + \sigma_t\right)\,. \tag{2.84}$$

Different approaches for modeling the flame surface ratio are available. Ewald [33] proposes an algebraic formulation based on the interaction of small and large-scale turbulent structures with the flame brush, which also includes unsteady effects of the flame brush development. He introduced the length ratio l^*:

$$l^* = \frac{l_{f,t}}{l_{f,t,alg}} \tag{2.85}$$

with $l_{f,t}$ as the current flame brush thickness and $l_{f,t,alg}$ as the algebraic formulation of the fully developed flame brush thickness. The latter can be calculated from the balance of production and destruction in the $\widetilde{G''^2}$ equation and the general definition of the flame brush thickness to:

$$l_{f,t,alg} = \frac{\sqrt{\widetilde{G''^2_{alg}}}}{|\nabla \widetilde{G}|} = \sqrt{\frac{2c_\mu}{c_s\, Sc_t}}\frac{k^{3/2}}{\varepsilon}\,. \tag{2.86}$$

The entire formulation for σ_t by Ewald can be read as follows:

$$\sigma_t = \frac{l_{f,t}}{l_f}\left(-\frac{{b_3}^2}{4b_1}\sqrt{\frac{3c_\mu c_s}{Sc_t}}l^{*q} + \sqrt{\frac{{b_3}^4}{16{b_1}^2}\frac{3c_\mu c_s}{Sc_t}l^{*2q} + \frac{c_s {b_3}^2}{2}\frac{l_f}{s_L}\frac{\varepsilon}{k}}\right) \tag{2.87}$$

with the model constants c_s, c_μ, q, b_1 and b_3, the turbulent Schmidt number Sc_t and the laminar flame speed s_L and laminar flame thickness l_f. Herein, the laminar flame thickness is calculated from the unburnt fluid properties under the assumption of a unity-Lewis number according to:

$$l_f = \left(\frac{\lambda/c_p}{\rho s_L}\right)_{unburnt}\,. \tag{2.88}$$

An overview of the model constants used is given in Table 2.3.

Table 2.3.: Model constants for the G-scalar/Ewald turbulent burning velocity model

Coefficient	**Value**
b_1	2.0
b_3	1.0
c_s	2.0
q	0.66
c_μ	0.09
Sc_t	0.7

Calculation of reaction species

To determine the local species composition inside the turbulent flame brush, the geometrical approach is coupled to 1D flamelets via a presumed probability density function (pdf) approach [31]. The Favre-averaged species composition can be calculated from the presumed pdf as:

$$\widetilde{Y}_k(\mathbf{x}) = \int_{-\infty}^{\infty} Y_k(x_n) P_{x_n}(\widetilde{G}(\mathbf{x}), \widetilde{G''^2}(\mathbf{x}))dx_n\,, \tag{2.89}$$

where $Y_k(x_n)$ is the species mass fraction along the one-dimensional flame coordinate x_n and P_{x_n} is the presumed pdf. A common assumption for the presumed pdf is a symmetric Gaussian distribution. This choice is justified by the availability of only two statistical moments of G and an expected symmetrical profile for very high ratios of u''/s_L [31].

However, if knowledge of the average species distribution of the flamelet is not required for the calculation and only the heat release is of interest, the representative species composition can be calculated using the composition of the unburnt and burnt species upstream and downstream of the flame front [33]:

$$\widetilde{Y}_i = (1-c)\,\widetilde{Y}_{i,u} + c\widetilde{Y}_{i,b}\,. \tag{2.90}$$

The indices u and b denote the compositions in the unburnt and burnt region of the flamelet, respectively, while the scalar c in the equation describes the reaction progress from unburnt $c = 0$ to burnt $c = 1$. It is calculated from the integral of the presumed pdf in equation 2.89, a Gaussian distribution, with the local values for $\widetilde{G}$ and $\widetilde{G''^2}$:

$$c = \int_{G^*=G_0}^{\infty} \frac{1}{\sqrt{2\pi\widetilde{G''^2}}} \exp\left\{ -\frac{\left(G^* - \widetilde{G}\right)^2}{2\widetilde{G''^2}} \right\} dG^*\,, \tag{2.91}$$

or in integral form:

$$c = \frac{1}{2} + \frac{1}{2}\operatorname{erf}\left(\frac{\widetilde{G} - G_0}{\sqrt{2\widetilde{G''^2}}}\right)\,. \tag{2.92}$$

To extend this definition from perfectly premixing mixtures to stratified mixtures, an additional transported variable must be introduced to account for local inhomogeneity, the mixing fraction Z. Similar to $\widetilde{G}$ and $\widetilde{G''^2}$, a Favre-averaged and variance value of Z is introduced. The transport equation for the averaged mixture fraction $\widetilde{Z}$ is derived by analogy with the conservation equations of the species as follows:

$$\frac{\partial \bar{\rho}\widetilde{Z}}{\partial t} + \bar{\rho}\nabla\widetilde{Z}\cdot\widetilde{\mathbf{u}} = \nabla\cdot\left(\mu + \frac{\mu_t}{Sc_t}\nabla\widetilde{Z}\right)\,. \tag{2.93}$$

It follows the subsequent transport equation for $\widetilde{Z''^2}$:

$$\frac{\partial \bar{\rho}\widetilde{Z''^2}}{\partial t} + \bar{\rho}\nabla\widetilde{Z''^2}\cdot\widetilde{\mathbf{u}} = \nabla\cdot\left(\mu + \frac{\mu_t}{Sc_t}\nabla\widetilde{Z''^2}\right) + 2\frac{\mu_t}{Sc_t}(\nabla\widetilde{Z})^2 - \bar{\rho}\chi_Z\,, \tag{2.94}$$

where the second term on the r.h.s of the equation describes the production and the third term the dissipation of $\widetilde{Z''^2}$. The scalar dissipation rate χ_Z in the dissipation term is modeled similarly to the respective term in the transport equation 2.80 for $\widetilde{Z''^2}$ dependent on the turbulent time scale:

$$\chi_Z = c_\chi\frac{\varepsilon}{k}\widetilde{Z''^2} \quad \text{with} \quad c_\chi = 2\,. \tag{2.95}$$

The uncertainty of the species composition due to its mixture fraction dependency is accounted for by again applying a presumed pdf approach to the equation. Assuming a beta pdf distribution of Z, the Favre-averaged species composition can be calculated via integration according to:

$$\widetilde{Y}_{i,b}(\widetilde{Z}, \widetilde{Z''^2}, T_{unb}, p) = \int_0^1 Y_{i,b}(Z, T_{unb}, p)\widetilde{P}(Z)dZ\,. \tag{2.96}$$

For practical applications, the species composition is usually tabulated in a pre-integrated manner in dependency of the transported quantities for $\widetilde{Z}$ and $\widetilde{Z''^2}$. This is also the case in this thesis.

Detailed documentation of the variant of the G-equation model implemented in ANSYS® CFX®, as well as details on the reinitialization of the G-scalar field, can be found in Toninel et al. [34].

Extension to include exhaust gas recirculation

The simulation of multiple engine cycles requires the consideration of the contribution of recirculated exhaust gas (EGR) from the previous cycle to the combustion process. In the context of this thesis, this was included by using the residual material model in ANSYS® CFX® [25].

The model extends the description of the mixture by means of the mixture fraction Z by introducing additional tracers for the mass fraction of fuel, oxidizer and EGR. The sum of all tracers Tr must equal the total composition and thus add up to one:

$$\widetilde{Tr}_F + \widetilde{Tr}_{Ox} + \widetilde{Tr}_{EGR} = 1\,. \tag{2.97}$$

Hereby, the index F denotes the fuel, Ox the oxidizer and EGR the residual gas fractions, respectively. Considering a stoichiometric composition of the residual gas $\widetilde{Z}|_{EGR} = Z_{st}$, the following relationship is obtained:

$$\widetilde{Z} = \widetilde{Tr}_F + \widetilde{Tr}_{EGR} \cdot Z_{st}\,. \tag{2.98}$$

The mixture fraction is composed of the “fresh” fuel mass represented by the fuel tracer $\widetilde{Tr}_F$ and the already consumed fuel mass $\widetilde{Tr}_{EGR} \cdot Z_{st}$ from the previous engine cycle that is present in the residual gas. To fully describe this system and determine between fresh and residual mixture, one additional mass fraction has to be transported next to the mixture fraction. In this work, the additional scalar transport equation for the Favre-averaged fuel tracer is solved:

$$\frac{\partial(\overline{\rho}\widetilde{Tr}_F)}{\partial t} + \frac{\partial\overline{\rho}\widetilde{u}_j\widetilde{Tr}_F}{\partial x_j} = \frac{\partial}{\partial x_j}\left[\left(\mu + \frac{\mu_t}{\sigma_Z}\right)\frac{\partial\widetilde{Tr}_F}{\partial x_j}\right]\,, \tag{2.99}$$

which has identical form as the transport equation of the Favre-averaged mixture fraction in equation 2.93. The residual gas fuel tracer can then be calculated from $\widetilde{Z}$ and $\widetilde{Tr}_F$ according to equation 2.98. The distinction between fresh and residual mixture allows a reformulation of equation 2.90. First, the composition of the fresh mixture considering fresh unburnt species and residual gas is determined:

$$\widetilde{Y}_{i,fresh} = (1-\widetilde{Tr}_{EGR})\widetilde{Y}_{i,u}(\widetilde{Z}|_{fresh}) + \widetilde{Tr}_{EGR}\widetilde{Y}_{i,b}(\widetilde{Z}_{st}, \widetilde{Z''^2}=0)\,, \tag{2.100}$$

where the fresh unburnt species are calculated as a function of the conditional fresh mixture:

$$\widetilde{Z}\Big|_{fresh} = \frac{\widetilde{Tr}_F}{\widetilde{Tr}_F+\widetilde{Tr}_{Ox}} = \frac{\widetilde{Tr}_F}{1-\widetilde{Tr}_{EGR}}\,. \tag{2.101}$$

Next, the fresh composition can be used to determine the current mixture composition dependent on the reaction progress c:

$$\widetilde{Y}_i = (1-c)\widetilde{Y}_{i,fresh} + c\widetilde{Y}_{i,b}(\widetilde{Z}, \widetilde{Z''^2}, T_{unb}, p)\,. \tag{2.102}$$

2.3. Soot Particulate Emissions

Several types of emissions are relevant in the context of internal combustion engines. Since this work is focused mainly on the formation of particulate emissions, the following section will give an overview of the soot particulate formation chain and applied methods for modeling these emissions. For a more detailed description of the modeling method, the author refers to the work of Salenbauch [35].

2.3.1. Formation, Growth and Oxidation of Soot Particulates

In the engine context, the term particulate emissions usually refers to the occurrence of small carbonaceous particles during incomplete combustion. These soot particles do not have a clearly defined molecular structure but can differ significantly in their carbon-to-hydrogen ratio. According to Tree et al. [36], depending on their age, they have a carbon-to-hydrogen ratio of 1 for very young particles up to a ratio of 8 to 1 for mature particles. There is widespread agreement in literature about the chain of formation of soot particles. Six major processes contribute to soot formation, growth, and reduction: pyrolysis, nucleation, coalescence, surface growth, aggregation, and oxidation [36].

The formation of soot particles begins in the gas phase through fuel pyrolysis under low-oxygen conditions at correspondingly high temperatures. Dimerization of large polycyclic aromatic hydrocarbons (PAHs) leads to nucleation of the first particles and transition to the liquid/solid phase. Collisions, especially of young particles, lead to coalescence and thus result in particle growth with decreasing particle number density. Further physically and chemically induced surface growth is responsible for a further increase in particle size. Mature particles can further aggregate into large coherent structures. Such structures can deviate greatly from the semi-spherical shape of individual primary particles. As a counter effect to surface growth, oxidation can reduce particle volume, lead to fragmentation of large aggregates or even to complete oxidation of particles. Figure 2.6 provides an overview of the soot formation chain. The individual processes and phenomena are explained in more detail below.

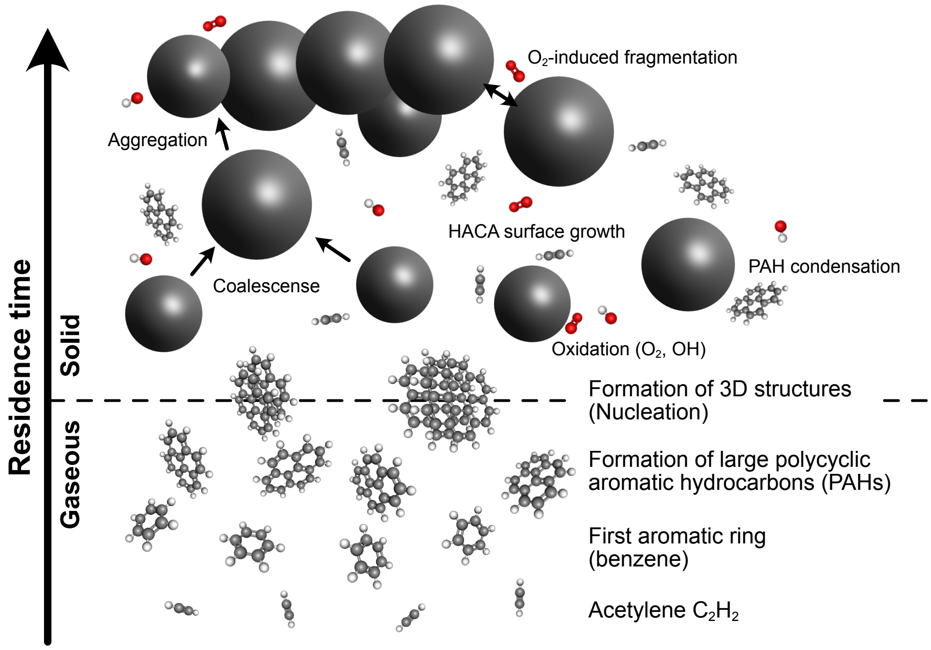

Figure 2.6.: Schematic representation of the soot particle formation chain, including gaseous soot precursor formation, nucleation, coalescence, aggregation, surface growth and oxidation processes. Taken from [35] and adapted.

Fuel pyrolysis and gaseous formation of soot precursors

Fuel pyrolysis under fuel-rich conditions to smaller hydrocarbon molecules, preferably C_2H_2, is considered crucial for soot formation. These molecules form larger polycyclic aromatic hydrocarbons (PAHs), which are known to be direct soot precursors [37]. State-of-the-art models assume the reactions involving C_3 and C_4 molecules are responsible for the formation of the first aromatic benzene ring (A1-C_6H_6) [38, 39]. Subsequently, the formation of larger PAHs follows a chemical growth mechanism commonly referred to as the "H-abstraction-C_2H_2-addition" (HACA) mechanism [40] or by a direct combination of multiple benzene rings [41]. McEnally [42] also assumes that aromatic compounds already present in the fuel are not initially decomposed but contribute directly to forming larger PAHs.

Nucleation of first soot particles

Based on those soot precursors, a series of mechanisms leads to the formation of larger three-dimensional carbonaceous structures. This point is referred to as the nucleation of the first soot particles. The exact processes leading to the nucleation of the first soot particles, especially due to a number of experimental difficulties [43], still need to be fully understood and are the subject of current research. However, two pathways are critical to the nucleation process. One is the stacking of multiple PAH molecules, and the other is the ongoing growth of PAHs towards larger gaseous structures. Stacking occurs by the dimerization of two PAH molecules after a collision. Due to repeated collision with PAHs, the resulting dimers gradually develop into larger structures [44]. However, Yoshihara [45] has shown that this stacking of PAH clusters alone is not sufficient to explain the observed growth of soot particles. Further growth of PAH radicals, for example, through the addition of acetylene to pericondensed aromatic hydrocarbons (PCAHs) or the addition of other aromatic and aliphatic components to condensed aromatic aliphatic linked hydrocarbons (AALHs), can also contribute to the nucleation of initial soot particles [46].

Coagulation, surface growth and oxidation of soot particles

Once a particle has formed, it can interact in various ways with the surrounding gas phase or other particles. The main processes can be divided into coagulation, surface growth and oxidation. Coagulation processes refer to the coalescence or aggregation of two or more particles with each other. While coalescence occurs mainly in young particles and is understood as a complete merging of two particles to form a new particle [47], the formation of aggregates, coherent structures consisting of several shape-holding primary particles, often occurs in mature particles [48]. There are several theories to explain the coalescence and aggregation of soot particles. One assumes that young soot particles have a liquid-like structure and, for this reason, coalesce entirely upon collision. Due to the minimization of free energy, these newly formed particles tend to return to a spherical shape [36]. Mature particles, on the other hand, exhibit surface aging and feature a rigid structure, and therefore tend to form aggregates [44].

Surface growth can occur by condensation and chemical surface reactions. While condensation describes the deposition of PAHs or PAH radicals on the particle surface [36], chemical surface growth is again dominated by the HACA mechanism [44]. Both are essential processes that contribute significantly to the increase in mass and volume of soot particles [44].

A process counteracting surface growth is soot particle oxidation. Oxidation occurs by reaction with O_2 and OH in the gas phase. In fuel-rich and stoichiometric regions, oxidation with OH [36] dominates due to its high reactivity and a uniform reduction of soot occurs [49]. In lean regions, on the other hand, oxidation with O_2 gains importance. In contrast to OH, oxidation with O_2 leads to increased fragmentation of the soot particles and aggregates [49, 50]. This is due either to the penetration of slow-reacting O_2 into the particles or to a targeted attack on the bonds of individual primary particles [46].

2.3.2. Modeling of Soot Particulate Emissions

As outlined in the previous section, the formation and evolution of soot particles is subject to a complex interplay of various physical and chemical effects. Depending on local conditions, this can lead to huge particle number densities with very different specific particle properties (e.g. different particle sizes). For a predictive numerical simulation of soot emissions in the context of internal combustion engines, it is therefore necessary to describe these processes in detail, both in the underlying gas phase and at the level of the soot particle distribution. In the following, the detailed gas phase mechanism and the modeling of the soot particle distribution used in this work will be further discussed.

Detailed gas phase mechanism

A detailed mechanism is required to characterize all soot-relevant reactions at the gas phase level prior to the nucleation process, as well as relevant precursors for growth and oxidation.

For this purpose, a detailed mechanism with 170 species and 5500 elementary reactions describing the high-temperature chemistry derived from a larger kinetic scheme developed at Politecnico di Milano is used. The specific mechanism utilized in this work was published by Salenbauch et al. [51] and described in detail in [35].

The kinetic scheme considers decomposition and oxidation reactions of various fuels such as isooctane (C_8H_{18}) but also includes several key components to comprehensively model the formation and evolution of soot-related species, such as the formation of first aromatic rings via C_1-C_4 chemistry. The growth of large PAHs is modeled using the HACA mechanism. The main consumption mechanisms of aromatics and PAHs, such as H-abstraction reactions by H and OH radicals, are also included. Since all these capabilities of the model have a particular emphasis on the prediction of soot, the mechanism has been intensively validated in this regard in a series of studies [38, 52–54].

For the coupling of the gas phase model with the deployed soot model, the mechanism was further adapted and A4-$C_{16}H_{10}$ was set as the heaviest component to address the fact that it is the only species that is directly connected to the solid phase through nucleation and condensation [35].

Modeling of the soot particle distribution

Modeling an ensemble of soot particles is a complex task, as individual particulate properties, e.g., size, shape and hydrogen-to-carbon ratio, differ depending on the flame conditions and the position within the flame substantially [55]. To properly describe the particle properties, several methods are available. The most common methods are *Monte Carlo methods*, *sectional methods* and *method of moments*.

Monte Carlo methods are used to describe particle processes by approximating the soot particle population balance from the transport of a sufficiently large number of stochastic particles. Those methods are known to yield very accurate results. However, due to their computational expense, their applicability has been limited to very simple configurations. Nevertheless, these methods are suitable for generating highly accurate reference data for validating other methods [51, 56, 57].

Sectional methods, on the other hand, describe the spectrum of particle properties, e.g., the particle volume, by separating them into a distinct number of classes. For each class, a separate transport equation is solved. These methods are easy to implement but very computationally expensive if the number of sections is large. These methods have already been successfully used in the past for the simulation of particulate emissions in gasoline combustion engines [58–60].

A third approach for detailed and efficient modeling of the soot particle population balance is the *method of moments*. This approach has the advantage that only a small set of statistical moments have to be transported in the CFD simulations compared to a vast number of stochastic particles or a large set of classes, leading to a higher computational efficiency while still retaining statistical accuracy [61]. However, the difficulty lies in the closure of the moment source terms since these terms depend on the particle property distribution, which is unknown. Over the past decades, various closure methods have been developed, resulting in a variety of approaches [56, 62–65]. A large number of those approaches have already found their way into practical application. Closure approaches such as the method of moments with interpolative closure (MOMIC) have been used for diesel engine combustion since the 2000s [66–68]. These methods have also been applied to the simulation of aero-engine combustors [69]. More recent developments for diesel engine combustion rely on moment projection methods (MPM) that can robustly handle the shrinkage of particles while retaining numerical simplicity [70–72]. Another popular closure approach is the quadrature method of moments (QMOM). The method was introduced in 1997 by McGraw [73] initially for aerosol dynamics. In his approach, a series of delta functions and corresponding weights are used to represent the unknown particle property distribution. The goal is to accurately reproduce the statistics of the distribution in order to calculate the source terms of the moment equations.

In the current state, several variants and extensions of this method exist. More improved methods making use of kernel density functions for approximation of the particle property distribution and hybrid methods combining the capabilities of MOMIC and QMOM have been extensively tested and validated in generic laminar and turbulent flame configurations [74–76]. A deployment of those methods on initial technical applications was also conducted [77, 78]. However, none of the moment approaches mentioned so far have been applied to study soot formation in gasoline engines.

In the context of this work, a QMOM-based soot model is employed. The implementation of the model was done by Salenbauch [35] and is described in detail in his thesis (Model I). The following provides an overview of the fundamentals of the model.

We consider a distribution function that maps the particle number density over certain particle properties $\boldsymbol{\xi}$. This function is referred to as the number density function (NDF) $n(\mathbf{x}, t; \boldsymbol{\xi})$ and depends on the spatial coordinate $\mathbf{x}$, the time t and the property vector $\boldsymbol{\xi}$. In this work, a univariate NDF is considered with the particle volume as an independent property parameter $\boldsymbol{\xi} = V$. The evolution of the soot NDF in the combustion chamber is governed by the population balance equation (PBE), which is defined as (overbars indicate Reynolds-averaging)

$$\frac{\partial \overline{n}(\mathbf{x}, t; V)}{\partial t} + \frac{\partial \overline{u}_i \overline{n}(\mathbf{x}, t; V)}{\partial x_i} = \frac{\partial}{\partial x_i}\left(D_t \frac{\partial \overline{n}(\mathbf{x}, t; V)}{\partial x_i}\right) + \overline{\dot{n}}(\mathbf{x}, t; V) \tag{2.103}$$

with the particle velocity u_i and the turbulent diffusivity D_t. The source terms $\dot{n}(\mathbf{x}, t; V)$ on the right-hand side account for the local physico-chemical processes explained above. As equation 2.103 is high-dimensional (depending not only on space and time but also on the particle volume V), its direct solution is not feasible in 3D-CFD simulations. Therefore, we consider statistical moments of the volume-based NDF rather than tracking the NDF itself directly. Moments are defined by

$$m_k = \int_0^\infty V^k n(\mathbf{x}, t; V) dV, \tag{2.104}$$

and applying equation 2.104 to equation 2.103 yields transport equations for moments of order k:

$$\frac{\partial \overline{m}_k(\mathbf{x}, t)}{\partial t} + \frac{\partial \overline{u}_i \overline{m}_k(\mathbf{x}, t)}{\partial x_i} = \frac{\partial}{\partial x_i}\left(D_t \frac{\partial \overline{m}_k(\mathbf{x}, t)}{\partial x_i}\right) + \overline{\dot{m}}_k(\mathbf{x}, t). \tag{2.105}$$

The main advantage of solving equation 2.105 (for different moment orders k) in the 3D-CFD engine simulations rather than equation 2.103 is that moments are scalar values that only depend on space and time (i.e., no dependency on the particle volume). Several studies have shown that even a small number of moments is sufficient to describe a distribution function with adequate accuracy [51, 56]. However, as a drawback, the transformation of the PBE to moment equations yields unclosed source terms since knowledge of the detailed shape of the NDF is lost. To achieve closure, we apply the quadrature method of moments (QMOM) [79], where the unknown NDF is approximated by a weighted sum of N_D Dirac delta functions $\delta(V - V_i)$:

$$n(V) \approx n^*(V) = \sum_{i=1}^{N_D} \delta\left(V - V_i\right) w_i. \tag{2.106}$$

The position of the delta functions V_i and the weights w_i are determined in such a way that the moments of $n^*(V)$ match the moments of the original (but unknown) soot NDF $n(V)$

$$m_k(n) = m_k\left(n^*\right), \tag{2.107}$$

and hence, the approximated NDF $n^*(V)$ can be applied for moment source term closure. The approximation $n^*(V)$ is obtained by applying the mathematical concept of quadrature theory. In particular, the unknown NDF is used as the weight function and the position of the Dirac delta functions correspond to quadrature nodes. The so-called moment inversion step, which determines the values of the quadrature node positions and weights from the transported moment set, further uses the concept of orthogonal polynomials and their relation to the statistical moments through the definition of recursion coefficients. Further details on the underlying mathematical theory can be found in Marchisio et al. [79] and Gautschi [80].

The physico-chemical phenomena considered in the source term calculation are particle nucleation, the condensation of polycyclic aromatic hydrocarbons (PAHs), chemical surface growth following the "H-abstraction-C_2H_2-addition" (HACA) mechanism [44], coagulation, and oxidation. Nucleation is described by the dimerization of pyrene molecules [81]. Condensation-based surface growth through large PAHs is assumed to take place via the collision of pyrene molecules and single soot particles following Balthasar et al. [81], while the rates for chemical surface growth follow the mechanism described in Appel et al. [82]. Oxidation occurs via reactions with O_2 and OH [41] and the rate parameters are also taken from Appel et al. [82]. Aggregation processes of single particles to large coherent structures are not included since the particle volume is considered as the only property parameter of the NDF. A detailed description of the calculation of the moment source term including all considered processes can be found in Salenbauch [35].

In summary, the soot model applied in this work is based on the solution of transport equations for two moments of a univariate soot particle distribution, which are closed using the QMOM approach. The source terms of the moment equations describe the physico-chemical processes of nucleation, condensation, HACA surface growth, coagulation, and oxidation. As these processes strongly depend on the underlying gas phase profiles (O_2, OH, C_2H_2, A4-$C_{16}H_{10}$, etc.) and gas phase temperature, the moment equations need to be coupled directly to the combustion model applied in the simulations. This coupling procedure with the 3D-CFD flow solver is discussed in Chapter 4.1.4.

3. Research Engines

Two different engines are used in the context of the investigations carried out in this thesis. While the numerical framework is first evaluated using a steady-state operating point of an optically accessible research engine, the framework is subsequently extended for the simulation of transient scenarios and applied to a full-metal series engine. In the following, the two investigated engines, including the available measurement techniques in each case, are further explained.

3.1. Optically Accessible Single-Cylinder Research Engine

To evaluate the numerical framework and the coupled moment-based soot modeling approach used in this work, a steady-state reference operating point from an optically accessible research engine is used. The research engine operated and experimentally investigated by LTT Erlangen[1] has already been the subject of a large number of publications [83–88] and has been extensively measured. For this reason, it is ideally suited for numerical comparison. The following is an overview of the research engine, its experimental setup, and the dataset available to evaluate the numerical setup.

3.1.1. Test Bench Description and Remarks

The investigated research engine is a modern/state-of-the-art optically accessible single-cylinder engine with four valves and direct injection. It is based on a modified production engine developed by BMW/PSA. For the injection, a laterally mounted solenoid injector (Bosch HDEV 5.1) is used. Additionally, the engine is equipped with a transparent cylinder liner and piston window to enable optical diagnostics.

Several experimental studies have been conducted on this engine [83–88]. Koegl et al. [88] investigated the impact of different biofuel admixtures and EGR rates on the soot formation and compared those at two operating points. They point out that the soot formation at early injection is in fact caused by liquid film evaporation and pyrolysis rather than by strong inhomogeneities

---

[1] Lehrstuhl für Technische Thermodynamik (LTT) Friedrich-Alexander-Universität Erlangen-Nürnberg (FAU)

in the gas phase. Since the numerical model used in this study aims in particular at the typical mixture-related soot formation processes, we will focus on the operating point at late injection. This experimental reference operating point is characterized by part-load operation at 1500 rpm with late injection (SOI = 140 °CA bTDC). The measurements were carried out using a surrogate fuel to ensure controlled and reproducible conditions. The primary objective in selecting this fuel was to achieve a similar soot emission behavior to conventional gasoline, in which the proportion of aromatic components plays a decisive role [89]. To meet this requirement, a two-component surrogate fuel was chosen consisting of 65 vol.% isooctane and 35 vol.% toluene as an aromatic component. Storch et al. [90] conducted a comparative study of the surrogate fuel with conventional gasoline and demonstrated similar soot emission potentials of both fuels for engine-related applications. Furthermore, the engine is operated with a global fuel-rich mixture (equivalence ratio $\phi = 1.25$) to promote soot formation and ensure the formation of distinct particles. The cylinder head, liner and lubricant oil were preconditioned at 333 K. An overview of the engine parameters used is shown in Table 3.1. For a complete description of the experimental setup, see Koegl et al. [87, 88].

Table 3.1.: Engine parameters and operating conditions.

Single-Cylinder Research Engine	
Engine Parameters	
Engine displacement volume	399 ccm
Stroke/Bore	85/77 mm
Effective compression ratio	9.5
Operating Point	
Engine Speed	1500 rpm
imep	0.215 MPa (part-load)
Fuel	TolIso (65 vol.% isooctane / 35 vol.% toluene)
Start of injection	140 °CA bTDC
Equivalence ratio	1.25
Ignition angle	28 °CA bTDC

3.1.2. Available Measurement Techniques

For the evaluation of the QMOM-based soot model coupled and applied in this work, data from various optical measurement techniques are available. High-speed soot extinction measurements allow the quantitative assessment of the soot volume fraction within a field of view (FOV) of 57.5×33.5 mm directly beneath the cylinder head. In total, ensemble-averaged data from 48 engine cycles are available for comparison with the line-of-sight (LOS) averaged soot volume fraction from the 3D-CFD simulation.

In addition, measurements are available for soot luminescence in the cylinder head region. These measurements are not suitable for quantitative comparison due to their temperature dependency. However, they can provide further insights about the soot formation outside the FOV of the previously described extinction measurement, especially during the early combustion stage at high temperatures.

Besides measuring soot-related quantities, the setup can also be used to measure the extinction of liquid fuel spray during the injection process. The ensemble-averaged images of spray extinction from 16 engine cycles were utilized to calibrate the spray model used in the numerical engine model. A detailed description of the measurement setup can be taken from Koegl et al. [87].

3.2. Full Metal Series Production Engine

The extension and application of the numerical framework for transient engine operation is based on a measured transient operating scenario of a realistic full metal series engine. Corresponding measurements on the highly dynamic engine test bench were carried out by the Institute for Combustion Engines (VKM) at TU Darmstadt. The following section gives an overview of the engine used, the experimental setup and the measurement data available for determining boundary conditions and evaluating the numerical model.

3.2.1. Test Bench Description and Remarks

The subject of the investigation is a 2-liter inline turbocharged four-cylinder engine with gasoline direct injection from BMW (B48A20M1 ZIK). The engine has a cylinder head integrated exhaust manifold as well as variable valve lift (Valvetronic) and variable valve timing (Double VANOS).

An overview of the engine parameters is given in table 3.2. The engine is operated on the highly dynamic engine test bench of the VKM at TU Darmstadt. It allows the replication of real RDE relevant driving scenarios recorded on the road under controlled ambient conditions and the use of additional measurement technology. In this way, transient emission peaks can be analyzed in detail and associated boundary conditions can be identified and transferred to the 3D-CFD simulation setup. Full access to the engine control unit (ECU) allows the recording and adaption of relevant control parameters required for the transfer to the virtual engine model.

3.2.2. Available Measurement Techniques

To measure the engine pressure boundary conditions relevant for the 3D-CFD simulation, cylinder 4 of the production engine is equipped with high- and low-pressure indications. The

Table 3.2.: Characteristics of the investigated full metal series engine

Four-Cylinder Series Production Engine (BMW B48 A20M1 ZIK)	
Engine Parameters	
Cylinder Engine Type	4-cylinder in-line engine
Capacity / Compression	1998 cm^3 / 11.0:1
Power	141 kW / 192 PS @ 5000 rpm
max. torque	300 Nm @ 1350 rpm
Charging	Turbocharger
Combustion process	Gasoline direct injection
Nb. of Valves / Control	4 / Full Variable Valve Train (Valvetronic)

low-pressure indication is conducted on the intake-side in the intake manifold directly in front of the cylinder. For exhaust-side indication, a predesigned measuring point integrated into the cylinder head is used on the exhaust manifold. The high-pressure indication is also performed through a separate access point in the cylinder head.

An AVL APC 489 particle counter is used to capture the particle emissions. The particle counter detects particles down to a particle size of 23 nm at a rate of 1 Hz. The sampling point for all experiments considered in this work is located upstream of the catalytic converter and thus covers the raw emissions from the engine.

In order to gain information about the processes inside the engine, additional optical measurements are carried out in cylinder 4 of the engine in addition to the aforementioned high-pressure indication. A Visiolution sensor from AVL List GmbH with 8 optical light conductors is used to measure the light intensity. The sensor allows the detection of direction-dependent light intensity with a temporal resolution of up to 0.1 °CA.

In summary, the setpoint and actual parameters of the engine control unit (ECU) and the recorded particle count upstream of the catalytic converter are available for evaluation. Furthermore, pressure data at the inlet, outlet and inside the cylinder can be used to generate boundary conditions for cylinder 4 of the engine under investigation. Optical data from the Visiolution sensor are used to evaluate the processes inside the cylinder.

4. CFD Engine Model for the Analysis of Particle Emissions

This chapter introduces the 3D-CFD simulation framework for the simulation of soot particulate emissions in gasoline direct-injection engines used in this thesis. The framework is then applied to a sooting operating point of the optically accessible single-cylinder research engine introduced in Chapter 3.1 and evaluated using available optical measurements.

Parts of this chapter have been published in a peer-reviewed journal publication in *Fuel Processing Technology*:

[1] **F. Held**, J. Reusch, S. Salenbauch, and C. Hasse. “A 3D Computational Study of the Formation, Growth and Oxidation of Soot Particles in an Optically Accessible Direct-Injection Spark-Ignition Engine Using Quadrature-Based Methods of Moments”. In: *Fuel Processing Technology* 254 (Feb. 2024), p. 107923. DOI: `10.1016/j.fuproc.2023.107923`

4.1. CFD Framework for Engine Simulations

The in-cylinder 3D-CFD simulation of flow, mixing, combustion, and soot pollutant formation within an engine cycle requires a comprehensive framework. The investigations performed in this work are therefore carried out using the ANSYS® CFX® (2021.2/2022.2) flow solver. The basis of the used framework for engine simulations is the ANSYS® CFX® ICE process [91]. It offers extensions of the general flow solver for handling moving boundaries and automated geometry meshing.

The simulation of a single cylinder is performed in four geometric configurations. Each configuration from C1 to C4 is passed sequentially and is defined respectively by the opening of the inlet and exhaust valves of the cylinder. Depending on the position of the valves, individual geometric areas, such as the intake port, are connected to the cylinder geometry or cut off. All four configuration geometries are depicted as examples in Figure 4.1 and are explained in more detail below.

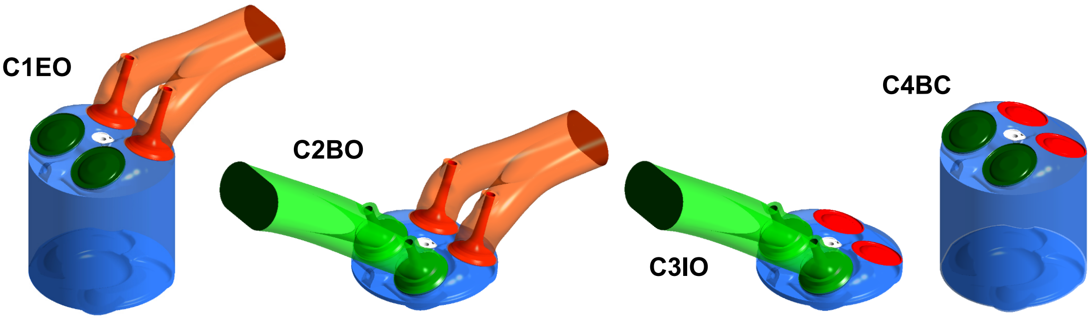

Figure 4.1.: The four base configurations of the 3D-CFD geometry.

The engine cycle begins with the exhaust phase, i.e., with the opening of the exhaust valves after the combustion has been completed. The following configurations are performed in sequence:

- Configuration 1, Exhaust Open (C1EO): Only the exhaust valves are open. The intake port is removed from the geometry and is not simulated. The burnt fuel-air mixture is pushed out of the combustion chamber into the exhaust manifold.

- Configuration 2, Both Open (C2BO): The intake valves start to open. Both intake and exhaust ports are connected to the geometry.

- Configuration 3, Intake Open (C3IO): The exhaust valves have closed and the exhaust port is separated from the geometry. Only the intake valves remain open. Fresh air is drawn into the combustion chamber from the intake port.

- Configuration 4, Both Closed (C4BC): Both intake and exhaust valves are closed. Both intake and exhaust ports are separated from the geometry. In this configuration, compression, combustion and expansion take place.

Buhl et al. [92] performed an extensive analysis of different port modeling strategies for scale-resolving simulations of cycle-to-cycle variations (CCV). The results indicate that neglecting flows for intake and exhaust ports separated from the cylinder geometry is justified.
It should also be noted that a fixed spark plug alignment is chosen for all numerical simulations to ensure that this study is geometrically consistent with previous studies. This is justified because different alignments in the experimental setup have not shown any significant effects on engine behavior in previous measurement campaigns.

4.1.1. Mesh Strategy

For the spatial resolution of the engine geometry, the Advanced Dynamic Remeshing [91] approach incorporated in the ANSYS® CFX® ICE process is used.

The starting point for the approach are initial meshes at the start time of each geometry configuration. Based on these, the geometry motion and resulting mesh deformation along the engine cycle is simulated in a separate mesh calculation. If the mesh quality declines too much due to the deformation, the simulation pauses and a remeshing of the geometry is initiated. The critical parameter for the mesh quality is the minimum orthogonality angle. This work uses a minimal orthogonality angle at 6 degrees as the required quality threshold.

The remeshing is automated according to predefined criteria. A large part of the geometry, including the intake and exhaust, the area below the cylinder head and the region directly above the piston, is discretized with tetrahedral cells. If the piston position allows it, the intermediate part between the cylinder head and piston is filled with an extrusion mesh. In this work, the global mesh size is chosen as 1 mm. Local refinements are made in the region of the valve gap and the cylinder head and vary between 0.125 mm and 0.25 mm depending on the crank angle. Prism cells with five layers are used near the walls.

All meshes created during recurrent remeshing events, referred to as key grids, are stored in a database for reuse in subsequent simulations. The condition to be able to reuse the generated meshes in subsequent simulations is the identical movement of the geometry, i.e., identical compression ratio, valve timing and stroke. The total number of key grids for the entire cycle for the operating point of the optically accessible engine investigated in this work is 69. The number of mesh nodes varies along the cycle between 0.78 million and 1.35 million nodes. Figure 4.2

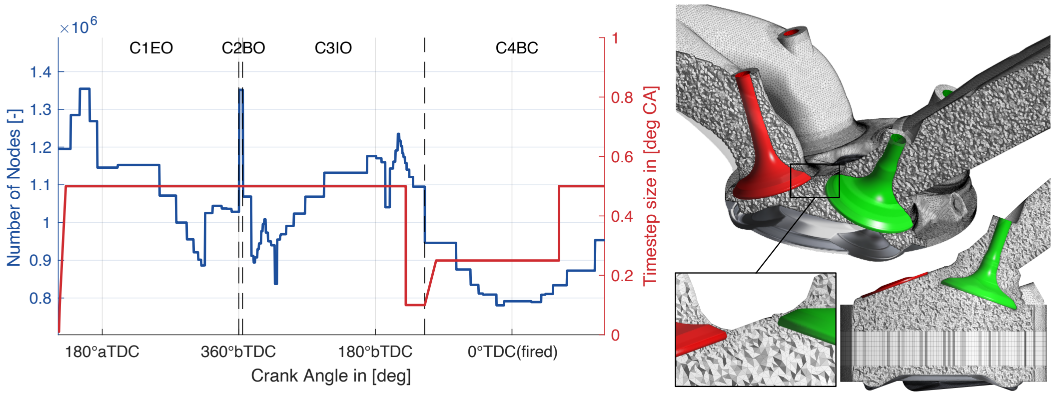

Figure 4.2.: Left: Mesh size and temporal resolution for different crank angles along the engine cycle. Right: Representative spatial resolution of the domain at two different crank angles. For visualization purposes, the mesh is mirrored at the symmetry plane. Top/bottom left: Mesh at 365 °CA.

(left) depicts the respective mesh size in blue over the engine cycle. In Figure 4.2 (right), the mesh is shown exemplarily for two piston positions. Highlighted are the resolution of the valve gap and the use of the extrusion mesh when the piston position is shifted sufficiently.
For the temporal resolution of the engine simulation, a time step size of 0.5 °CA corresponding to $5.5 \cdot 10^{-5}$ s is specified over a large part of the cycle. In areas requiring additional modeling effort, namely direct fuel injection and combustion, the time step size is reduced to 0.1 °CA ($1.1 \cdot 10^{-5}$ s) and 0.25 °CA ($2.75 \cdot 10^{-5}$ s), respectively.

4.1.2. 1D Gas Exchange Analysis

The 3D-CFD engine simulation is combined with a 1D gas exchange analysis to provide detailed flow boundary conditions. For this analysis, the 1D gas dynamics and thermodynamics code GT-Power from Gamma Technologies is used [93]. The goal of the analysis is to calculate the gas exchange and the associated combustion process inside the cylinder. The calibrated model can then be used to determine mass flow inlet and exhaust pressure outlet boundary conditions, which are essential for the 3D-CFD flow simulation.
In the so-called “Three-Pressure-Analysis” (TPA) method, measured instantaneous inlet and outlet pressures and instantaneous in-cylinder pressure are used for this purpose. At its core, the method is based on two run modes, the “Forward Run” and “Backward Run”. The “Forward Run” describes the classic procedure in which the cylinder pressure and heat transfer in the cylinder are calculated using a fixed burn rate. The “Backward Run”, on the other hand, acts in reverse. With a fixed cylinder pressure and heat transfer, the appropriate combustion rate is determined.
In the TPA, both modes are run alternately within one cycle. Starting from the time of closed inlet valves (IVC), a burn rate is first predicted in a “backward run” on the basis of the trapped fuel mass, the heat transfer of the previous cycle and the measured pressure curve. Using the determined rate, the calculation continues in a “forward run” and an updated heat transfer and gas exchange is calculated. The procedure is repeated over several cycles until a converged solution is reached.
The flow modeling in this analysis is performed using a network of 0D/1D elements in which conservation equations for mass, momentum and energy are solved. Measured inlet and outlet pressures serve as external boundary conditions for the system. The combustion model is based on a two-zone combustion methodology. For this purpose, the cylinder volume is divided into two zones, unburnt and burnt. At the start of combustion, mass is transferred from one zone to the other at each time step, according to the burn rate derived from the TPA analysis. The composition of the burnt zone can be determined from chemical equilibrium calculations. Finally, using the respective compositions of both zones, the zone temperature and cylinder pressure

can be determined at each time step. To consider heat transfer, the WoschniGT model [93] is used. It is based on the classical Woschni correlation [94] but has been adapted to include additional heat loss due to the gas exchange.

The model used in this work for the investigation of the optically accessible research engine is based on the preliminary work of Neumann [95] and Hain [96] and was adapted for the operating point described in section 3.1. The flowchart of the model used is shown as an example in Figure 4.3.

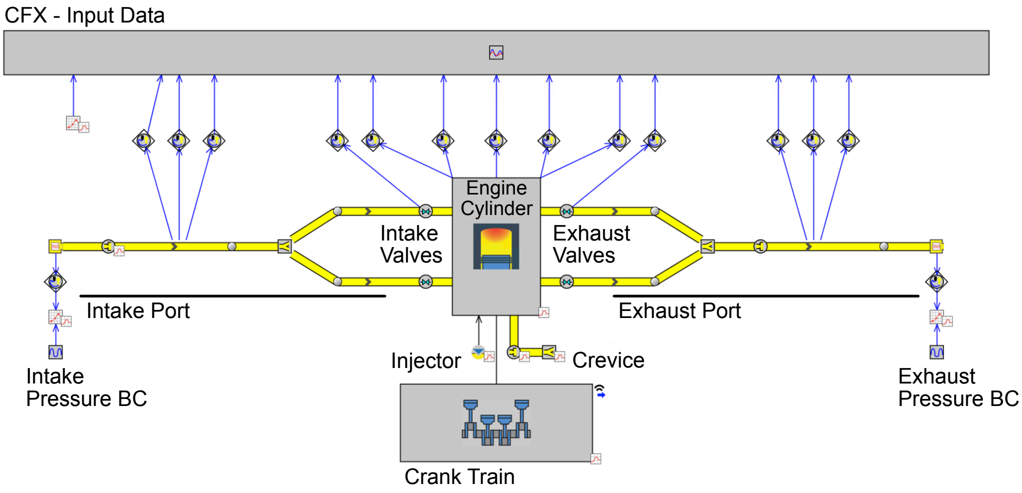

Figure 4.3.: Simplified flowchart of the 1D gas exchange model of the optically accessible research engine.

The intake and exhaust pressures required as boundary conditions for the TPA are based on ensemble-averaged measured data from a total of 63 engine cycles of the operating point.

A noteworthy aspect of the simulation is the special consideration of the piston crevice volume. To ensure optical access, the investigated engine has deep-seated piston rings to prevent grinding on the quartz liner. A consequence of this design is a large crevice between the piston and cylinder liner, which influences the compression ratio of the engine and the heat loss. To account for these influences, the crevice volume is considered a separate volume in the engine model that allows pressure and temperature-dependent exchange of the cylinder charge between cylinder and crevice.

4.1.3. 3D-CFD Modeling Methods

All investigations in this work were carried out with the flow solver ANSYS® CFX® (2021.2/2022.2). The solver has already been used several times for the simulation of internal combustion engines [34, 97–100] and includes several submodels for considering all relevant physical effects.

The node-based finite volume solver is employed with an implicit second-order Euler method for temporal discretization. To discretize the advective fluxes, a flux blending scheme *High Resolution* is used. The blending factor used to blend locally between first- and second-order scheme is adjusted to ensure the boundedness of the solution [25]. The mass flow is evaluated so that a pressure-velocity coupling is achieved. The system of discretized equations is solved using an Incomplete Lower-Upper (ILU) method and a coupled algebraic multi-grid approach.

To account for turbulence, an unsteady Reynolds-averaged Navier Stokes (URANS) approach with a shear-stress-transport (SST) model is applied. A detailed description of the model is given in Chapter 2.2.2.

To simulate the entire engine cycle, additional models are employed that consider all relevant phenomena along the engine cause-and-effect chain (cf. Chapter 2.1.2). Direct fuel injection into the engine cylinder is modeled using an Euler-Lagrange approach. The relevant parameters were determined using an adapted spray model based on spray chamber measurements and were provided by the manufacturer for use in this work. The injection duration determines the injected fuel mass and is controlled to match the required air-fuel ratio. The droplet evaporation and spray-wall interaction with the cylinder liner and piston walls are modeled according to the models presented in Chapter 2.2.3. A previous study by Salenbauch et al. [101] investigated the influence of different ethanol blends on mixture formation and successfully applied the presented spray modeling approach.

The decisive factor for the interaction of the fuel spray with the combustion chamber walls is the wall temperature. In contrast to the conventional operating conditions of a series engine, the research engine investigated in this section is operated only briefly in the part-load range due to the optical access. Therefore, the existing wall temperatures may deviate from typical values assumed for full-metal engines in steady-state operation. For this reason, the wall temperatures used in this work were estimated based on supporting 1D heat transfer simulations. As expected, the results described in Reusch [102] show significantly lower piston and cylinder liner wall temperatures. Based on this evaluation, constant wall temperatures of 380 K at the aluminum piston surface and 345 K at the quartz piston window were assumed for the 3D-CFD simulation over the engine cycle. For the quartz cylinder surface, the temperature was set linearly as a function of height between 380 K and 335 K.

Mass flow inlet and exhaust pressure outlet boundary conditions are determined from the previously introduced GT-Power 1D gas exchange analysis. Another aspect that is particularly relevant for the simulation of optically accessible research engines is the consideration of the large piston crevice volume. Since the crevice volume is not included separately in the 3D engine geometry, the mass flow between the cylinder and piston crevice monitored in the 1D gas exchange analysis is imposed on the 3D model as an additional boundary condition.

To simulate premixed turbulent combustion in the engine cylinder, a G-equation level-set model is used. The implementation in ANSYS® CFX® for combustion engine simulations was introduced by Toninel et al. [34]. A further description of the method is given in Chapter 2.2.4 of this work.

In order to model soot particle formation, a detailed quadrature method of moments (QMOM) approach, as discussed in Chapter 2.3, is utilized. The detailed modeling of soot particle formation and oxidation requires an accurate description of the combustion process and the resulting gas phase, including soot precursors and oxidizer species, even as far as behind the flame front. The close coupling required for this with the combustion model used is described in more detail in the following section.

4.1.4. Combustion and Coupled QMOM Approach

The G-equation combustion model used in this work is based on the principal idea of tracking the propagating flame front using a level-set approach [31]. This flame front acts as an interface that separates the unburnt and the burnt regions. It is represented by an isosurface G_0 of a scalar quantity G, indicating the main reaction zone (i.e., the flame). Smaller and larger values of G ($G < 0$ and $G > 0$) describe fresh and hot gases in the combustion chamber, respectively. Transport equations as derived by Peters [31] are solved for the mean value $\tilde{G}$ and the variance $\widetilde{G''^2}$. The solution requires the turbulent burning velocity s_T, which is a function of the laminar burning velocity s_L and the laminar flame thickness l_f. Both parameters are related to the respective thermochemical conditions and the fuel considered. Ewald [33] proposed an analytic approach to determine both variables for pure iso-octane. However, for the experimental conditions in this work, a surrogate fuel for gasoline was used; hence, these former correlations cannot be used directly. Instead, we determine s_L and l_f with 1D simulations of freely propagating surrogate/air flames and then tabulate the results as a function of the unburnt temperature $\tilde{T}_u$, the pressure p and the mixture fraction $\tilde{Z}$.

The mass fraction of different chemical species in the unburnt and burnt regions is evaluated following

$$\tilde{Y}_i = (1-c)\tilde{Y}_{i,u} + c\tilde{Y}_{i,b}\,, \tag{4.1}$$

where c describes the reaction progress that is evaluated from $\tilde{G}$ and $\widetilde{G''^2}$, assuming that the distribution of G can be approximated using a Gaussian distribution (cf. Chapter 2.2.4). The Favre-averaged burnt mass fraction of a certain species $\tilde{Y}_{i,b}$ is usually evaluated assuming equilibrium [34]. While this is sufficient for the kinematics of turbulent flame propagation [33], it is not suitable to describe the evolution of soot precursors such as pyrene (A4-$C_{16}H_{10}$) in premixed combustion configurations. This is demonstrated in Figure 4.4, where results of a 1D simulation of a sooting premixed surrogate/air flame show that the soot precursors pyrene (A4-$C_{16}H_{10}$) and acetylene (C_2H_2) slowly approach their equilibrium value in the post flame

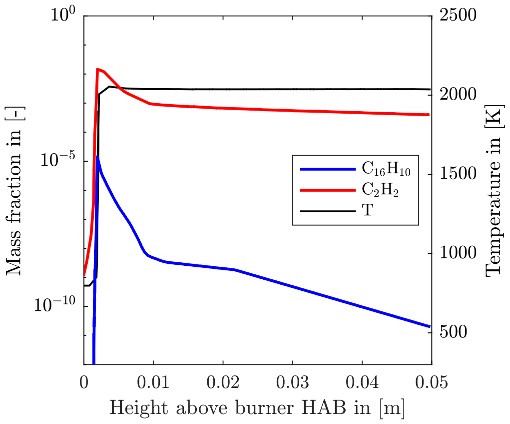

Figure 4.4.: Examplary simulation results for the mass fraction profiles for C_2H_2 and pyrene (A4-$C_{16}H_{10}$) over the height above the burner (HAB) for a 1D premixed surrogate/air flame with an equivalence ratio $\phi = 2.0$, $T_u = 800$ K, $p = 10$ bar. The temperature profile indicates the flame front and the subsequent post-flame zone.

zone. In contrast, for the specific case shown, their concentration peaks around the main reaction zone, followed by a slow descent towards their equilibrium value, which in the case of pyrene is several orders of magnitude smaller. The standard approach based on Equation 4.1 and the equilibrium assumption cannot capture these effects. Instead, the pyrene concentration in the main reaction and the post-flame zone would be significantly underestimated. Thus, we replace the equilibrium values of $\tilde{Y}_{i,b}$ of soot-related gas phase species (e.g., for C_2H_2, pyrene) with the maximum values occurring in the premixed flame zone in the flamelet table, which are also tabulated from 1D premixed flame simulations.

For the decay of the soot-related gas phase species in the post-flame zone, an additional progress variable c' is introduced. Within the framework of this work, a composition of the averaged variable in parts of C_2H_2 and OH species with the ratio $\widetilde{c'} = 2\tilde{Y}_{\mathrm{C_2H_2}} + 0.2\tilde{Y}_{\mathrm{OH}}$ has proven to be suitable. To describe the evolution of $\widetilde{c'}$ in the 3D-CFD simulation, we use an additional transport equation in analogy to the species transport.

The source term $\dot{\widetilde{c'}}$ responsible for the decay of the progress variable, as well as the relevant soot-related species mass fractions (C_2H_2, A4-$C_{16}H_{10}$, and OH), are tabulated along the progress variable itself and as a function of $\tilde{T}_u$, p, $\tilde{Z}$, and the variance of the mixing fraction $\widetilde{Z''^2}$ using 1D premixed flames. To ensure a unique representation of the thermo-chemical state, a monotonic progression of the progress variable is required. For this reason, only the area behind the peak value of the progress variable in the main reaction zone is considered for tabulation. A switch of the species determination between its increase, described by the equilibrium approach of the combustion model, and its decrease in the post-flame region, represented by the additional progress variable $\widetilde{c}'$, is carried out at a reaction progress of $c = 0.5$. For a reaction progress of $c < 0.5$, the calculation of $\widetilde{c}'$ takes place based on the species definition by equation 4.1. For a reaction progress of $c \geq 0.5$, the transport equation involving the tabulated source term is used to represent the evolution of the progress variable.

The description of the soot particle moments $\overline{m}_k$ is also done by introducing additional transport equations in the 3D-CFD simulation. The influence of the physico-chemical processes discussed in Chapter 2.3 by nucleation, coagulation, surface growth and oxidation on the individual moments is represented by their source terms $\dot{\overline{m}}_k$. The source terms are calculated on-the-fly for each control volume based on the thermo-chemical state, including all soot-relevant species mass fractions and the current moments of the soot particle distribution. A detailed description of the determination of the moment source terms can be found in the work of Salenbauch [35].

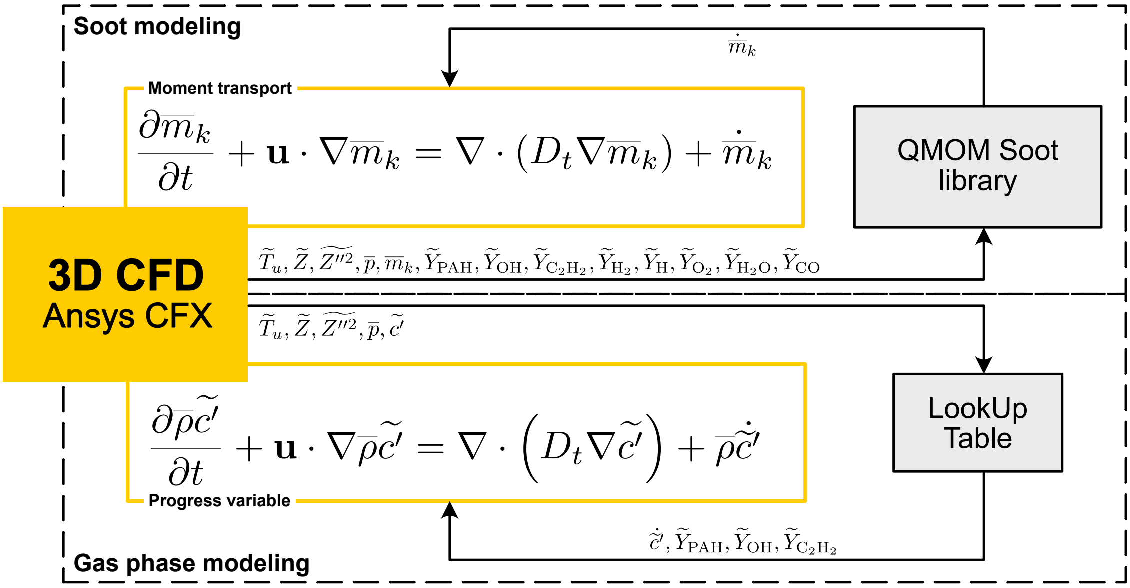

Figure 4.5.: Schematic description of the CFD solver - QMOM coupling.

In summary, the adjustments made in the 3D-CFD model are shown in Figure 4.5. The coupling of the moment-based soot model includes the transport of two additional transport equations for the moments of the soot particle distribution and an additional transport equation to describe the decay of soot-relevant species in the post-flame zone. The thermochemical state is represented by three tables: A table describing the equilibrium state before and after combustion, a table describing the laminar flame velocity and flame thickness to calculate the turbulent flame velocity in the G-equation model, and a table describing the soot-relevant species in the post-flame zone. The moment source terms are evaluated on-the-fly by the coupled QMOM soot library.

4.2. Model Evaluation Based on a Steady-State Operating Point

The evaluation of the 3D-CFD engine framework is based on a steady-state operating point of the optically accessible research engine. It is characterized by a part-load operation at 1500 rpm and a late fuel injection at SOI = 140 °CA bTDC. Both experimental and numerical studies were performed with the same surrogate fuel TolIso (65 vol.% isooctane and 35 vol.% toluene). A detailed description of this operating point is given in section 3.1. For the qualitative comparison of the fuel injection, experimental spray extinction measurements were used. The soot model is evaluated based on soot luminescence and quantitative extinction measurements. LTT Erlangen provided all experimental data presented in this chapter.

In the first step of the analysis, a look is taken at the processes along the chain of action preceding the formation of soot, namely the fuel injection and subsequent mixture homogenization. In the second step, the resulting formation of soot particles in the engine domain is compared with experimental data and the processes underlying these observations are analyzed in more detail.

4.2.1. Fuel Injection and Mixture Formation

The injection timing relative to the engine cycle and the resulting dispersion and propagation of fuel droplets through the combustion chamber has an important impact on the mixture homogenization and, therefore, on soot particle formation.

For the operating point under consideration, a late injection timing was chosen, with the start of injection (SOI) at 140 °CA bTDC, in the early compression stroke with the piston far away from the cylinder head. The purpose of this measure is to reduce the spray–wall interaction, especially when compared to early injection timings, and to avoid a prolonged wall film. However, the opposite effect may occur if the injection duration is too long. The piston moves again towards the top dead center during the compression phase and can intersect the zone of the liquid injection cone again. To ensure this behavior is correctly represented in the simulation, experimentally measured spray extinction images are first compared with line-of-sight (LOS) integrated CFD results.

Figure 4.6 (left) shows the direct comparison of experimentally and numerically determined results. Further information about the positioning of the experimental field of view (FOV) is given by projection onto the numerical domain in Figure 4.6 (right). The first comparison of CFD and experimental results in the FOV shows good agreement in terms of both spray targeting and timing. The CFD calculation provides further information outside the FOV. Figure 4.6 (right) indicates that there is an interaction between the spray, the cylinder liner and the piston walls.

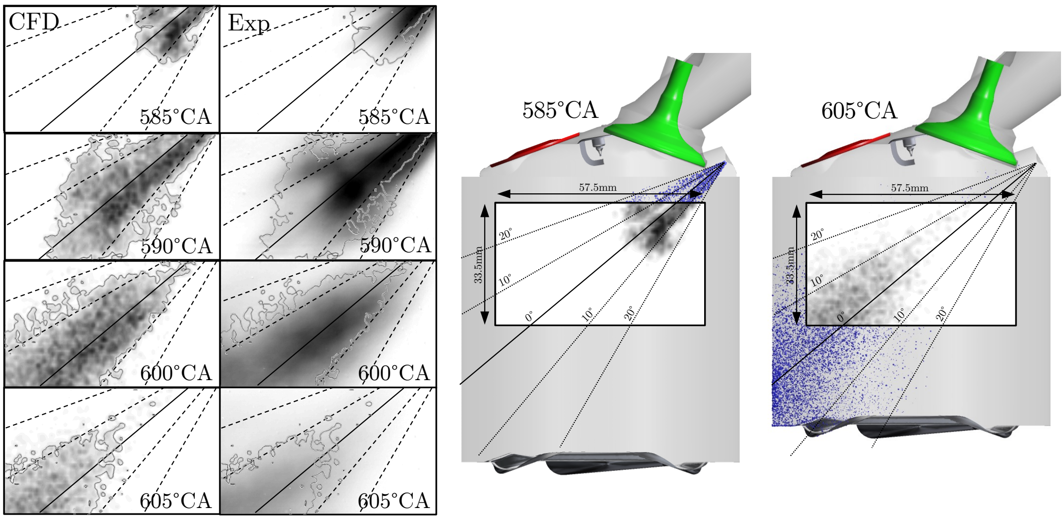

Figure 4.6.: Left: Comparison of spray extinction measurements with LOS-integrated CFD results. Right: Position of the field of view (FOV) based on the example of two different crank angles.

To quantify how much fuel is deposited on the walls, the detailed distribution of the fuel mass in the domain was evaluated. Figure 4.7 (top) provides information on the overall fuel mass balance in the cylinder, while Figure 4.7 (bottom) depicts the distribution of the wall film mass between the cylinder liner and the piston surface. Wall film formation occurs 15 °CA after the

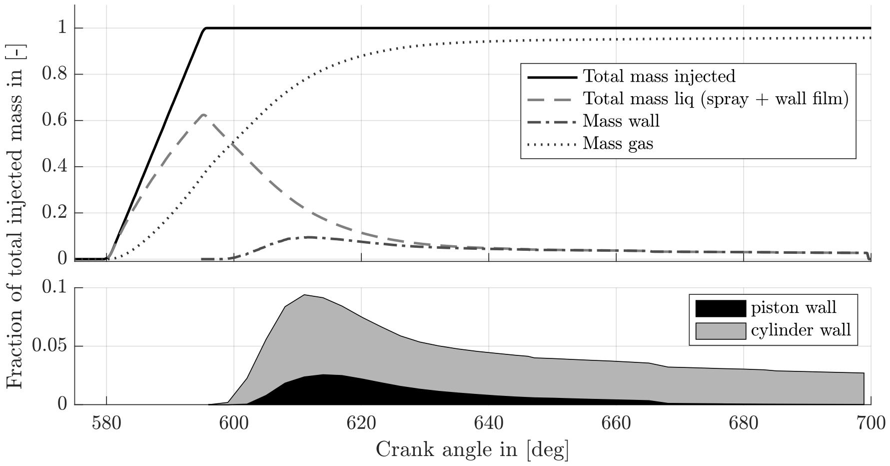

Figure 4.7.: Top: Mass distribution between liquid and gaseous fuel after injection. Fractions of liquid and gaseous mass are summed up to the total amount of injected fuel mass. The fraction of liquid fuel mass includes the mass bound to the wall film. Bottom: Further distribution of wall film mass between piston and cylinder surface.

start of injection. Most of the fuel film forms on the cylinder liner due to the spray targeting; additional wall film formation occurs on the piston surface. As the injection process continues, the wall film mass increases until it finally reaches a maximum of 10% of the total injected fuel mass at 611 °CA. Subsequent evaporation of the liquid fuel is delayed due to the cold walls. The evaporation of the wall film causes a local enrichment of the mixture and thus counteracts homogenization. This becomes particularly clear by taking a closer look at the cylinder regions with a high equivalence ratio, as depicted in Figure 4.8 (top section). The mass fraction of the mixture in the cylinder with an equivalence ratio higher than $\phi > 1.7$ is plotted along the crank angle. The mass fraction already burned is indicated by the hatched area. Despite an initial decrease as mixing proceeds, a very fuel-rich mass fraction of 8.9% remains in the domain at the ignition time. Figure 4.8 (bottom section) reveals the location of the fuel-rich mixture. In this graphic, the region with an equivalence ratio higher than $\phi > 1.7$ is highlighted in blue; the propagation of the flame front after ignition is represented by the reaction progress at 0.02 in red. The region with the highest equivalence ratio corresponds not only to the area in which wall film formation occurs but also to the experimentally and numerically identified zone of increased soot particle formation. It can be seen how the flame propagates between 710 °CA and 720 °CA through this particularly fuel-rich region, initiating the rapid increase in soot volume. This will now be analyzed in more detail.

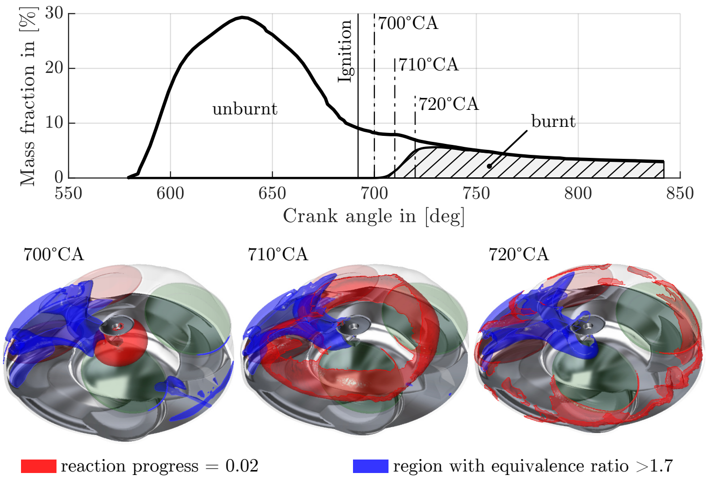

Figure 4.8.: Top: Mass fraction of mixture with equivalence ratio higher than 1.7 along the engine cycle. The hatched area indicates the already burnt fraction of fuel-rich mixture. Bottom: Flame progress through the fuel-rich mixture. Regions with an equivalence ratio higher than 1.7 are depicted in blue. The flame front is visualized by the reaction progress variable at 0.02 in red.

4.2.2. Soot Particle Formation

To evaluate the coupled moment-based soot model described in the previous section, the calculated soot volume fraction field is line-of-sight (LOS) averaged and compared with the available quantitative soot extinction measurements. Since these can only detect soot in a restricted field of view (FOV) below the cylinder head region, qualitative luminescence measurements are also used. These measurements can detect luminescence over a large region, even in the vicinity of the cylinder head, and thus allow general orientation and the detection of possible soot foci. Figure 4.9 (1st row) shows both measurements combined for three different crank angles. The "FOV Extinction" cutout indicates the FOV of the quantitative extinction measurements, while the luminescence measurements are shown as a supplement in the entire cylinder head area. The colormap of the luminescence measurements is inverted for better comparison. The second row depicts the LOS-averaged numerical soot volume fraction field. For better orientation, the experimental FOV is also highlighted in the numerical results.

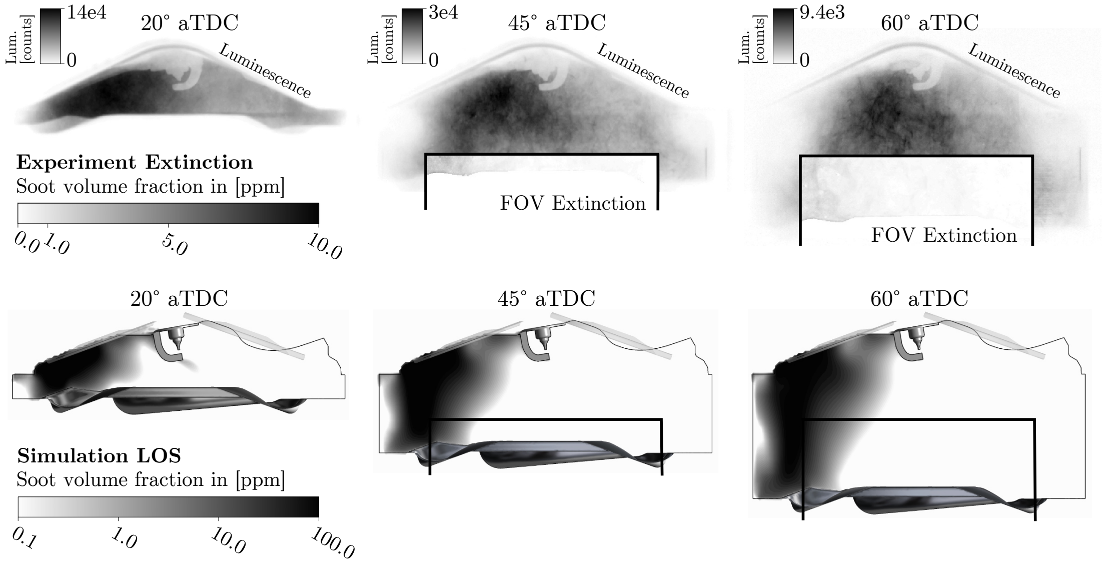

Figure 4.9.: Detailed comparison of the soot distribution between experiment and simulation for several crank angles. The experiment (top row) shows the soot luminescence and additional soot extinction measurements in the box at the bottom part of the cylinder. The simulated soot volume fraction is for comparison line-of-sight (LOS) integrated and averaged (bottom row).

The luminescence measurements reveal increased luminescence, mainly on the left side of the cylinder head right below the exhaust valves. With increasing time, the overall signal decreases, and the soot cloud drifts slightly to the center of the cylinder. The extinction measurements confirm the trend toward increased soot formation on the left side of the cylinder. However, the signal does not indicate that the soot cloud drifts toward the center of the cylinder. The simulation can predict similar trends to those observed in the experiment. The primary source of soot is located on the left side, just below the exhaust valves. As the cylinder expansion progresses, this area is stretched, with the lower end continuing to attach to the piston surface. As time progresses, the soot cloud is drawn into the experimental FOV. The extinction measurement can confirm this observation. An expansion of the soot cloud in the upper region of the cylinder can also be noted. However, the dimensions observed in the luminescence measurements cannot be reproduced in this case.

The QMOM modeling approach allows the evaluation of the soot volume fraction and soot number density. From both, an average soot particle diameter can be calculated.

In Figure 4.10, three-dimensional views of the cylinder, including two orthogonal sectional planes, are shown with the soot volume fraction (left), mean soot particle diameter (center) and equivalence ratio (right) for 780 °CA. As observed in the extinction measurements, the soot plume is mainly located on the left of the combustion chamber. This region is characterized by an exceptionally high equivalency ratio caused by previous mixing processes described in the previous section. In regions away from this very fuel-rich mixture plume, the potential for soot formation decreases rapidly as the equivalence ratio decreases. The distribution of the mean particle diameter in the domain resembles the soot volume fraction. The highest mean diameter of 100 nm is found right in the plume, while the diameter decreases with increasing distance.

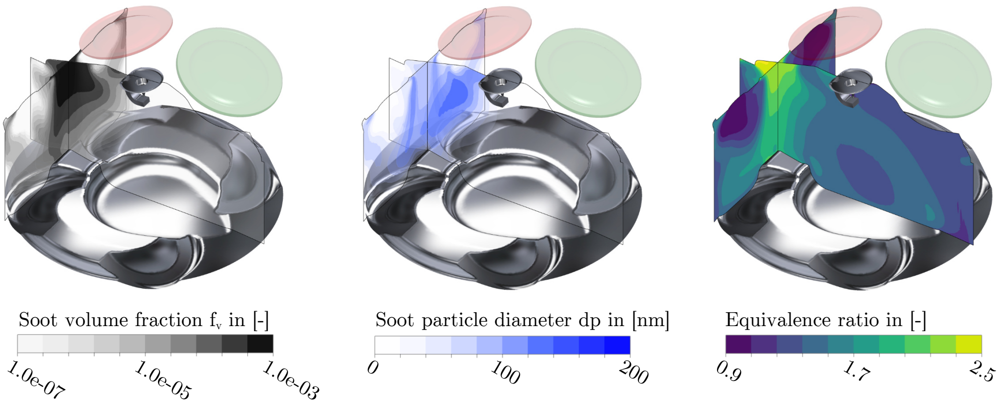

Figure 4.10.: Three-dimensional view of the engine cylinder at 780 °CA divided by two sectional planes. Left: Soot volume fraction predicted by the moment-based soot model. Center: Corresponding mean soot particle diameter. Right: Equivalence ratio of the air-fuel mixture.

Formation of soot precursors

The integrated soot volume over the entire engine domain is depicted in Figure 4.11. The initial increase of soot volume starts between 720 °CA and 730 °CA. At that moment the flame front enters the fuel-rich region, and soot precursors begin to form in the burnt zone behind. Subsequently, the soot volume increases until it reaches its maximum value at 778 °CA. From this point, oxidation effects dominate, and the integrated particle volume decreases again.

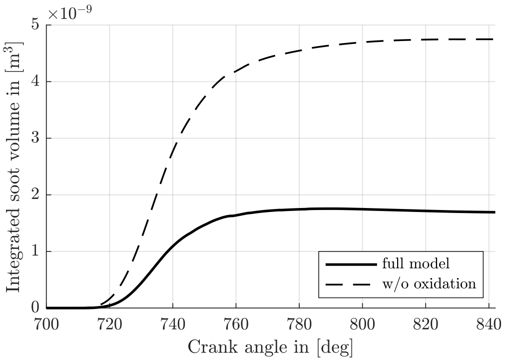

Figure 4.11.: Total soot volume in the cylinder taking into account all physico-chemical processes (solid line). For the assessment of oxidation effects in the next section, this curve is compared with the total soot volume neglecting oxidation processes (dashed line).

Figure 4.12 depicts the soot volume fraction f_v (left column), the air-fuel equivalence ratio (center column), and the relevant soot precursors acetylene, pyrene and the oxidizer OH (right column) on the tumble plane (symmetry plane) for the early combustion stage. As can be seen, the initial soot formation starts solely on the left side, slightly delayed behind the flame front. As time passes, the soot volume increases. A look at the underlying species profiles (right column) reveals the causes of the increased formation. The soot-promoting precursor acetylene (C_2H_2 in red) is formed right behind the flame front. Depending on the local equivalence ratio, larger PAHs are formed as well. The concentration of the representative PAH pyrene (A4-$C_{16}H_{10}$ in orange) increases especially on the left side of the domain, promoting the nucleation of soot particles. By contrast, the predominant species on the right side of the domain is OH (in green). Soot nuclei behind the flame front are quickly oxidized in this lean environment. Thus, no relevant particle formation can be detected on the right side of the domain.

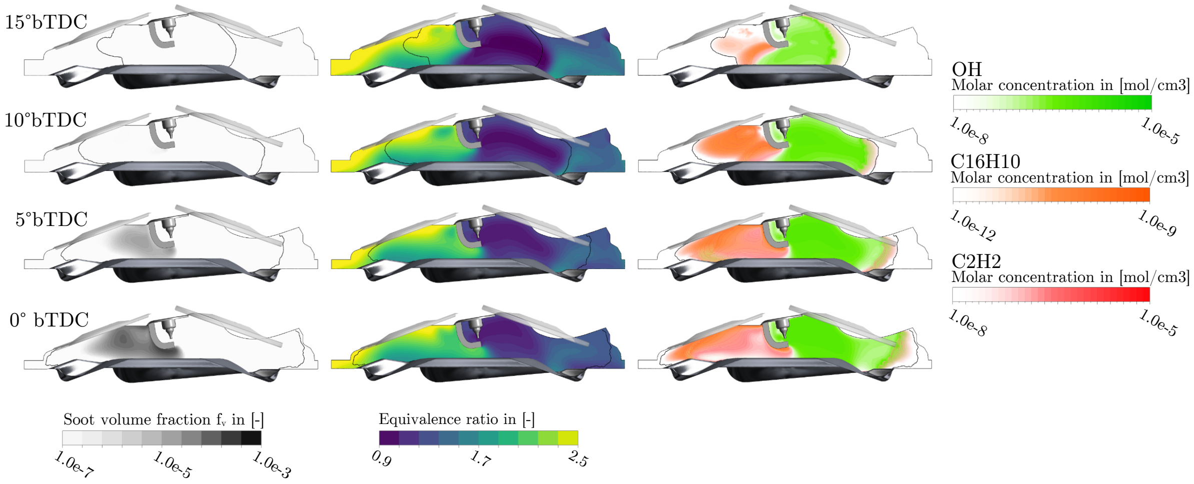

Figure 4.12.: Soot volume fraction f_v, air-fuel equivalence ratio and soot precursors are depicted on the tumble plane of the engine domain for four different crank angles during combustion. The black line highlights the flame front at a reaction progress of 0.02. Important precursors (C_2H_2, A4-$C_{16}H_{10}$, and OH) are depicted together (color-coded) in the right-hand column.

To depict the increase and subsequent decrease in soot-promoting precursors behind the flame front, cell data on the tumble plane for six equidistant crank angles from 700 °CA to 750 °CA were combined and evaluated according to their distance to the flame front. The averaged and normalized molar concentration of each soot-promoting precursor species is depicted in Figure 4.13. The data are plotted separately depending on the locally encountered equivalence

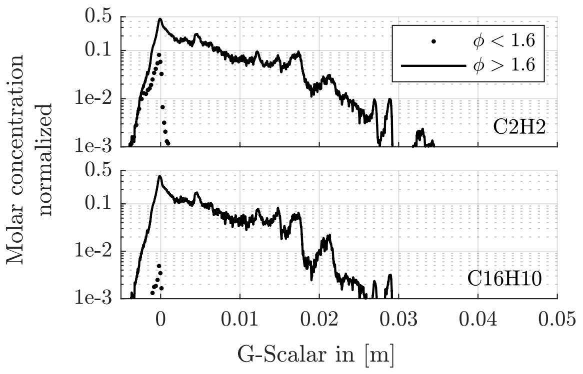

Figure 4.13.: Formation and reduction of soot precursors acetylene (C_2H_2) and pyrene (A4-$C_{16}H_{10}$) in the flame zone. The Figure depicts the average local molar concentration normalized with the maximum value occurring over the distance to the flame (G-scalar). Data is evaluated for each cell on the tumble plane and combined for six equidistant crank angles from 700 °CA to 750 °CA.

ratio above or below $\phi = 1.6$.

It becomes clear that the peak value of the precursors in the flame front for different equivalence ratios differs significantly. The highest values are achieved in the most fuel-rich regions. For stoichiometric to moderately rich equivalence ratios ($1 < \phi < 1.6$), the concentration of precursors first increases inside the flame brush and then rapidly decreases. The decrease for higher equivalence ratios ($\phi > 1.6$) emerges more slowly and at larger distances to the flame front. In these regions behind the flame front, where significant concentrations of acetylene and pyrene are present, initial soot nuclei are formed.

Assessment of oxidation effects

As can be observed in Figure 4.12, certain areas show no or minimal occurrence of soot particles. This is especially obvious for areas with high OH concentrations. To evaluate this in more detail, the impact of the oxidation term is studied next. For this purpose, the oxidation term was deactivated in an additional numerical experiment, and the resulting soot volume fraction was compared with the reference case (including oxidation).

The integrated soot volume obtained neglecting the soot oxidation processes is added to Figure 4.11 to compare the two models. Oxidation leads to a significant reduction in the total soot volume. Both the rate at which soot formation occurs and the peak volume are reduced. Neglecting the soot oxidation effects results in a significant increase in soot volume. The maximum value is reached at the end of the combustion cycle at 840 °CA with 4.75e-9 m^3 and is 2.65 times larger than the maximum value reached for the case with activated oxidation. This shows that oxidation not only leads to a reduction in soot volume in a downstream process but also competes with soot-promoting mechanisms at an early stage. From a crank angle of 780 °CA onwards, oxidation and formation processes balance each other out, and even a slight decrease in the integrated soot volume can be observed.

Figure 4.14 shows the calculated soot volume fraction without considering oxidation for 780 °CA (left). The difference between both, the simulation with and without oxidation, is presented in the center. It can be seen that soot oxidation occurs in the entire engine domain. An evaluation comparing the reduction to the total soot volume fraction (right) shows that complete oxidation occurs in most regions, especially in areas with an initially small soot volume.

Although the simulated regions of increased soot formation agree broadly with the experimentally collected data, the exceptionally high threshold for the presence of soot indicates an overestimation of the oxidation rate. This is consistent with the known high uncertainty of these rates, especially at the pressures present in the engine. Therefore, improving the prediction of oxidation effects in the context of an engine is the subject of intense research.

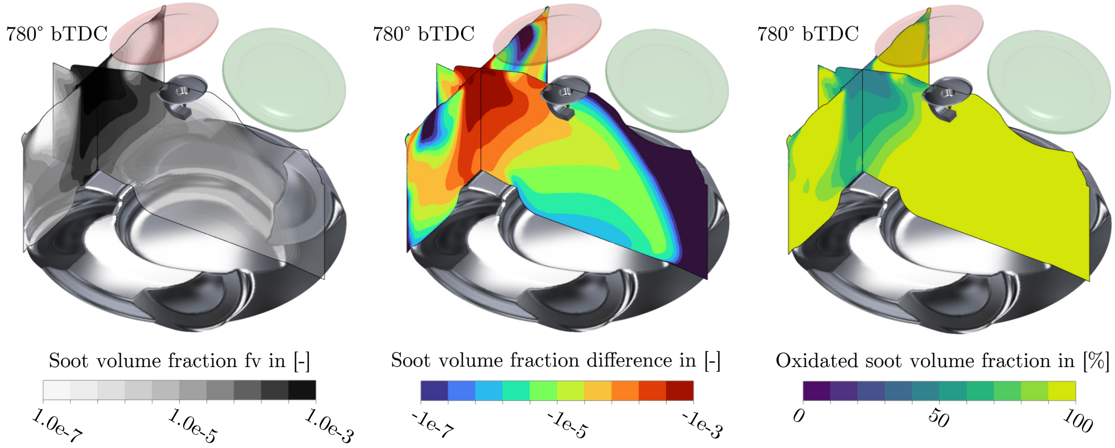

Figure 4.14.: Influence of oxidation on the soot volume fraction inside the engine. Left: Calculated soot volume fraction without oxidation taken into account. Center: Difference in soot volume fraction between simulations with and without oxidation. Right: Relative reduction of the soot volume in relation to the local soot volume fraction without considering oxidation effects.

4.3. Summary and Closing Remarks

To approach the 3D-CFD simulation of soot formation under transient engine operation, this chapter first presented a framework of methods and models for simulating soot particle formation and oxidation in the internal combustion engine, including all relevant processes along the engine cause-and-effect chain. Subsequently, the model was evaluated based on a sooting operating point of an optically accessible research engine and available measurement data.

The framework, which is based on the ANSYS® CFX® flow solver, works with a number of specifically implemented approaches and models for the simulation of internal combustion engines and is supplemented in this work by a model for the accurate simulation of soot particle emissions.

A quadrature method of moments (QMOM) soot model was coupled to the flow solver to describe the evolution of the polydisperse system of soot particles taking into account relevant physico-chemical processes such as nucleation, coagulation, surface growth and oxidation of soot particles. Two additional transport equations are solved by the flow solver for the description of the statistical moments of the particle size distribution. The evaluation of the source terms of the respective moment equations is based on the reconstructed distribution, the thermo-chemical state and the underlying gas phase composition. Furthermore, an additional progress variable was introduced that allows an accurate representation of the gas-phase soot precursor and oxidizer species and describes their slow decay behind the flame front based on a detailed gas-phase mechanism. To characterize the operating point under investigation and provide detailed inflow and outflow boundary conditions, 1D gas exchange simulations were carried out based on high- and low-pressure measurements of the operating point on the engine test bench.

The application of the framework to the considered operating point demonstrated that it is able to represent the entire soot formation cause-and-effect chain and thus allows not only the simulation of soot but also the investigation of its root causes. A detailed analysis of the cause-and-effect chain along the engine cycle revealed how soot formation originates from late fuel injection and spray-wall interaction with the cold combustion chamber walls. The hereby occurring locally very fuel-rich region below the exhaust valves is an essential source of the observed emissions which agrees with the experimental observations from optical extinction and luminescence measurements. In addition, the influence of the oxidation process on the simulated soot formation was investigated. The particularly large influence up to complete oxidation in regions with only moderate amounts of soot indicates an overestimation of the oxidation rates.

The results demonstrate that the presented framework provides a comprehensive platform for investigating the sources of particulate emissions in complex engineering applications such as the internal combustion engine. In the following part of this work, the framework will be supplemented for the investigation of particulate emissions in the context of transient engine operation.

5. Extension of Methodology to Transient Engine Operation

This chapter extends the introduced simulation framework in Chapter 4 to transient engine operation. To this end, the challenges associated with consecutive engine cycles and changing boundary conditions are addressed and solution approaches and methods are presented.
First, a look is taken at handling experimental reference data from individual realizations of a transient engine event. Based on a proposed averaging method, an extension of the 1D gas exchange analysis from Chapter 4.1.2 is introduced to generate further boundary conditions for several consecutive engine cycles. Finally, the topic of increasing simulation costs for very long transient engine events is addressed by an efficient method for partitioning into multiple threads.

5.1. Methodology

5.1.1. Handling of Transient Boundary Conditions

The simulation of transient scenarios requires precise knowledge of the underlying conditions inside the engine. For this reason, both general boundary conditions (cylinder pressure, intake/exhaust pressure, oil temperature, etc.) and boundary conditions controlled by the engine control unit (injected fuel, injection timing, air/fuel ratio, etc.) are recorded on the highly dynamic engine test bench and made available to the simulation side. To make this information actually suitable for the application in the 3D-CFD simulation, averaging over a sufficient number of engine cycles is required. In contrast to ensemble averaging at the steady-state operating point, where each cycle is operated at the same load and speed, in transient engine operation each realization of the transient scenario begins at a slightly different crank angle position. This results in a relative shift of the in-cylinder pressure signal, which makes considering the whole transient scenario for an ensemble averaging impossible. Fig. 5.1 illustrates this, showing three realizations of the same representative transient.
For this reason, a cycle-based averaging approach is used in this work. First, all measured

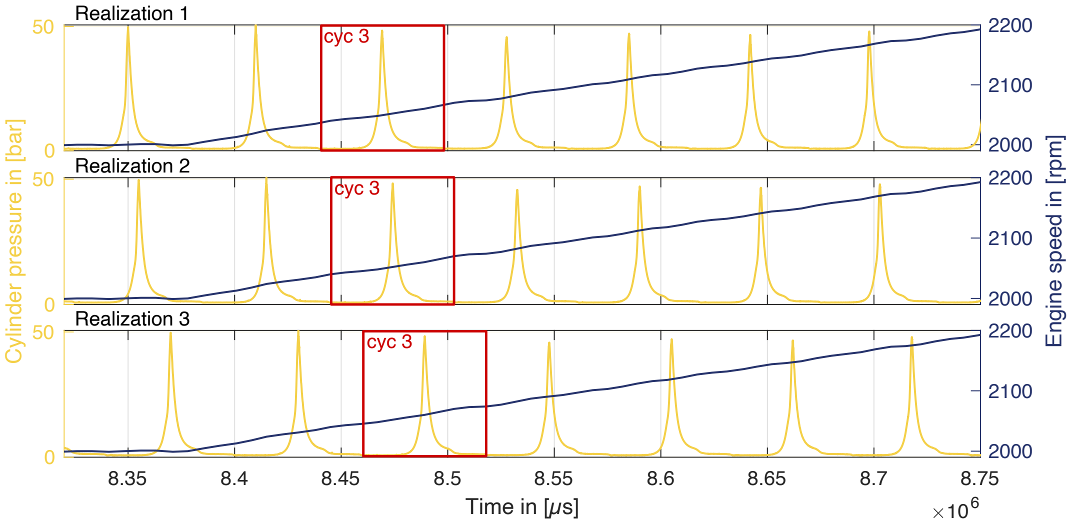

Figure 5.1.: Example of three different realizations of the same transient engine scenario. The transient scenario is reflected by the linear increase in the engine speed. Different crank angle positions at the start of the scenario lead to individual shifts of the cycle for each realization.

realizations of the scenario are synchronized in temporal space according to the event-defining transient parameter (e.g., the engine load and speed). In the next step, each cycle in each realization is assigned to a number corresponding to its placement in the transient. This allows the consideration of each cycle along its internal coordinate, the crank angle. Finally, an ensemble averaging of all cycles with the same rank can be applied. Figure 5.2 demonstrates these steps in an example with the cycle of rank 3 in the transient scenario (referred to as cyc3).

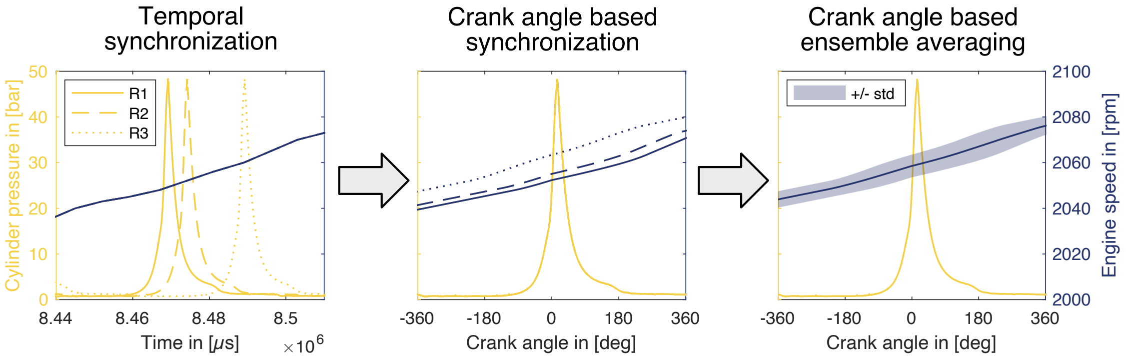

Figure 5.2.: Step-for-step procedure for the synchronization and ensemble averaging of multiple transient engine datasets.

A consideration in temporal space (left) demonstrates the characteristic shift in crank angle between different realizations. A synchronization according to the internal coordinate (center) allows for a reasonable averaging. However, this synchronization leads to a temporal shift of the realization itself, as can be seen in the engine speed signal. An ensemble averaging of the signal therefore results in a higher standard deviation for those signals (right).

The introduced error depends on the required shift for each individual realization and the dynamics of the transient engine scenario. In general, it can be said, that the error is marginal, as long as the time scale of the transient is much larger than the time scale of a single engine cycle.

For a better treatment of the individual cycles in the 3D-CFD simulation, the actually continuously changing engine speed is discretized by a cycle-averaged quantity. In this way, each cycle can be calculated at a steady engine speed in the transient engine simulation. In Figure 5.3 the discretization is shown exemplarily for a linearly increasing engine speed. Over the respective engine cycle represented by the indicated pressure (grey), the actually linearly increasing engine speed (blue, dashed) is replaced by an average constant speed (blue, solid).

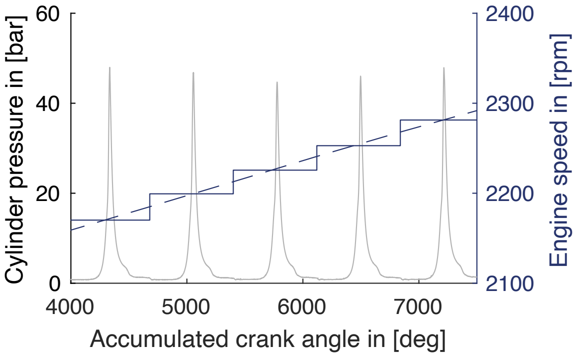

Figure 5.3.: Representative approximation of transient engine speed for individual cycles. Each cycle is treated with a constant engine speed represented by the average speed along the cycle.

5.1.2. Extension of the 1D Gas Exchange Analysis

In order to determine further boundary conditions for the 3D-CFD simulation, the ensemble averaging is followed by performing a gas exchange simulation based on the measured boundary conditions using the thermodynamics code GT-Power [93]. The starting point for the gas exchange simulations is a calibrated simulation model of cylinder 4 for steady-state operating points provided by the engine manufacturer. The model is based on a *Three-Pressure Analysis* (TPA), an iterative method that uses measured intake, exhaust and cylinder pressures to determine cylinder load and combustion profile. Wall temperatures are estimated in the model using a simplified FEM model based on oil and coolant temperatures. A detailed description of the individual solvers and models can be found in the software documentation [93].

To investigate transient engine operation, it is also necessary to consider the course of successive engine cycles. For this reason, the procedure for carrying out the gas exchange analysis was adapted and extended. The adapted method follows a three-step approach, which also considers changes in the wall temperature along the transient scenario. The approach is structured as follows:

- Step 1 Conventional TPA approach for calculating an initial steady-state operating point.
- Step 2 Independent calculation of the burn rates of all individual cycles along the transients using steady-state TPA at constant wall temperature determined in Step 1.
- Step 3 Calculation of the complete transients using the burn rates calculated in Step 2. Determination of the resulting cylinder load and wall temperatures.

Step 1 serves to initialize the analysis. Using averaged boundary conditions and pressure data of the steady-state operating point at the beginning of the transient scenario, an initial cylinder load and the corresponding wall temperature can be determined.

In *Step 2*, each individual cycle of the transient scenario is considered as an individual operating point and calculated with a steady-state TPA. For this step, it is assumed that the wall temperature is constant over the course of the transients. The temperatures determined in Step 1 serve as boundary conditions. The determined burn rates are used in the final step to calculate the total transient scenario.

Finally, in *Step 3* the transient calculation of the succession of cycles is performed. The cycles are calculated one after the other, with each cycle initialized with its preceding cycle. The calculation starts with the steady-state operating point determined in Step 1. No TPA is performed; instead, the measured inlet and outlet pressures and the burn rates determined in Step 2 are used for the calculation. The wall temperatures are calculated analogously to the reference model and initialized with the temperatures determined in Step 1.

The approach was first evaluated on the measurement of a generic transient engine scenario, a linear engine speed and load ramp, and shows good agreement in the calculated indicated mean effective pressure ($imep$). Figure 5.4 depicts the $imep$ along the engine transient. The calculated $imep$ can successfully reproduce the averaged experimentally measured values in most of the scenario. Only at the beginning of the transient do more significant deviations occur. However, a deviation of 10% is never exceeded.

The determined wall temperatures along the scenario are shown in Figure 5.5. It can be seen that, after an initial delay, the wall temperatures increase linearly far beyond the actual transient. The temperature change is slow and only by a few degrees during the entire period of study.

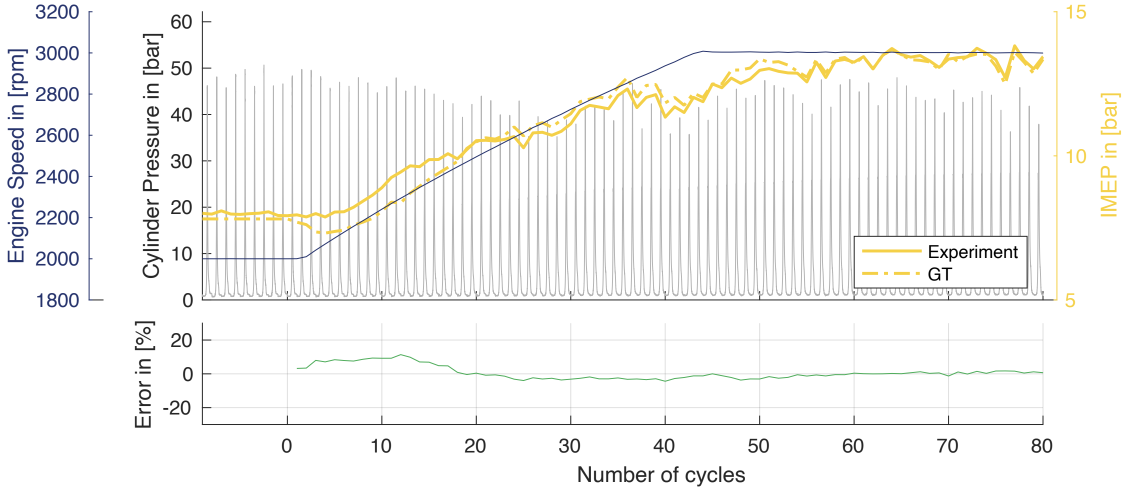

Figure 5.4.: 1D gas exchange analysis of a generic transient engine scenario, a linear speed and load ramp. Depicted is the engine load represented by the indicated mean effective pressure ($imep$) and the relative error between 1D analysis and experiment (in green).

Even though the actual wall temperatures under these operating conditions are not known and thus the results cannot be validated, the method provides a rough estimate of the effects of transient operating conditions on the trend of wall temperatures.

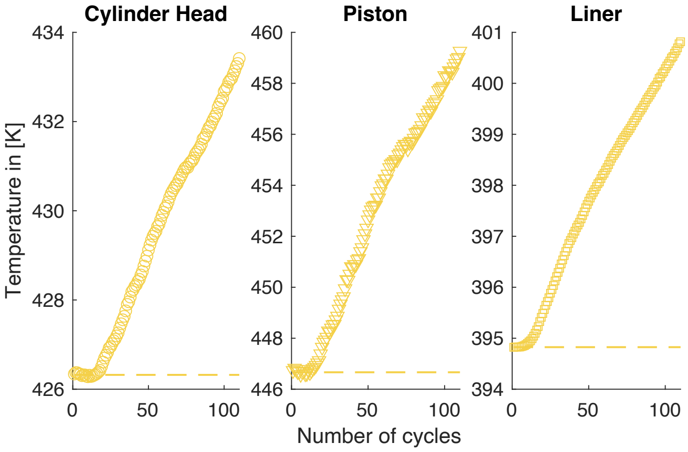

Figure 5.5.: Wall temperatures at the cylinder head, piston and cylinder liner surface from 1D gas exchange calculations of a linear speed and load ramp.

5.1.3. Thread-Based Simulation Approach

Another challenge in multi-cycle simulation is the efficient calculation of successive cycles. Since each cycle of the engine transient depends on the previous cycle, the cycles can only be computed one at a time, one after the other. In this section, possibilities of parallelization are discussed.
For the simulations carried out in this work, computing capacities were provided on the Hessian high-performance computer Lichtenberg II (Intel® Xeon® Platinum 9242) and on the institute's own high-performance computer (Intel® Xeon® Gold 6248). The computational effort for one cycle on the available processors is about 35h with a recommended parallelization of about 160 cores. A continuous calculation of the entire emission-relevant range (~80 cycles) for a transient engine scenario would thus extend to a period of approx. 3.7 months. To reduce computation time, parallelization into multiple independent threads is proposed. The procedure is shown in Figure 5.6 as an example of parallelization with 3 threads. The first three lines represent the sequence of computations along the engine cycles, while the bottom three lines represent the sequence of computations in real-time with parallelization applied.

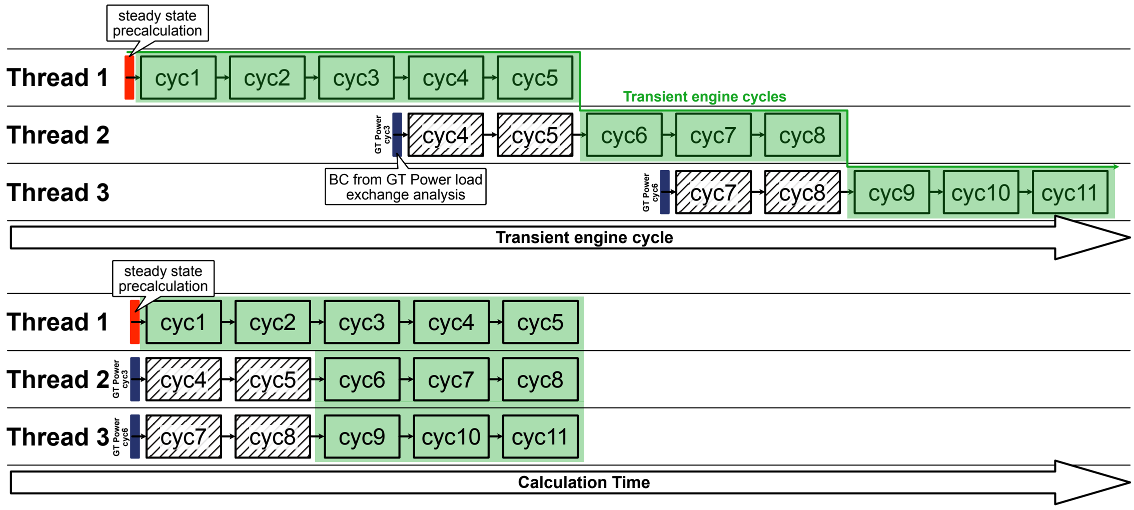

Figure 5.6.: Example of parallelization of a transient engine simulation with multiple parallel threads.

The exemplary engine transient, which consists of a series of successive cycles (boxes), requires approx. 22 days for the calculation of 11 cycles. By partitioning the cycles into several sections (threads 1-3) and starting all sections together, the total calculation time of the transient can be reduced considerably. The new challenge added due to the partitioning of the transients is to provide accurate initial conditions for the individual threads. In this work, the data from the previous 1D gas exchange simulations (in blue) is utilized for this purpose. Together with additional initialization cycles (hatched), they serve to initialize the thread. These initialization cycles overlap with the actual transient scenario and increase the overall computational effort.

5.2. Summary and Closing Remarks

In this chapter, the framework initially presented in Chapter 4 for studying soot particle formation and oxidation in the gasoline direct-injection engine was extended to analyze transient engine operation. Key elements of this extension deal with the preparation and handling of available experimental reference data, the calculation of transient intake and exhaust boundary conditions using 1D gas exchange simulations, and a concept for parallelizing consecutive multi-cycle simulations.

In order to make the cycle-resolved reference data of the transient engine scenario available for the 3D-CFD simulation, an averaging methodology was introduced that allows to synchronize several realizations of a recorded engine transient at the test bench using a reference variable (the engine speed) and to extract a sequence of phase-synchronized engine cycles. The result is a set of consecutive, ensemble-averaged and crank angle resolved engine cycles along the transient scenario, including fixed assigned control parameters and boundary conditions.

To provide extended boundary conditions, including intake mass flow and exhaust pressure, the 1D gas exchange analysis methodology introduced in Chapter 4.1.2 was modified to include the consecutive progression of multiple cycles throughout the scenario. Furthermore, an available model for estimating averaged wall temperatures was utilized and included in the transient methodology. The resulting crank angle resolved intake mass flow and exhaust pressure boundary conditions, as well as cycle-averaged wall temperatures individually for each cycle of the engine transient, serve as boundary conditions for the 3D-CFD.

In order to reduce the long computation time required to run large consecutive multi-cycle simulations, a method of parallelizing the cycle sequence was used. It utilizes multiple threads and reinitializations based on 1D gas exchange analyses and additional transient initialization cycles. Depending on the thread partitioning, this strategy can significantly reduce the overall computation time of a complete transient engine scenario, albeit higher computational resources are required.

With the datasets of ensemble-averaged control parameters for each cycle along the engine transient, accompanying crank angle resolved boundary conditions from 1D gas exchange calculations, and a methodology for time cost savings, all the necessary modules are available for the transfer of a test bench characterized transient engine scenario in 3D-CFD. The practical application of the presented methodology is demonstrated in the following Chapter 6 using a realistic emission-critical transient scenario for the analysis of particulate emissions.

6. Application: Investigation of RDE Relevant Transient Engine Event

6.1. RDE Relevant Transient Engine Event

To identify an emission-critical transient driving scenario, the Institute for Combustion Engines (VKM) at TU Darmstadt analyzed various RDE driving scenarios with regard to particulate emissions and transferred them to the highly dynamic engine test bench. The scenario “gear change under acceleration” proved to be particularly promising. Therefore, the scenario was specially adapted for transfer to the 3D-CFD simulation. The following section explains a characterization of the scenario and required adaptions in more detail.

6.1.1. Characterization

The full-metal series engine investigated in this work (described in Chapter 3.2) has a Valvetronic system for fully variable adjustment of the valve lift and valve timing. While running through the transient engine scenario, this allows the engine control unit (ECU) to select optimal settings to reduce pressure losses, especially in the part-load range [11].

For the numerical 3D-CFD simulation, this means a large number of possible combinations of piston and valve positions along the transient engine scenario, resulting in almost arbitrary geometrical configurations of the investigated domain. Therefore, the investigated scenario was reproduced with constant valve timing and a fixed intake valve lift curve. This allows the numerical investigation of the entire engine scenario with a fixed set of key grids for all engine cycles. The following fixed valve parameters were derived from the analysis of the full transient scenario: A timing of 105 °CA bTDC was chosen for the exhaust valve, and 75 °CA aTDC for the intake valve. For the selection of the maximum valve lift, care was taken to avoid part-load specific measures to increase charge motion such as *phasing* and *masking*. An inlet valve lift of 8 mm was selected. A further discussion of both the scenario with variable and fixed valve timing is given in Appendix A.

Figure 6.1 (top) shows the transient scenario averaged from 8 realizations, represented by the indicated mean effective pressure ($imep$) and the engine speed. Shaded in grey is the standard

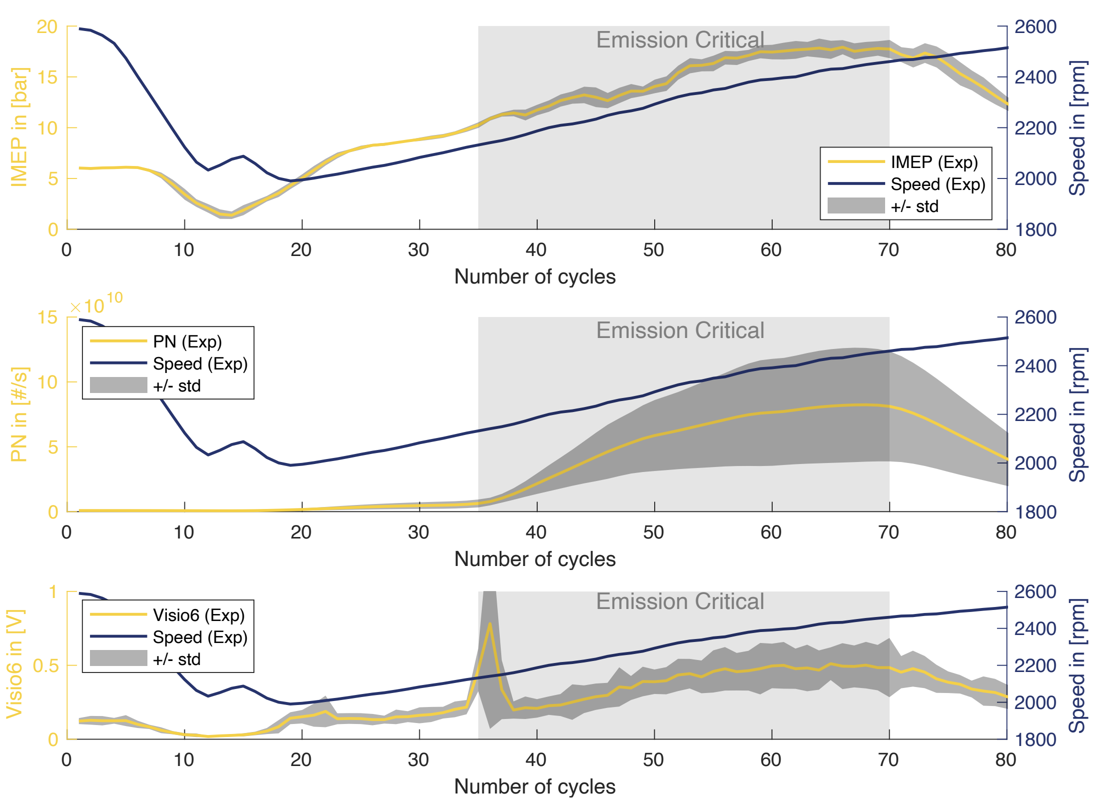

Figure 6.1.: Emission-critical region of RDE relevant transient engine scenario. The top section depicts the increasing engine load along the transient. The mid-section depicts the resulting soot particle emissions, represented by the particle number (PN), measured by the particle counter. The bottom section depicts the corresponding signal of the Visiolution optical spark plug sensor in exhaust valve direction.

deviation of the measurements. The scenario starts from a steady state operating point at 2590 rpm and an $imep$ of 6 bar. Due to the gear change, there is initially a dip in both variables before the acceleration process begins at about cycle 20. As a result, the engine accelerates from part-load to the full-load range. Figure 6.1 (center) depicts the measured raw particle count before the catalytic converter. It can be seen that notable particulate emissions do not occur until cycle 35 of the transient scenario is reached. The curve follows the increase in the engine load up to cycle 70 before a drop sets in. It can be seen from the standard deviation that the raw particle number (PN) can vary strongly between the realizations. However, the initial start of the increase in particle number can be reproduced well across all realizations. The range from cycle 35 to cycle 70 will be referred to in the following as the emission-critical cycle range due to this sharp increase in the observed number of particles.

In addition, the combustion characteristics for cylinder 4 were analyzed over the scenario using a Visiolution optical spark plug sensor. Particularly outstanding is sensor signal 6 shown in Figure 6.1 (bottom). The sensor, which points in the exhaust valve direction, not only reflects the characteristic load profile of the cylinder but also shows a particularly prominent signal around cycle 37. A close look at the experimental results of the cycle indicates that the signal spike is related to a detected knock event.

In addition to these three characteristic variables, further control parameters of the ECU are available for interpreting the transient scenario and transferring it to the virtual engine model. Figure 6.2 depicts a selection of available parameters and their course along the scenario.

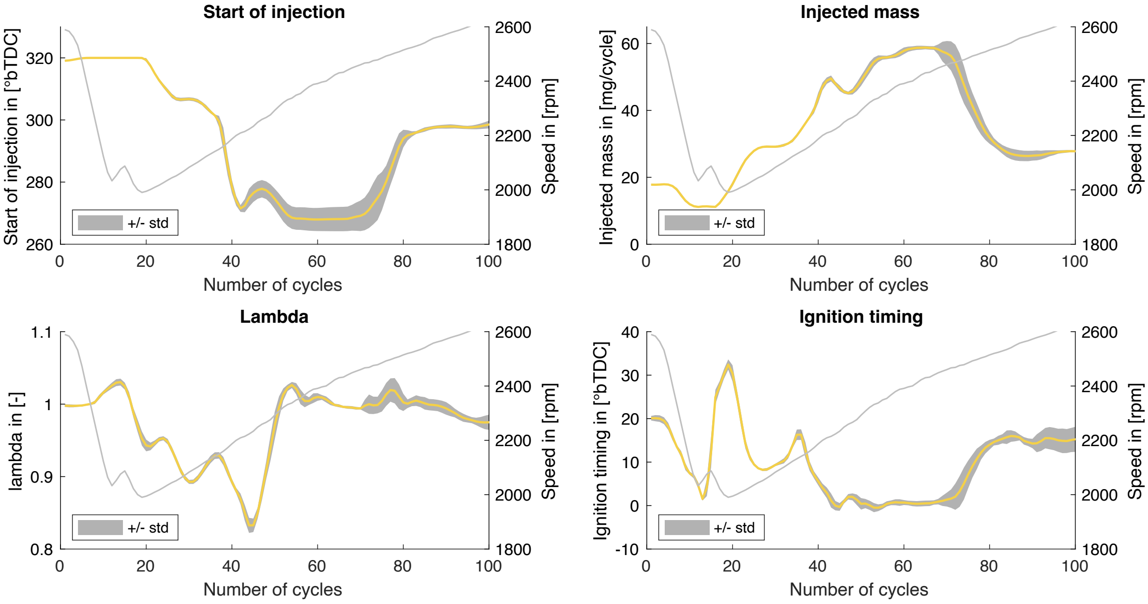

Figure 6.2.: Selected engine control parameters over the transient engine scenario. The grey area highlights the standard deviation.

It can be observed how the start of injection (SOI) is shifted towards later crank angles, particularly in the region of highest engine loads. Furthermore, the amount of fuel injected increases with increasing engine load. The drop in the detected air-fuel equivalence ratio (lambda) below the stoichiometric ratio in the early part of the acceleration phase indicates a temporary lack of air in the combustion chamber. A comparison with the scenario at fully variable valve timing suggests that this is a consequence of the fixed timing and valve lift used in this study. The ignition timing shows the temporary shift towards early crank angles. This coincides with the detection of knock at cycle 37. In the later course, a constant ignition timing of about 0 °CA bTDC is established. The connection between individual parameters and the observed emissions is discussed further in Chapter 6.2 based on the transient 3D-CFD results.

It is worth noting that under the selected conditions, the entire scenario is carried out in a single fuel injection mode. For selected experimental realizations, a change to a multi-injection mode for high loads was observed. A detailed comparison of both modes is depicted in Figure 6.3. Plotted are the start and the duration of each fuel injection in the form of a bar graph for each engine cycle along the transient scenario. Starting from cycle 45, the mode changed and the initial first injection is shifted backward towards an SOI of 300 °CA bTDC. Two additional injections are carried out at 200° and 90 °CA bTDC with subsequently decreasing injected fuel mass. The implementation and further evaluation of the scenario with multiple injections is discussed in Chapter 6.3.

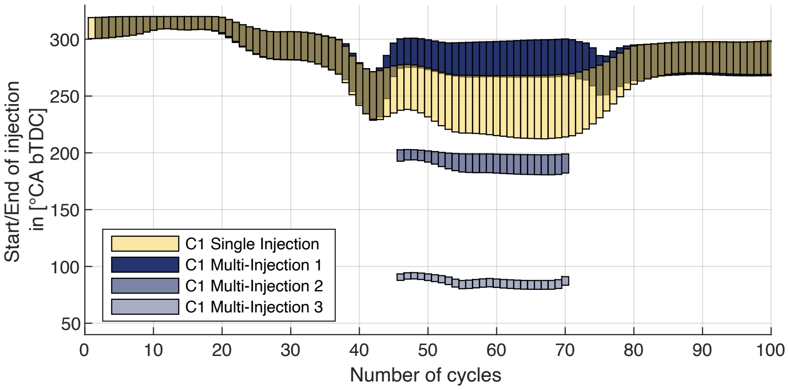

Figure 6.3.: Comparison of a single-injection and a multi-injection strategy at the RDE relevant transient operating point.

6.1.2. Transfer into the Virtual Engine Framework

1D gas exchange analysis

To provide further boundary conditions, the experimentally provided high- and low-pressure indicated data were used to perform a gas exchange analysis of the scenario using the methodology presented in section 5.1.2. The synchronized and averaged data sets from 8 experimental realizations of the transient scenario presented in section 6.1.1 were used as input data.

In Figure 6.4, the indicated mean effective pressure ($imep$) obtained by the simulation for the scenario is compared with the experimentally determined mean pressure. It can be seen that there is good agreement of the $imep$ over the entire transient scenario. The largest deviation occurs in the range of the gear change, with a deviation of approximately 20%.

The wall temperatures of the transients determined for this transient load profile are shown in Figure 6.5. As already observed for the generic transient load ramp presented in Chapter 5.1.2, the temperatures vary only by a few degrees over the course of the scenario. In the early phase, the curve follows the changing load profile very well. In the high load range, the system reacts

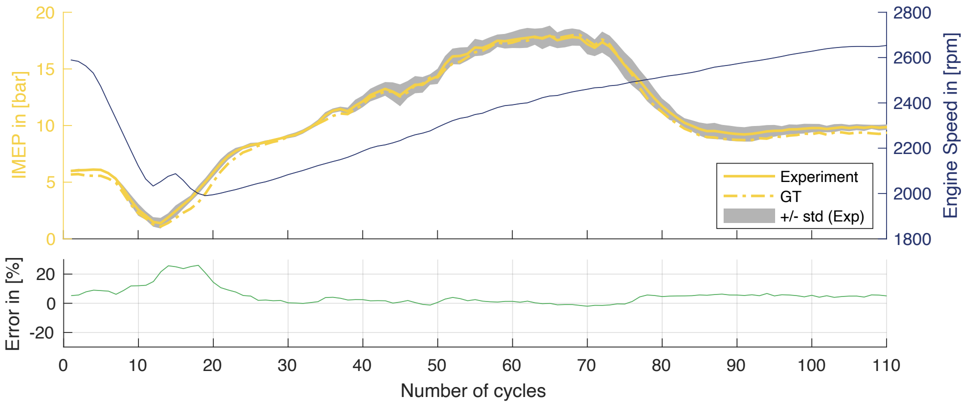

Figure 6.4.: 1D gas exchange analysis of the RDE relevant transient engine scenario. Depicted is the indicated mean effective pressure ($imep$) and the relative error between 1D analysis and experiment (in green).

more slowly. Despite a drop in load, there is a sustained rise in temperatures at the cylinder head and piston. Since no experimental data are available on the present wall temperatures, the temperatures shown here were used for all numerical investigations of the transient scenario in this work, unless otherwise stated.

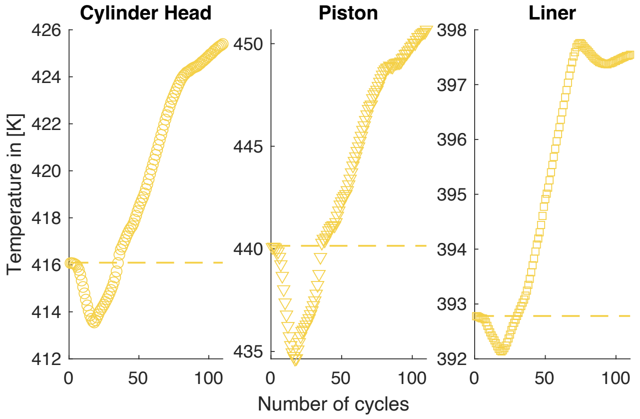

Figure 6.5.: Wall temperatures at the cylinder head, piston and cylinder liner surface from 1D gas exchange calculation of the RDE relevant transient engine scenario.

3D-CFD Model

The model of cylinder 4 used for the 3D-CFD analysis of the transient engine scenario is substantially based on the modeling presented in Chapter 4.1 for the analysis of particulate emissions. However, in contrast to the simulation of the single-cylinder research engine, the discretization of the series engine analyzed in this chapter abandons the assumption of symmetry due to the curved intake manifold and the entire cylinder 4 is discretized using a hybrid tetrahedron-prism mesh. A total of 66 key grids are used for one engine cycle. The total number of mesh nodes used during a cycle varies between 1 and 3 million nodes depending on the current crank angle. An overview of the number of mesh nodes used along an engine cycle is shown in Figure 6.6 (left). The local mesh refinement at the valve plane is shown in Figure 6.6 (right) for a crank angle of 386 °CA bTDC as an example. Keeping valve timing constant allows the entire transient engine scenario to be covered with one set of key grids, significantly reducing the computational effort.

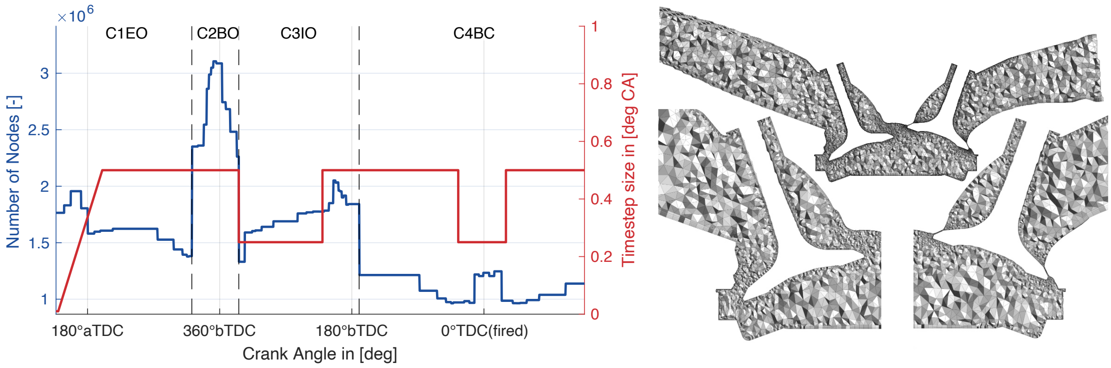

Figure 6.6.: Left: Number of mesh nodes along an engine cycle. Right: Sectional view of the mesh at valve plane for 386 °CA bTDC.

An Euler-Lagrange modeling approach was chosen to model the direct fuel injection. The necessary characterization of the injector mounted in the engine was kindly provided by BMW AG and is based on a fixed particle size distribution in the engine's high load range. Unfortunately, a load-dependent characterization of the mounted injector was not possible within the scope of this work, which is why the identical particle size distribution was assumed over the entire transient.

Individual boundary conditions of each cycle, such as engine speed, injection timing, ignition timing, etc., are set according to Chapter 5.1.1. Mass flow inlet and pressure outlet boundary conditions, as well as wall temperatures, are taken from the supplementary transient gas exchange analysis presented in the previous section.

Simulated regions of the transient scenario

With a total duration of approx. 80 cycles, the RDE relevant transient engine scenario represents a challenge for any 3D-CFD simulation. A consecutive simulation of all cycles results in a time expenditure of approx. 3.7 months. However, the experimental investigations of the transient engine scenario show that the highest emission potential is primarily at the end of the transient from about cycle 35 onward. Therefore, the thread-based simulation approach presented in Chapter 5.1.3 was first tested starting from the steady-state operating point at the beginning of the transient. Based on the results, the emission-critical region was calculated separately starting from cycle 33 with corresponding initialization cycles. The total of 31 simulated engine cycles of the emission-critical region was calculated in two overlapping threads. Thread 1 covers the first part of the transient from cycle 31 to cycle 43 and Thread 2 the last part from cycle 44 to cycle 62. Two cycles overlapping with Thread 1 were used for the initialization of the second thread.

6.2. CFD-Based Investigation of Emission Sources

6.2.1. Model Evaluation based on Experimental Data

Figure 6.7 shows the calculated indicated mean effective pressures ($imep$) of all calculated cycles and compares them with the experimental measurements and the data from the previously calculated 1D gas exchange analysis. The sequence of simulated cycles can reproduce the measured transient very well. The best agreement can be obtained in the range of highest peak pressures from cycle 31 to cycle 38. For this range, the model parameters of the turbulent burning velocity model used were adjusted and calibrated for the study. With increasing distance from the calibration point, there is a slight overestimation of the calculated $imep$.

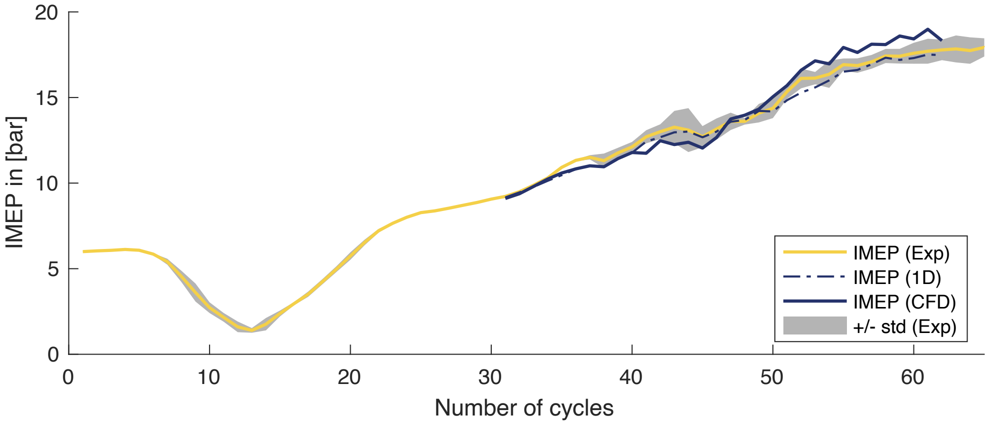

Figure 6.7.: Comparison of indicated mean effective pressure ($imep$) of the experiment, 1D-simulation and the 3D-CFD simulation.

The decisive factor for the investigations carried out in this work is the resulting soot emissions. The moment-based soot model used provides information on the locally present soot volume fraction/integrated soot volume and the particle number density. Figure 6.8 gives an overview of all named quantities at the time the exhaust valves are opened (EVO).

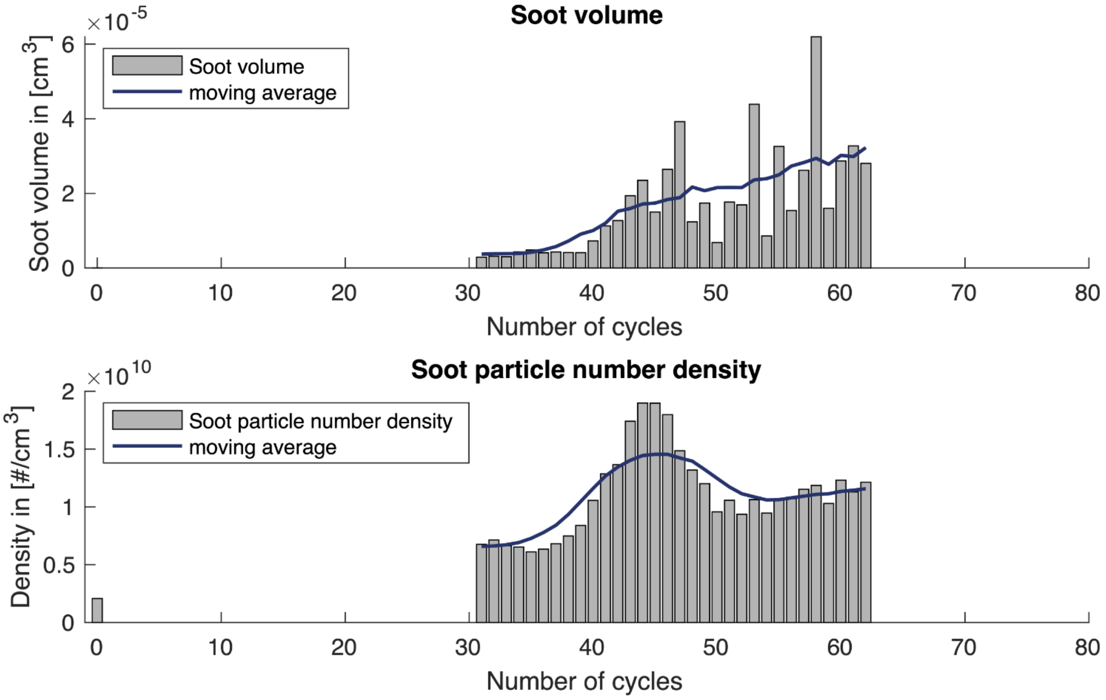

Figure 6.8.: Integrated soot volume and soot particle number density in the engine domain for all calculated engine cycles along the engine transient.

The 3D-CFD simulation shows a significantly increased amount of soot in the entire emission-critical region compared to the steady-state operating point at the start of the scenario (cycle 0). The detected particulate emissions remain at similar levels during the first 9 cycles of the emission-critical region. This range includes the cycles with the highest peak pressures and the cycle range of potential knock. Beginning with cycle 40, an increase in the calculated soot volume can be observed. While the general trend of the soot volume represented by the moving average increases over the course of the transient scenario, individual cycles show large deviations from each other. The resulting particle number density shares the general trend toward higher numbers. However, a temporary increase in the calculated soot particles in the period from cycle 40 to cycle 50 is striking. This section coincides with the initial increase in the soot particle volume.

For a more detailed analysis of the particle size distribution inside the engine cylinder, a mean particle diameter was determined for each mesh cell of the domain based on the local particle number density and soot volume. Figure 6.9 shows the calculated mean particle diameters for all transient engine cycles at the time of exhaust valve opening (EVO). In a large part of the mesh cells, mean particle diameters around 10 nm occur. This is particularly evident in cycle 45.

The cycle with the highest total particle number density exhibits this in particular with very small particle diameters. It can be observed that only with further load increase towards later cycles, a significantly larger number of mesh cells with larger mean particle diameters appear.

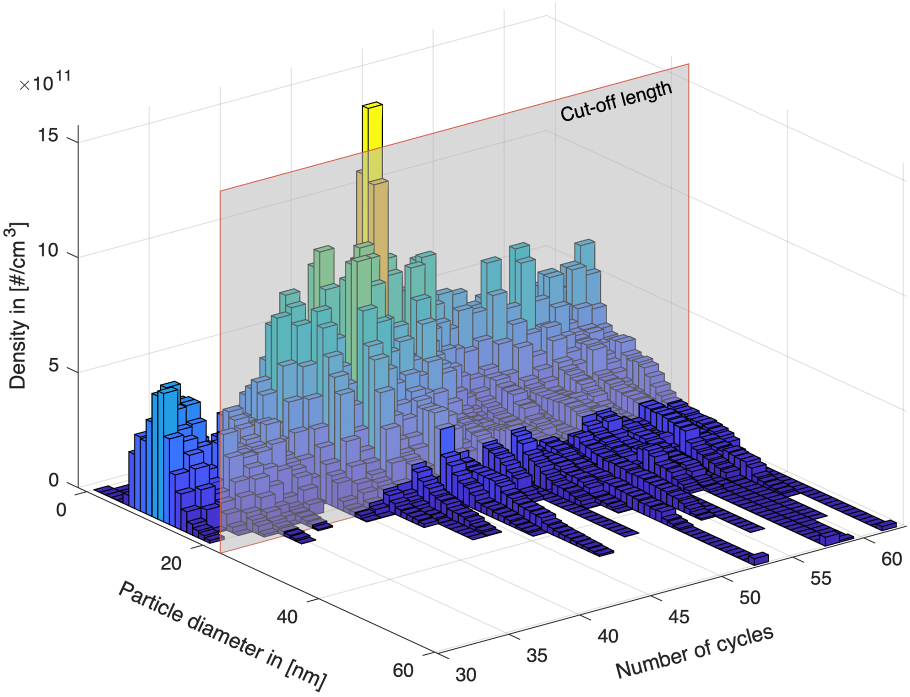

Figure 6.9.: Histogram of the mean soot particle diameter in the engine domain at EVO for all simulated engine cycles. The highlighted plane indicates the cut-off length at a particle diameter of 23 nm of the experimental measurement.

Since experimentally measured particle numbers are only taken into account by the particle counter above a defined particle size, it makes sense to also introduce a corresponding cut-off length for a comparison of the numerically calculated data.
For optical visualization, a characteristic cut-off length of 23 nm is highlighted in Figure 6.9. Using only mesh cells with mean particle diameters above this threshold in the calculation of the integral soot volume and particle number density results in a significantly different profile. In Figure 6.10, both are plotted comparatively for the full particle size distribution and the limited particle size distribution in the engine domain.
Consideration of the cut-off length is particularly noticeable for the soot particle volume in the first half of the simulated transient engine cycles. In this range, a large part of the soot volume is no longer included in the evaluation, since it is composed of particles with a mean particle diameter below 23 nm. A reduction of the particle volume is also observable in the second half of the transient. Nevertheless, a significant fraction remains. The cut-off length

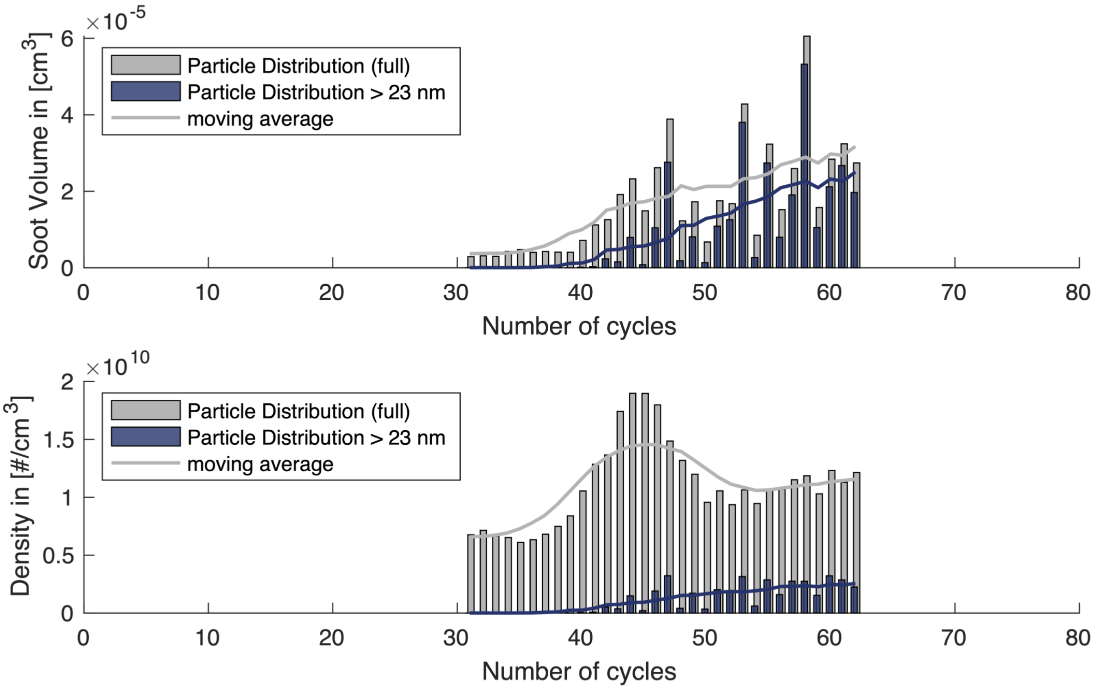

Figure 6.10.: Integrated soot volume and soot particle number density corrected by the cut-off length of 23 nm.

is also clearly noticeable in the particle number density since a large part of the combustion chamber domain exhibits only small mean particle diameters. Over the course of the simulated transient, however, there is a tendency for the number of particles to increase, with particles larger than 23 nm appearing more and more frequently in the domain. A temporary increase in the calculated particle number density, as observed when considering the overall particle size distribution, no longer exists. The observed high particle numbers are thus essentially due to zones with a very high particle density but only very low mean particle diameter.

For evaluation purposes, the particle number density reduced by the cut-off length can be qualitatively compared with the experimentally determined particle number in the exhaust gas flow before the catalytic converter. Figure 6.11 shows the particle number per cycle throughout the transient engine scenario, both experimentally determined and numerically calculated based on the previously introduced cut-off length. The standard deviation calculated from eight experimental realizations of the engine scenario is shaded in grey. It should be noted that for the comparison, the numerically calculated number density was scaled by a factor of $1\mathrm{e}{-3}$. Both results show a good qualitative agreement. The first notable increase in particle number in both curves occurs around cycle 40. The moving average of the simulation results can reproduce the experimentally observed increase well. However, a large fluctuation from cycle to cycle can still be observed when examining individual results of simulated engine cycles.

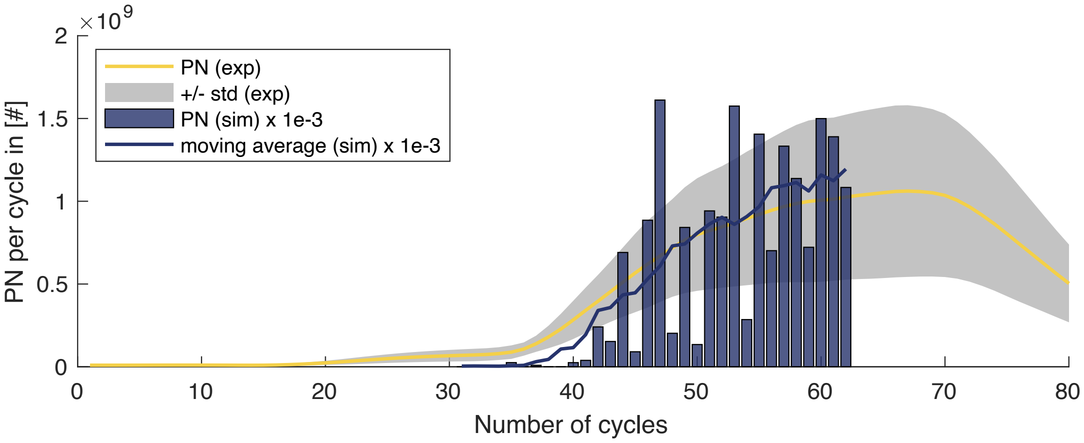

Figure 6.11.: Comparison of experimentally measured number of soot particles per engine cycle and cylinder with corrected soot particle numbers of the numerical simulation. Note that the numerical results are scaled by the factor of 1e-3 for comparison.

In order to obtain a more detailed picture of the ongoing processes and causes of the increase in particulate emissions along the transient engine scenario, a detailed cause-and-effect chain analysis of the scenario is performed in the following section.

6.2.2. Cause-and-Effect-Chain Analysis

Based on both the experimental characterization of the scenario presented in Section 6.1.1 and the simulative insights gained in this work as presented in Section 6.2.1, the emission-critical region can be divided into three characteristic regions.

Region 1 is characterized by an experimentally detected knock event and a corresponding signal from the optical spark plug sensor of high intensity. The signal, which is reproducible over several realizations, occurs in the region around cycle 36. Although the 3D-CFD simulation in the configuration used in this work cannot represent the influence of engine knock, a look at the conditions inside the engine cylinder allows further interpretation of the experimental observations.

Region 2 denotes the initial sharp increase in the measured soot particle emissions from cycle 38 to cycle 48. Since this is associated with a series of adjustments to the engine control parameters that took place after the knock event, this region is referred to in the following as the "knock aftermath". The transient engine simulation carried out in this work shows particularly high particle number densities in this range at comparatively low total soot volumes. A look into an individual engine cycle allows us to identify the cause for this observation.

Region 3 indicates the region with the highest load of the investigated engine scenario starting from cycle 49. On average, the highest particulate emissions occur in this range, both experimentally and simulatively. Noticeable in this region are fluctuations in the particulate emissions between individual engine cycles. A more detailed analysis of individual engine cycles allows the causes for these observations to be identified.

Figure 6.12 describes all three regions defined for the detailed analysis relative to the measured particle emissions. In the following, the observations and obtained findings for the respective regions are discussed in detail.

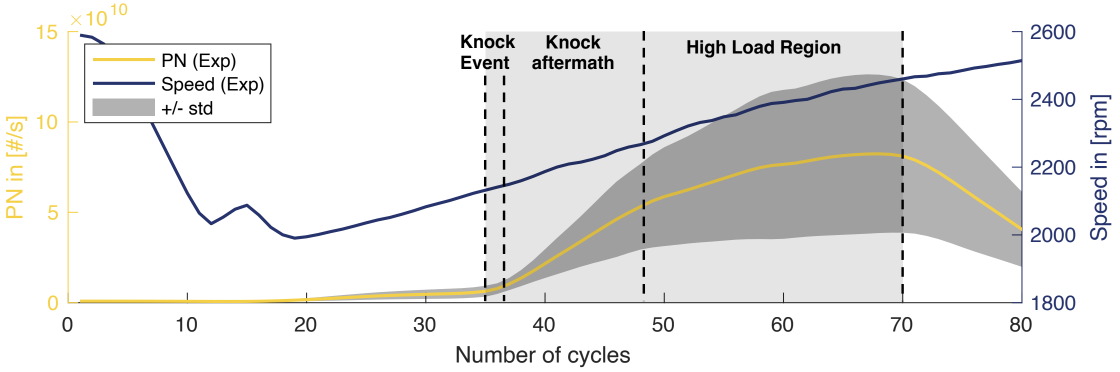

Figure 6.12.: Particle (PN) emissions along the transients are divided into individual affection areas for investigation within the framework of a cause-and-effect chain analysis.

Region 1 – Knock Event

The analysis of the knocking event and its influence on the particle emission is not easily feasible by a 3D-CFD simulation without special modeling. Nevertheless, the influence of experimentally determined boundary conditions at the time of the event can be represented and investigated.

To evaluate the influence of possible component wetting/coking from the experimental observations, the accompanying 3D-CFD simulations first considered the resulting wall film at cycle 36. Figure 6.13 (right) shows the injection of fuel into the combustion chamber and its interaction with the walls for two selected timesteps. At the time of injection (SOI=300 °CA bTDC), the piston is near the top dead center and is in a downward motion. The spray cones strike the piston surface (below the injector) head-on as well as the cylinder wall and the piston opposite the injector, as depicted for 287 °CA bTDC. From the observations, it cannot be ruled out that the spray cone also acts on the piston crevice. Since the piston crevice is not taken into account in the modeling, corresponding influences cannot be evaluated. The different wall temperatures of the components lead to different interaction behavior. A relatively warm piston temperature of 440 K prevents the formation of a wall film on the piston surface. The cylinder wall experiences better cooling at 393 K, and wetting of the surface occurs, as depicted for 254 °CA bTDC. The fuel mass deposited on the wall relative to the total fuel mass is shown in Figure 6.13 (right). Over the entire cycle, a maximum of 0.6% of the fuel mass is deposited on the wall. Most of the wall film forms on the cylinder liner, while the piston surface shows only minor wetting. Overall, the resulting wall film evaporates rapidly and has already completely disappeared at 225 °CA bTDC.

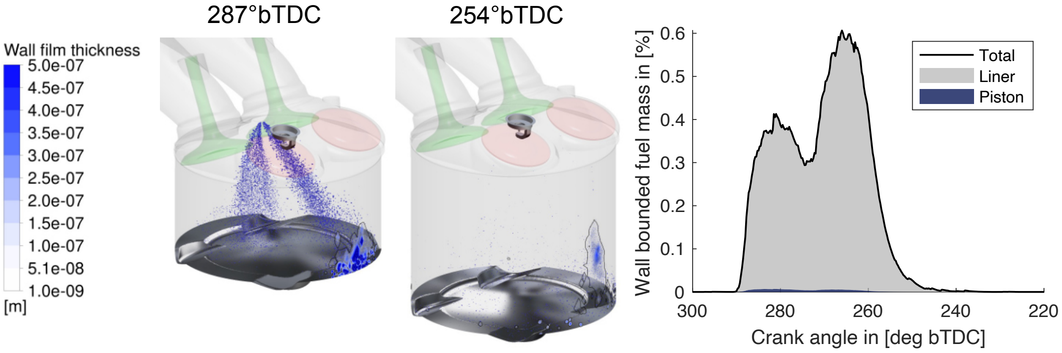

Figure 6.13.: Wall film formation at cycle 36 of the engine transient. Left: Visualization of the spray cone and wall film as Lagrange parcel in the domain and film thickness at the piston and cylinder liner surface. Right: Integrated fuel mass at piston and cylinder liner surface. The colors indicate the distribution of the wall film mass between the cylinder liner (grey) and the piston (blue).

Since wall temperature boundary conditions in 3D-CFD engine simulation are typically subject to large uncertainty, the wall temperatures at the piston and cylinder walls were varied to estimate the sensitivity of the results to the temperatures used in a further step. The wall-bound fuel mass for the three variants A, B and C is shown in Figure 6.14 (left). The corresponding wall temperatures can be obtained from Figure 6.14 (right). Case B, with the oil/coolant temperatures, represents the lower limit for the realistic wall temperature range. Case C is below this limit, but assumes equal wall temperatures for the piston and cylinder wall. By lowering the wall temperature, the maximum bound fuel mass can be increased by up to 2%. All variants lead to complete vaporization of the fuel mass by the time of ignition.

In order to estimate the influence of non-representative low-volatile components of the real fuel, the evaporation properties of the surrogate fuel were modified in a further calculation. For the modified calculation (mod), the vapor pressure and the material properties of the liquid phase of the surrogate fuel component iso-octane were replaced by those of n-decane as a representative low-volatility component. With this adjustment, a wall-bound fuel fraction of up to 6% can be forced and $\sim$3% maintained until the ignition time.

Figure 6.15 summarizes the resulting changes in soot volume for the different wall temperature configurations. A comparison indicates that there is no significant increase for any of the

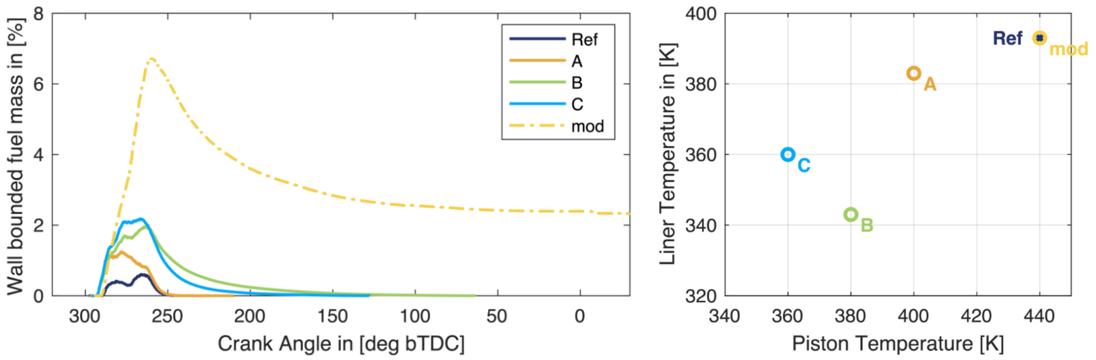

Figure 6.14.: Wall bounded fuel mass under the assumption of 5 different wall temperatures/ fuel properties for engine cycle 36 (left). The different wall temperatures for each configuration are given in the matrix on the right. The label *mod* indicates a configuration with modified fuel properties.

configurations shown. However, it should be noted that the model currently used can only represent gas phase-related soot sources. Possible effects due to a wall film persisting up to the ignition time and beyond, such as pool fire and pyrolysis, cannot be represented by the simulation model used.

The investigations carried out confirm the assumption of temporary wall wetting and possible coking in the area of the piston-cylinder transition and the piston crevice opposite the injector. Although the wall film evaporates quickly in the simulation model, additional low-volatile components in the fuel have a retarding effect that can lead to a long-lasting film, especially on the cylinder wall. The responsible operating conditions for this occur over a period of several cycles. Since the increased deflection in the optical spark plug sensor signal 6 occurs exclusively during the knock event, a possible diffusion flame can be ruled out and instead an interaction with dissolving deposits is likely.

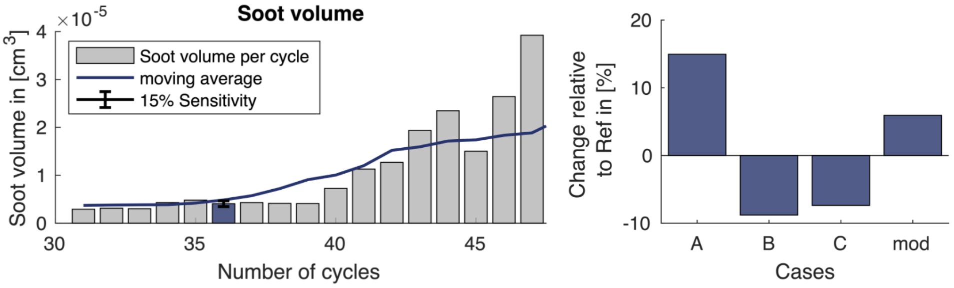

Figure 6.15.: Resulting integrated soot volumes at different wall temperatures for cycle 36. Left: The original cycle 36 in blue in correlation to its neighboring cycles. Right: The impact of different wall temperature configurations/fuel properties relative to the original configuration. The case labels correspond to Figure 6.14.

Region 2 – Knock Aftermath

As a result of the knock event, various adjustments of the engine control parameters and thus of the boundary conditions of the system can be observed. Starting from cycle 37, there are significant changes in ignition timing, injection timing and measured actual lambda (c.f. Figure 6.2). The increasing load requires an increased charge of the cylinder and thus the injected fuel mass increases. The drop in the lambda value indicates that the fresh air supply cannot keep up with the increased demand. At the same time, there is a delay in the injection timing with effects on mixing and a shift of the ignition timing towards the top dead center.

The soot statistics of the transient scenario presented in Figure 6.8 not only indicate an increase in total particle volume but also show significantly higher soot particle number densities in the affected cycles. This increase, as highlighted in Figure 6.9, is mainly attributed to an increase in smaller mean particle diameters due to excess fuel.

Figure 6.16 shows the local particulate emissions of cycle 44 of the engine transient as an example for this region. It is clear how after ignition at 0.2 °CA aTDC there is a uniform increase in soot particle volume behind the flame front. This increase is a consequence of the globally fuel-rich mixture in the combustion chamber. As combustion progresses, the effects of local inhomogeneity also play a role. Especially in the area of the cylinder wall below the intake and exhaust valves, there is a further increase in emissions. These effects play an even more important role with increasing load along the engine transient.

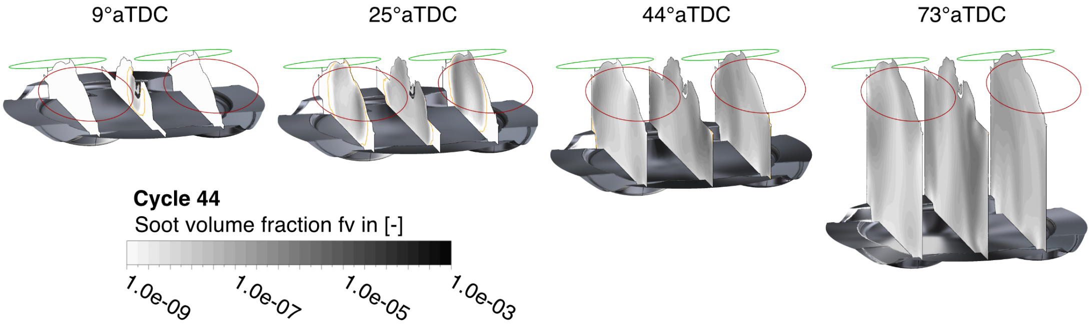

Figure 6.16.: Local distribution of the soot volume fraction f_v for cycle 44 of the transient at three cut-planes along the cycle. The orange line highlights the flame front represented by the flame progress variable at 0.02.

The observations emphasize that the particulate emissions determined can by no means be clearly attributed to a single isolated cause. Instead, the combination of various overlapping effects plays a role. Depending on the existing boundary conditions, these can have a larger or smaller influence on the resulting particulate emissions of the cycle.

Region 3 – High Load Region

After the region of fuel-rich combustion, the experimentally determined emission curve shows a further increase in particulate emissions. The numerical investigations can confirm this trend. However, the increase is accompanied by strong fluctuations in the particulate emissions between the cycles. Figure 6.17 shows the local equivalence ratio near the top dead center at 6.5 °CA aTDC and the locally occurring particle volume fraction at time 73 °CA aTDC for three representative cycles of the range, cycle 58, 59 and 60. The three cycles differ only slightly in their boundary conditions but exhibit different stratification. The local, very fuel-rich areas lead to increased soot formation in the course of combustion. The area of the squish gap opposite the injector is particularly noticeable in all three cycles. The increased fuel content in this area appears to be decisive for the overall emissions.

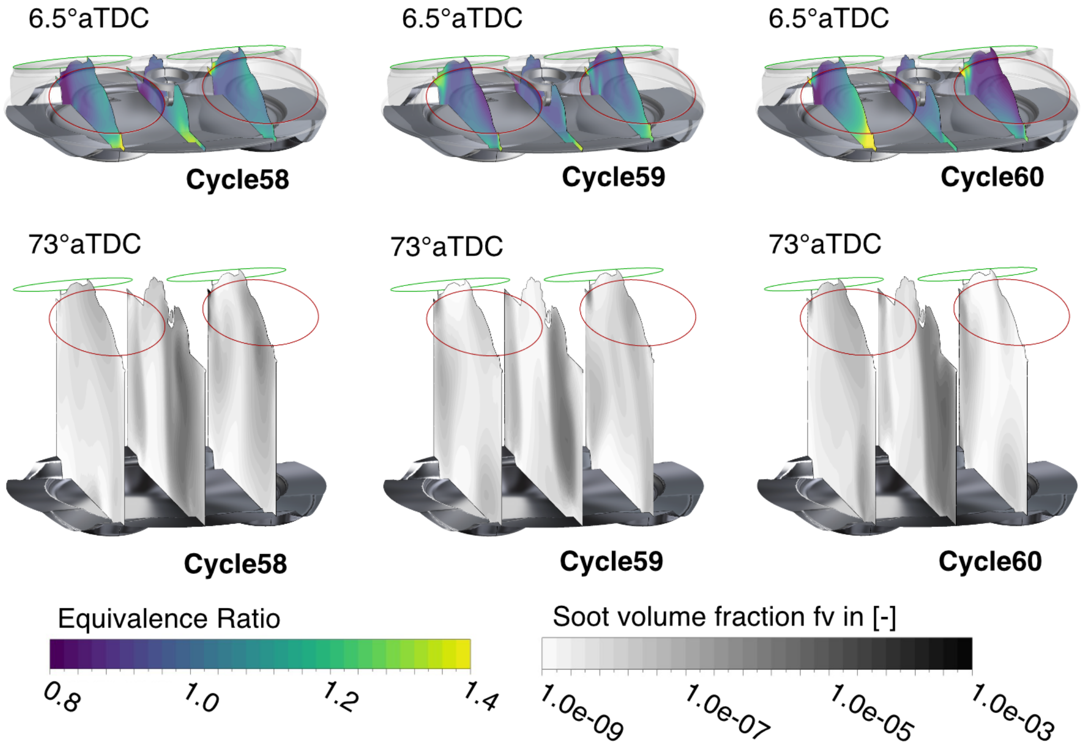

Figure 6.17.: Local mixture distribution at 6.5 °CA aTDC and soot volume fraction f_v at 73 °CA aTDC for three consecutive cycles starting from cycle 58 of the engine transient.

The volume-based uniformity index is introduced as a parameter for quantifying mixture homogeneity. For the calculation of the index, a variety of calculation rules can be found in the literature. In this work, the following rule was used:

$$UI_\phi = 1 - \sqrt{\frac{1}{V_{tot}} \frac{\int (\phi - \overline{\phi})^2 dV}{\overline{\phi}}} \,. \tag{6.1}$$

In this equation, V_{tot} denotes the total cylinder volume, ϕ the local and $\overline{\phi}$ the volume-averaged equivalence ratio over the entire cylinder volume. Figure 6.18 (left) depicts the uniformity index for all calculated cycles at the respective time of ignition. The averaged progression of the index, shown in yellow, illustrates how the homogeneity decreases at the beginning of the investigated range. From cycle 40 on, this decrease stagnates; from this point on, the homogeneity varies widely from cycle to cycle. The decrease in uniformity correlates with the observed shift in injection timing. The relationship between the two quantities is shown in Figure 6.18 (right). As expected, there is a clear trend toward better uniformity at early injection timings. In the range of later injection (265 °CA bTDC – 280 °CA bTDC) the same strong variations of the uniformity index can be observed.

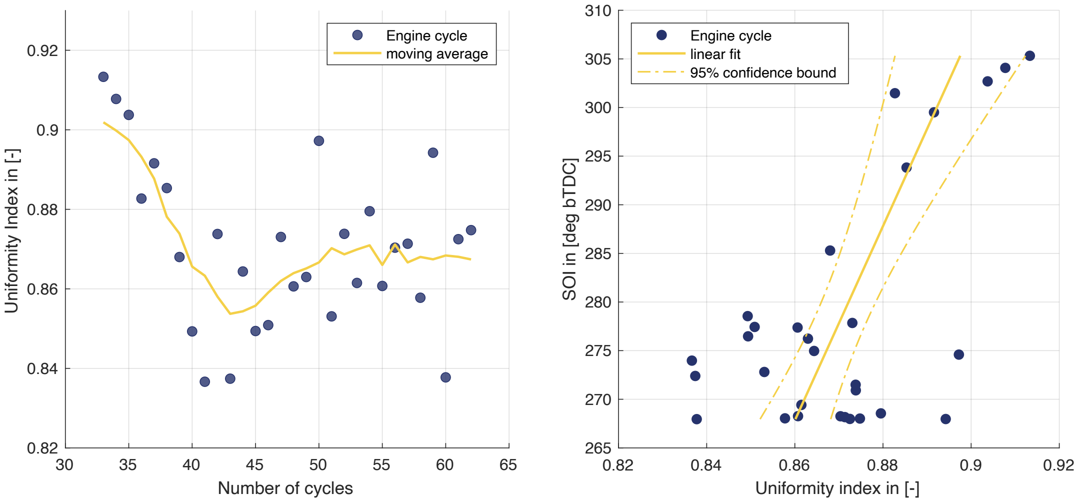

Figure 6.18.: Left: Uniformity index for each cycle along the engine transient. Right: Correlation between the start of fuel injection (SOI) and the uniformity index.

A detailed look at the underlying mixture field provides further insight into the causes of the strong fluctuations. In Figure 6.19 the local equivalence ratio for cycle 60 of the emission-critical engine transient is illustrated over the compression phase. The arrows marked in red indicate the direction of movement of the fuel-rich mixture through the combustion chamber. It can be seen that at a given injection point of 265 °CA bTDC, the very fuel-rich mixture moves through the combustion chamber following the tumble flow and continues to mix. When the piston reaches the top dead center, a large part of the fuel-rich charge is located in the area of the squish gap below the intake valves. The fuel mass trapped there can vary greatly depending

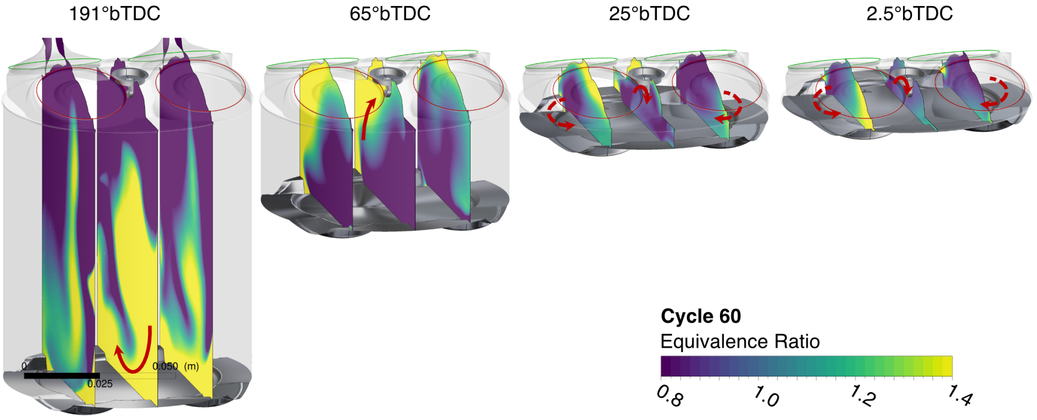

Figure 6.19.: Mixture homogenization process in the high-load region of the engine transient represented by cycle 60. Depicted is the equivalence ratio. The red arrow highlights the movement of the fuel-rich mixture through the domain

on local flow fields. A comparison of the equivalence ratio in the squish gap at 25 °CA aTDC for cycle 59 and cycle 60 of the transient further illustrates this effect. Figure 6.20 shows the respective equivalence ratio on the slice plane through the gap. Despite nearly identical boundary conditions of both cycles, the mixture trapped in the gap differs significantly. The difference is clearly visible in the resulting soot emissions.

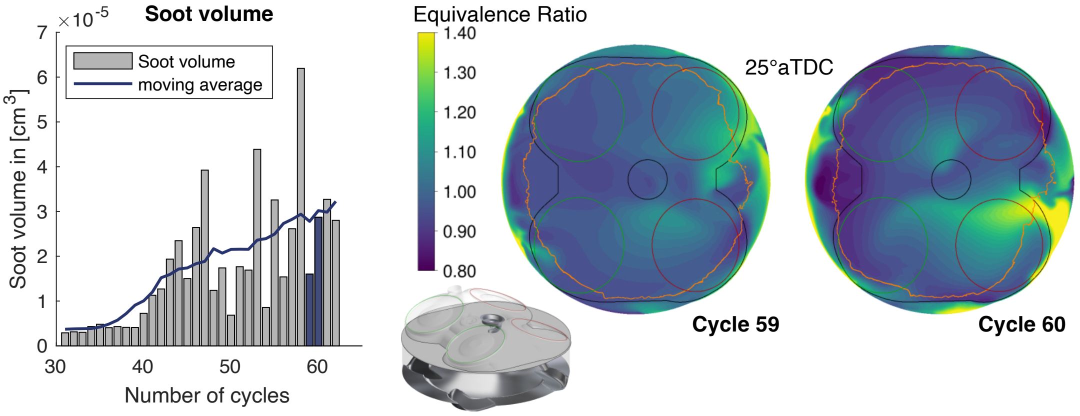

Figure 6.20.: Left: Integrated soot volume for cycles 59 and 60 (highlighted in blue) relative to the complete engine transient. Right: Equivalence ratio at a slice plane in the squish gap of the cylinder for cycles 59 and 60. The orange line highlights the flame front represented by the flame progress variable at 0.02.

The observed high emissions are thus attributable to the inhomogeneities of the fuel-air mixture present in the combustion chamber. In addition to the global inhomogeneity, the local distribution of the inhomogeneities in the combustion chamber is also relevant. This can vary strongly from cycle to cycle along the emission-critical transients.

6.3. Potentials for Emission Reduction

The following two main objectives can be derived from the causes of increased soot particle formation identified in the previous analysis:

- Maintaining an ideal air-fuel ratio throughout the entire transient scenario.
- Reduction of mixture inhomogeneities in the high-load region of the transient scenario.

In the following section, possible measures to achieve these goals are discussed. For this purpose, further analyses of the relevant operating range of the transient are carried out and identified measures are compared with experimental reference measurements.

6.3.1. Preservation of an Ideal Air-Fuel Ratio

The experimentally observed deviations from the ideal air-fuel ratio occur primarily in the early acceleration phase during the steepest load increase of the transient. Comparisons with measurements at fully variable valve timing (compare Appendix A) indicate that this effect is a particular feature of the fixed valve timing configuration used in this study.

In order to evaluate the influence of deviations from the ideal air-fuel ratio, further CFD simulations were performed for a representative cycle of the transient scenario with adjusted injected fuel mass. The studied cycle 44 shows the lowest lambda value of 0.83 in the entire transient. To increase the value to lambda equals 1, the calculated trapped air mass in the reference simulation was used to correct the required injected fuel mass. By adjustment, the fuel mass was reduced from 52.0 mg to 42.7 mg. Figure 6.21 shows the resulting soot volume and particle number density for the adjustment to $\lambda = 1$ (blue) compared to the transient reference case (black).

The resulting soot quantity is significantly reduced by the adjustment carried out. The increase in particle number density observed for the low lambda range in the reference case can also be reduced. The particle number density level approaches the observed values around cycle 35 of the reference transient.

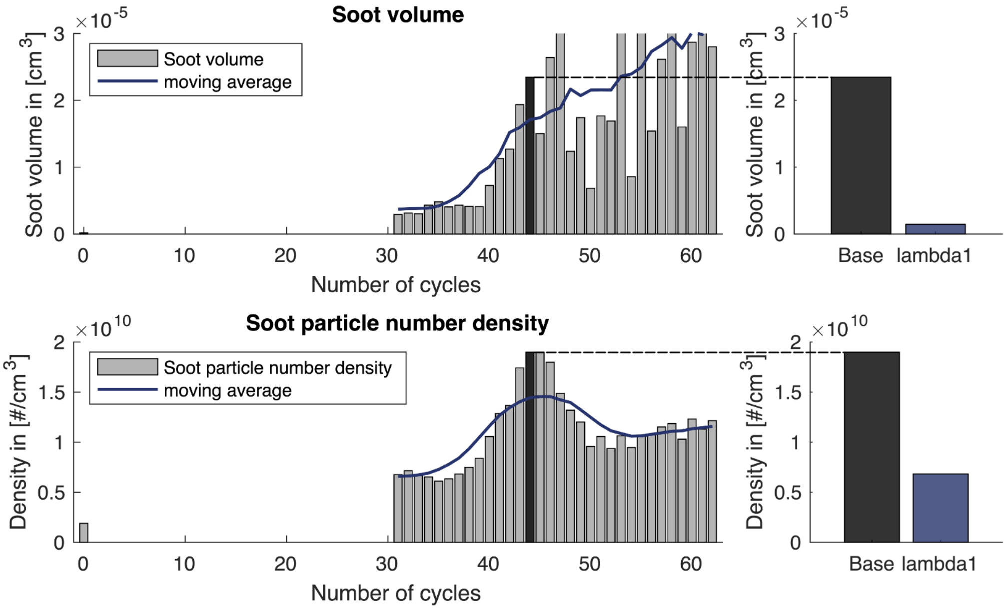

Figure 6.21.: Comparison of resulting total soot volume between cycle 44 with $\lambda = 1$ adjustment (blue) and cycle 44 of reference engine transient (black).

6.3.2. Reduction of Mixture Inhomogeneities

As shown in section 6.2, the observed air-fuel mixture inhomogeneity is essentially attributed to the late fuel injection timing persisting over the entire high-load range. The start of injection, which is rather late in the range from cycle 40 to cycle 70 at 268 °CA bTDC, does not give the mixture sufficient time to homogenize. The result is a locally very high fuel concentration at combustion with associated emissions.

In order to derive possible measures, a comparison was first made between the configuration with fixed valve timing (C1) and variable valve timing (C0). In the course of the transient, both configurations show a shift of the start of injection towards later crank angles with increasing load. However, the C0 configuration switches to a triple injection mode in the region of the highest load and injected mass. This behavior can be seen in the C1 configuration only in selected realizations. Figure 6.3 compares the start and end of fuel injection conditionally averaged as a function of the injection strategy for fixed valve timing (C1). In the low and medium load range, both variants exhibit an almost identical strategy; only in the high load range do the two variants differ. In the range from cycle 50 to cycle 70, for some of the realizations the required fuel mass is introduced into the combustion chamber in three injection processes instead of one, starting with the first injection at 300 °CA bTDC. For this strategy, the first injection occurs earlier than for a single injection. Injections 2 and 3 follow at an injection start of 200 °CA bTDC and 87 °CA bTDC.

To assess the impact of the injection strategy, different strategies were compared based on cycle 60 of the transient engine scenario. The investigation includes the reference operating point with a single injection at SOI=268 °CA bTDC, a triple injection with three injection events starting at SOI=300 °CA bTDC, and an alternative early single injection at SOI=301 °CA bTDC. Figure 6.22 depicts the resulting total soot volume and particle number density of the respective injection strategies at the time of exhaust valve open (EVO) compared to the reference transient scenario (Base).

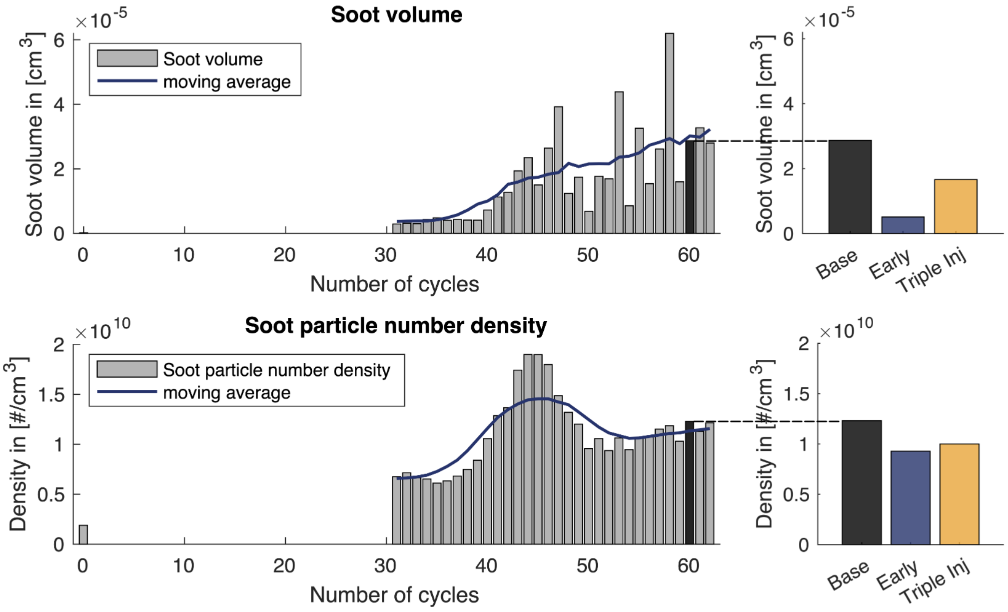

Figure 6.22.: Comparison of resulting total soot volume between cycle 60 of the reference transient scenario, cycle 60 with early single injection at 301 °CA bTDC and cycle 60 with triple injection.

Both early single injection and triple injection are capable of reducing the resulting soot volume in the engine domain, with single injection having significantly higher reduction potential with 82% than triple injection with 42%. The particle number density also decreases for both strategies, albeit to a much lesser extent. An analysis of the corresponding mean particle size distribution in the domain is shown in Figure 6.23. The reason for the significant reduction in soot volume with early injection becomes clear here. The size distribution at early injection is clearly shifted to the left towards smaller particle diameters compared to the baseline operating point. No mean particle diameters of $d_p > 23\,\mathrm{nm}$ are predicted in the domain, instead the number density of smaller mean particle diameters increases significantly. The triple injection strategy can also reduce larger mean particle diameters, although not to the same extent as with the early injection strategy.

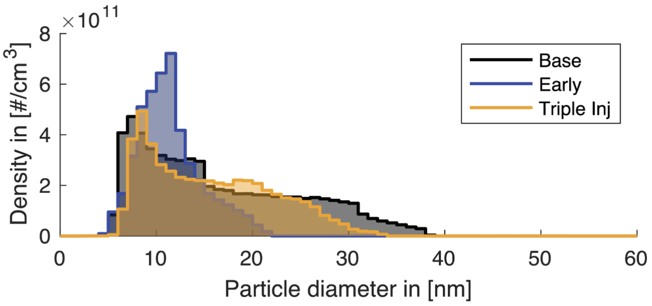

Figure 6.23.: Comparison of the soot particle size distribution in the engine domain for different injection strategies at EVO for cycle 60.

A look at the spatially represented equivalence ratios in the combustion chamber in Figure 6.24 provides further insight into the causes of the reduction. The triple injection is able to significantly reduce the local fuel excess observed in the reference simulation at the squish gap region opposite the injector. Nevertheless, additional emission sources occur in other areas of the combustion

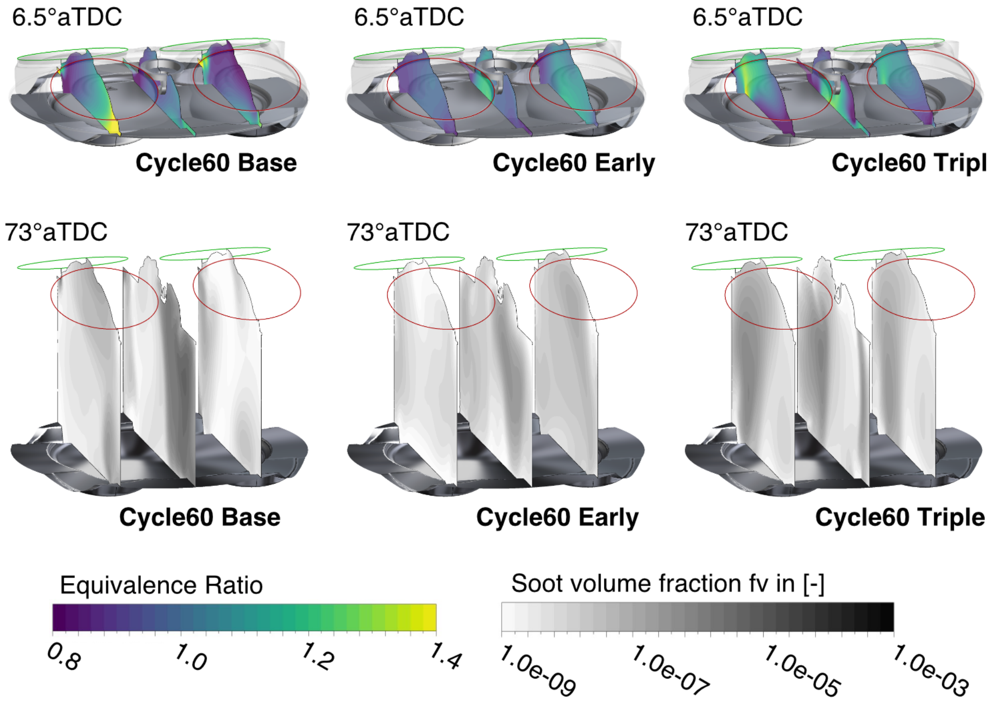

Figure 6.24.: Local equivalence ratio at 6.5 °CA aTDC and soot volume fraction f_v at 73 °CA aTDC for cycle 60 of the reference engine transient, cycle 60 with early single injection at 301 °CA bTDC and cycle 60 with triple injection.

chamber, although not as pronounced. Less inhomogeneity is observed for an early single injection strategy. Although the particle volume fraction increases slightly over the entire range, local extremes, as occur in the reference simulation, are not observed.
Finally, in order to evaluate the influence of early single injection on the observed variations of the soot volume of the reference configuration, a sequence of cycles with a modified injection strategy was investigated. The analysis covers the range from cycle 55 to cycle 60. A comparison of the calculated soot volumes with the reference case is shown in Figure 6.25 (left). All cycles in the sequence achieve similarly low soot volume values. The corresponding uniformity index for each cycle is shown in Figure 6.25 (right) in comparison to the indices of the reference transient. The improvement in mixture homogeneity visually observed in the contour plots (Figure 6.24) can be confirmed by the mean increase in the index.
There are still large fluctuations in the value between cycles. This observation makes it clear that the uniformity index alone is not able to capture the entire emission potential of a cycle. In addition, local phenomena, such as the specific location of a very fuel-rich mixture cloud, are also involved. This is also confirmed by the uniformity index of cycle 60 with triple injection shown in Figure 6.25 (right, yellow dot). While the very late third injection of the strategy leads to a low uniformity index, the different spatial distribution of the mixture in the combustion chamber can also reduce particulate emissions.

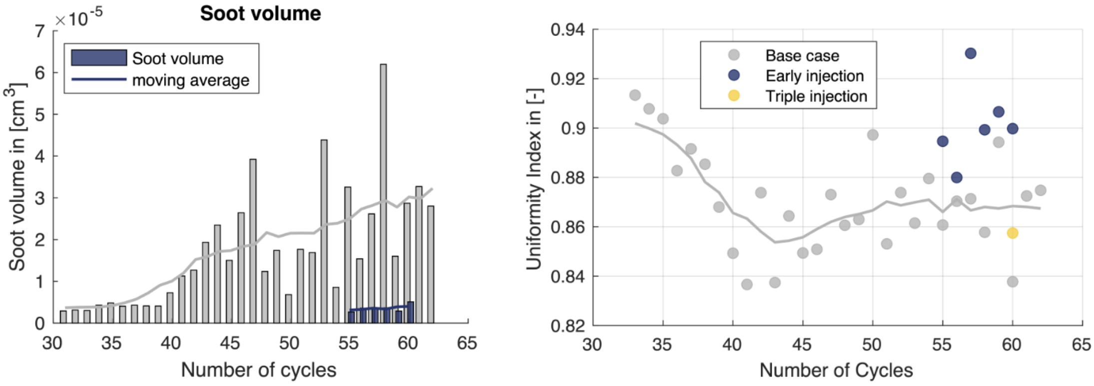

Figure 6.25.: Left: Total soot volumes of a consecutive calculation of 5 cycles starting at cycle 55 in comparison to the calculated volumes of the reference engine transient. Right: Corresponding uniformity index for each cycle of the calculated transient.

The results suggest that shifting the start of fuel injection to an earlier crank angle is reasonable. Both triple and early single injection offer reduction potential compared to the reference configuration of the transient studied. Negative effects from increased spray-wall interaction due to earlier injection is possible, although the influence is estimated to be moderate based on previous studies on cycle 36 (cf. section 6.2).

6.4. Summary and Closing Remarks

In this chapter, the framework presented in Chapter 4 was applied to an RDE relevant emission-critical transient engine scenario using the extensions introduced in Chapter 5 to investigate the root causes of increased particulate emissions. The scenario investigated was derived from a realistic RDE relevant driving scenario and transferred to the highly dynamic engine test bench. It consists of a transient load and speed drop due to a gear change maneuver and subsequent acceleration with observed soot particle emissions.

The scenario was modified according to the requirements of the 3D-CFD and adapted to fixed valve timing. With the aim of analyzing soot particle formation, the 3D-CFD analysis focused on a sequence of 30 subsequent engine cycles in the emission-critical region of the transient at increasing load and speed.

The simulated engine cycles show good agreement in the indicated mean effective pressure and reproduce the load profile well. The trend towards increased particle emissions, both in terms of particle volume and particle number, can also be reflected. An analysis of the mean particle diameters in the domain indicates a high proportion of small particles of diameter less than 23 nm. Conditioning the simulated particle number density on particles larger than 23 nm allows a feasible comparison with experimentally measured particle numbers. Again, a similar progression towards increased soot particle formation can be observed.

For a more detailed analysis of the root causes, the emission-critical region of the transient scenario was divided into three representative subsets: a potential knocking event, a knock aftermath region and a high-load region.

Although the framework presented in this thesis cannot simulate the knock event itself, it can be used to characterize crucial conditions inside the engine and derive potential causes for the experimentally observed phenomena. The combined findings from both sides, experiment and simulation, ruled out a contribution of the knock event to the observed soot emissions and instead attributed the experimental observation to a potential detachment of deposits.

Several parameter adjustments by the engine control unit and condition changes were observed in the knock aftermath region. A key contributor to soot formation was the overall fuel-rich operating condition. As a result, an increase in the particle number density throughout the entire engine domain was observed.

Particle emissions in the high-load range could be attributed to local mixture inhomogeneities. An analysis of the uniformity index suggested that this occurrence is related to the shift of the injection timing and can vary strongly from cycle to cycle. A more detailed analysis of the mixture field was able to identify the mechanism behind this observation.

In the next step, specific control parameters were varied for individual engine cycles to counteract the observed root causes. Particle emissions were significantly reduced in the knock aftermath region by reducing the injected fuel mass and thus returning to global stoichiometric conditions. The very fuel-rich mixture zones observed locally in the high-load range were counteracted by varying the injection timing. Comparing the reference injection timing with an early injection timing and an alternative multi-injection mode, the original mechanism responsible for the strong local inhomogeneity was suppressed for both cases and a reduction in soot volume fraction was achieved. It is worth noting that early single injection has a higher reduction potential than multiple injection.

This investigation successfully demonstrated how the built framework and methodology for transient engine simulation enables the detailed analysis of individual emission-critical scenarios. It should be emphasized that the methodology does not stand for itself, but is largely dependent on a characterization of the scenario on the engine test bench. Combined with experimental measurement data, however, it offers a unique opportunity to look inside the engine and gain a comprehensive understanding of the processes taking place.

7. Conclusions and Outlook

In this thesis, a 3D-CFD framework for simulating soot particle emissions in a direct-injection internal combustion engine during transient engine operation is presented and applied to a series production engine to investigate a real driving emission (RDE) relevant and emission-critical driving scenario. The aim of this work is to demonstrate the potential of 3D-CFD as a tool for the targeted analysis of individual transient engine scenarios. This is carried out in three steps:
First, a framework for the simulation and analysis of soot particle emissions from the direct-injection gasoline engine in steady-state operation was developed and evaluated using optically available engine data. In the next step, the framework was extended for the investigation of consecutive multi-cycle simulations and the application at transient operating points. Particular emphasis was given to preparing and providing suitable experimental boundary conditions and to the parallelization of consecutive engine cycles. Finally, the extended framework was used to simulate transient operating points based on an RDE-relevant and soot emission-critical driving scenario to identify causes of increased soot particle emissions and reveal optimization potentials in a combined experimental-numerical cause-and-effect chain analysis.

The presented framework is built around the flow solver ANSYS® CFX® and is based on a number of standard implemented solutions and models for the simulation of combustion engines. In the context of this work, it was extended by a detailed moment-based soot model for accurate simulation of soot particle emissions. The coupled quadrature method of moments (QMOM) soot model describes the evolution of the polydisperse system of soot particles, considering all relevant physico-chemical processes such as nucleation, coagulation, surface growth and oxidation of soot particles. Furthermore, an additional transport equation was introduced to accurately represent gas-phase soot precursors.
The evaluation of the framework using the steady-state operating point of an optically accessible research engine was able to achieve good agreement with the available soot extinction and soot luminescence measurements. In an accompanying cause-and-effect chain analysis, the soot formation chain was traced over the entire engine cycle. It was thus possible to show that the presented methodology is capable of covering all relevant mechanisms and can therefore be used as a diagnostic tool.

The extension of the framework for the investigation of transient engine operation by means of consecutive multi-cycle simulations includes methods regarding the preparation and handling of available experimental reference data, the calculation of transient intake and exhaust boundary conditions using 1D gas exchange analysis and a concept for the parallelization of consecutive engine cycles.

For the transfer of a transient engine scenario recorded on the test bench into the virtual engine environment, a strategy was presented that allows phase-shifted realizations to be averaged. The result is a set of consecutive, ensemble-averaged and crank angle resolved engine cycles along the transient scenario, including assigned control parameters and boundary conditions. To provide extended boundary conditions, the 1D gas exchange analysis methodology was modified to include the consecutive progression of multiple cycles throughout the scenario. The resulting crank angle resolved intake mass flow and exhaust pressure boundary conditions, as well as averaged wall temperatures to each cycle of the engine transient, serve as boundary conditions for the 3D-CFD. To reduce the computational time required by large consecutive multi-cycle simulations, a method for parallelizing the cycle sequence using multiple threads was introduced. Depending on the thread partitioning, this strategy significantly reduces the total computation time of a full transient engine scenario.

With this extended framework, all the necessary information is available to transfer the characterized transient engine scenario from the test bench into 3D-CFD.

The extended framework was applied to investigate particulate emissions in a RDE-relevant emission-critical transient engine scenario. The scenario of interest is characterized by a transient load and speed drop due to a gear change maneuver and subsequent acceleration with observed soot particle emissions.

The simulated transient engine cycles show good agreement in the indicated mean effective pressure and reproduce the load profile well. The trend toward increased particle emissions, both in terms of particle volume and particle number, is also reflected by the simulation. To identify the root causes of the increased particulate emissions observed on the engine test bench, the emission-critical region of the scenario was analyzed in more detail in three regions.

Region 1 is determined by an experimentally observed knock event. However, a combined experimental-numerical analysis did not prove a direct effect of the event on the observed increased particle emissions. Instead, experimental observations were attributed to a potential detachment of deposits. For Region 2, effects on soot particle formation due to global substoichiometric conditions were observed. As a result, a significant increase in particle number density was detected with a moderate increase in particle volume. In Region 3, the region with the highest particle emissions, the particle formation was dominated by local inhomogeneities.

A detailed analysis of the mixing field identified the mechanism behind the inhomogeneities. In a final step, it was possible to reveal optimization potentials based on the knowledge gained through targeted variation of the control parameters in individual cycles. Two alternative injection strategies were tested, an SOI shift to early injection and an alternative triple injection strategy. Both strategies were able to disrupt the initially identified mechanism for increased soot formation and demonstrated reduction potential. The simulated trend toward a reduction in soot emissions was confirmed later by additional test bench measurements.

Summarizing this work, the initially posed scientific questions can be answered. It is demonstrated that existing numerical submodels can successfully be extended and adapted to address current questions in the context of transient engine scenarios. The extended framework presented is suited to process test bench data, provide required boundary conditions and subsequently characterize the transient engine scenario of interest in the virtual engine environment. This work also proposes a way of balancing the high numerical costs by using a thread-based approach even though these kinds of scenarios remain complex and resource intensive.

In conclusion, this work presents a 3D-CFD multi-cycle framework for transient engine scenarios which complements the development process for sustainable and low-emission internal combustion engines. The methodology can be used as a targeted diagnostic tool for a detailed analysis of individual transient engine scenarios and thus contributes to building understanding and identifying possible optimization measures. However, a precise characterization of the scenario that is to be investigated is essential for the transfer into the virtual engine model. For this reason, a close integration of experiment and simulation is recommended in order to benefit from the synergy effects of both perspectives.

Outlook

Due to the complexity of the entire cause-and-effect chain in gasoline direct-injection engines, the overall modeling error is determined by the weakest submodel. Hence, to further improve on predictive capabilities of the proposed overall modeling framework developments in the following areas could be beneficial.

Depending on which phenomena need to be examined more closely, the use of scale-resolving simulation methods, improved models of direct injection and wall film formation or models for the special treatment of wall film pyrolysis could enhance the simulation accuracy.

Furthermore, it is possible to use improved soot models with continuous reconstruction of the particle size distribution to consider the influence of oxygenated fuels on the formation of very small particles.

A. Discussion Variable vs. Fixed Valve Timing

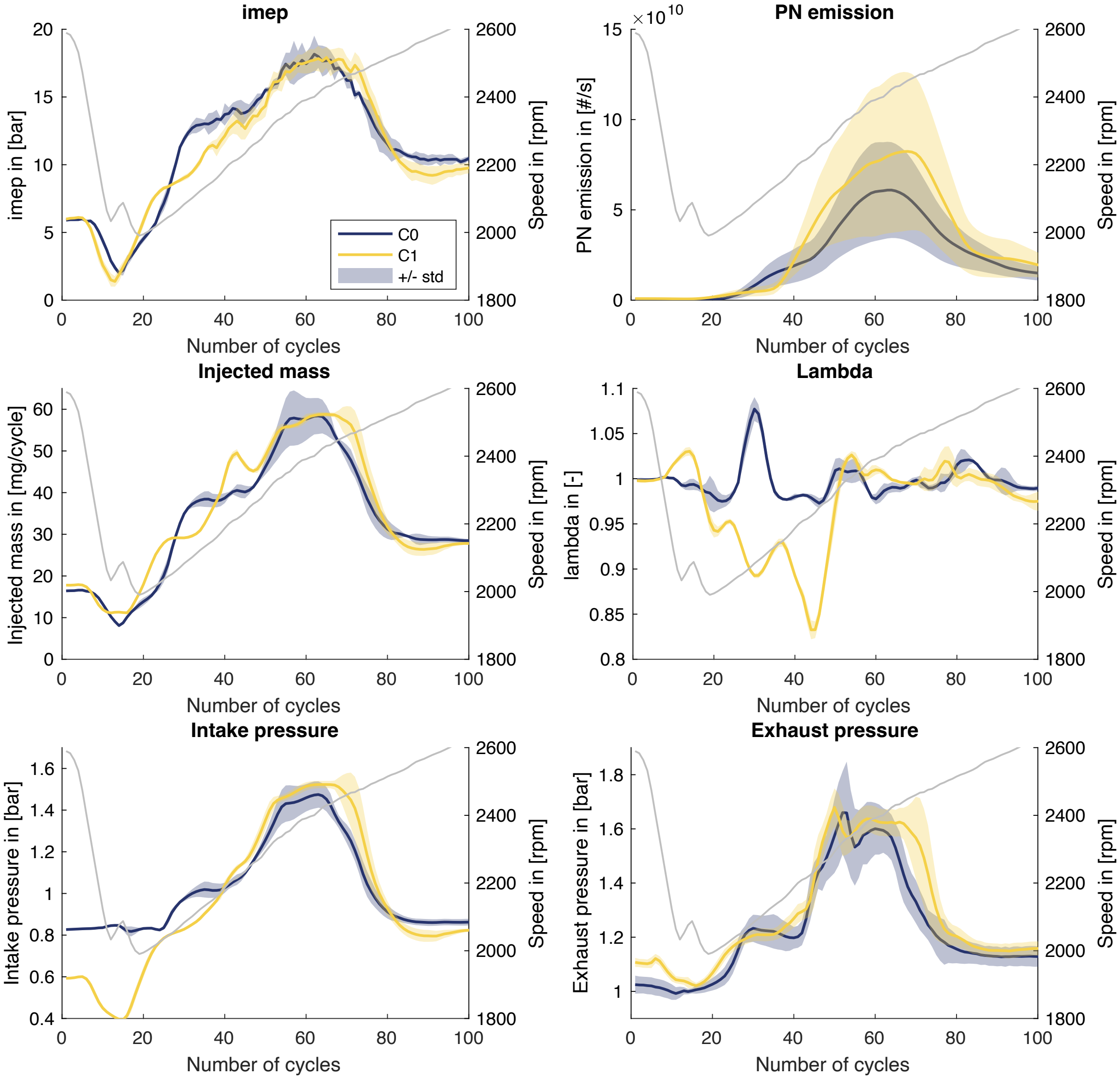

Figure A.1.: Characteristic engine parameters of the BMW B48 transient engine scenario with full variable valve timing and lift (Configuration 0 - C0) and fixed valve timing (Configuration 1 - C1). Part 1/2

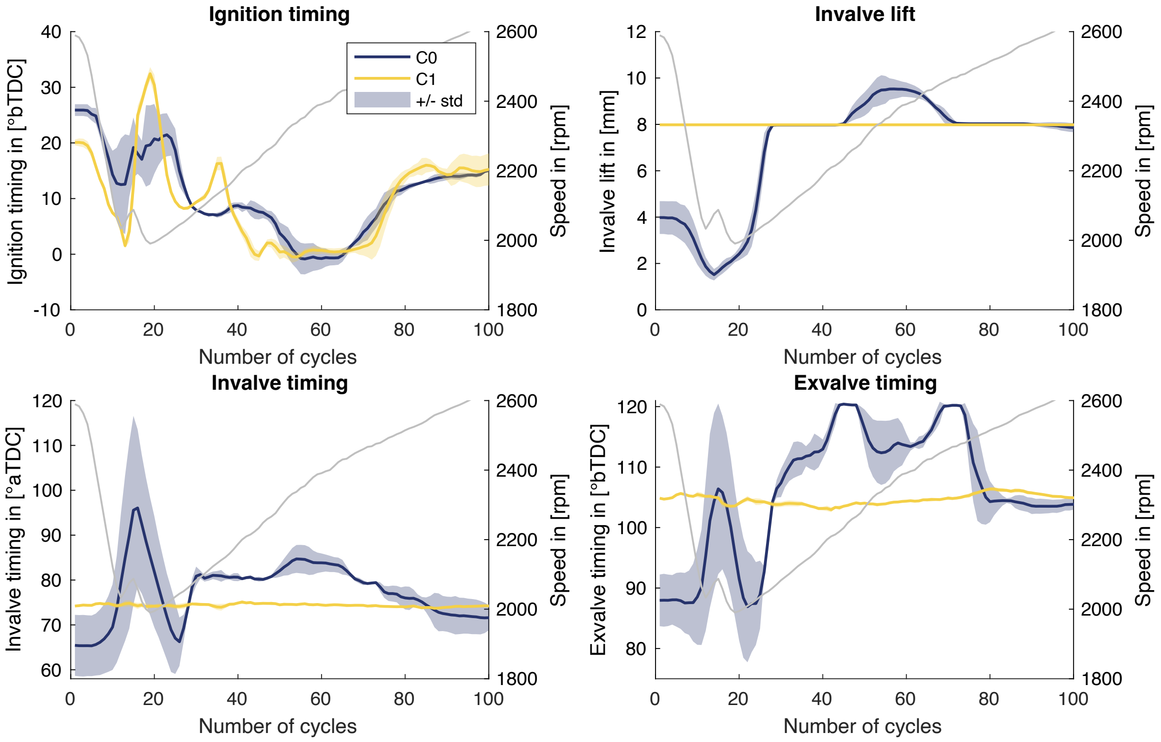

Figure A.2.: Characteristic engine parameters of the BMW B48 transient engine scenario with full variable valve timing and lift (Configuration 0 - C0) and fixed valve timing (Configuration 1 - C1). Part 2/2

To make the transient engine scenario feasible for the 3D-CFD investigation, the scenario was reproduced on the engine test bench with fixed valve timing and valve lift as part of the study presented here. A comparison of both configurations, once with variable valve timing (Configuration 0 - C0) and once with fixed valve timing (Configuration 1 - C1) is shown represented by their characteristic control parameters in Figure A.1, A.2 and A.3.

The adapted transient engine scenario is able to reproduce the load scenario well. A collapse of the engine load in the range from cycle 30 to 40 is noticeable. In this range, it can be observed how the actual lambda value for C1 drops significantly. This phenomenon is presumably due to the restriction of the control unit due to the fixed control times by the user. Another difference can be observed for the intake pressure in the lower load range. Here, a significantly higher pressure loss is visible due to the held valve lift and the throttling of the intake flow required as a result.

A comparison of both injection strategies is shown in Figure A.3. It is striking here how C1 switches to a multiple injection strategy in the high load range. The influence of such a strategy was investigated in detail in section 6.3.

Despite all the distinctions, both configurations show similar emission behavior over the course of the transient. Other control parameters also show a similar reaction.

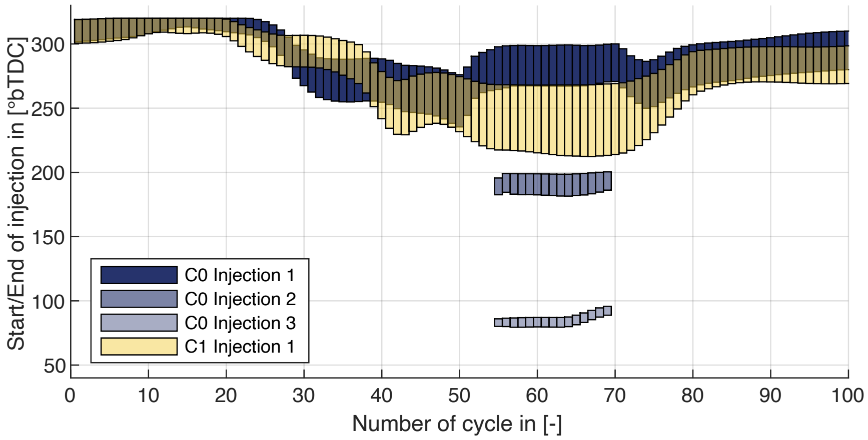

Figure A.3.: Comparison of different injection timing between full variable (C0) and fixed valve timing (C1). The bar for each cycle indicates the duration of the injection.

List of Symbols

Characteristic Numbers

Le	Lewis number
Nu	Nusselt number
Pr_t	Turbulent Prandtl number
Re_p	Particle Reynolds number
Sc_t	Turbulent Schmidt number
Sh	Sherwood number
We_p	Particle Weber number

Greek Symbols

χ_Z	Scalar dissipation rate of the mixture fraction
κ	Flame curvature
ϕ	Fuel-air equivalence ratio (Equivalence ratio)
σ_t	Turbulent flame surface area ratio
α_1	SST model constant
α_2	SST model constant
α_3	SST model constant
β_1	SST model constant
β_2	SST model constant
β_3	SST model constant
β^*	SST model constant
c_χ	Model constant
δ	Dirac delta function
δ_{ij}	Kronecker Delta
δ_f	Wall film thickness
ε	Turbulent dissipation rate
η_f	Fuel conversion efficiency

κ	Von Kármán constant
λ	Thermal conductivity
λ	Air-fuel equivalence ratio
μ	Dynamic viscosity
μ_{eff}	Effective dynamic viscosity
μ_t	Turbulent dynamic viscosity
μ_g	Gas phase dynamic viscosity
ν	Stoichiometric mass ratio
ν'_k	Stoichiometric coefficient of reactant species k
ν''_k	Stoichiometric coefficient of product species k
$\dot{\omega}_k$	Mass source term of species k due to chemical reaction
ω	Turbulent frequency
ϕ	Arbitrary scalar
ρ	Density
ρ_g	Gas phase density
ρ_p	Particle/parcel density
σ	Surface tension
σ_{k1}	SST model constant
σ_{k2}	SST model constant
σ_{k3}	SST model constant
$\sigma_{\omega 1}$	SST model constant
$\sigma_{\omega 2}$	SST model constant
$\sigma_{\omega 3}$	SST model constant
τ_{ij}	Viscous stress tensor
τ_p	Particle time scale
$\boldsymbol{\xi}, \xi_i$	Soot particle property i

Operators

∇	Gradient
$\nabla_{\|\|}$	Gradient tangential to the mean flame front
$\overline{\square}$	Average with respect to time
$\dot{\square}$	Temporal derivative
$\widetilde{\square}$	Density based average with respect to time / Favre average
$\square''$	Fluctuating part of Favre decomposition

Roman Symbols

A	Antoine model constant

AFR	Air-fuel ratio
A_p	Wetted wall area
$A_{w,cv}$	Wall surface of wall element
B	Antoine model constant
C	Antoine model constant
C_D	Drag coefficient
D_k	Diffusion coefficient of species k into the mixture
D_t	Turbulent diffusivity
D'_t	Turbulent diffusivity based on mixing length approach
F_1	SST model blending function
F_2	SST model blending function
$F_{B,i}$	Buoyancy force in direction i
$F_{BA,i}$	Basset force in direction i
$F_{D,i}$	Drag force in direction i
$F_{P,i}$	Pressure gradient force in direction i
$F_{R,i}$	Rotational forces in direction i
$F_{VM,i}$	Virtual mass force in direction i
G	G-scalar
G_0	G-scalar isosurface / flame front location
G''^2	Variance of the G-scalar
LHV	Lower heating value
N_D	Number of Dirac delta functions
N_c	Number of species
P	Presumed probability density function (pdf)
P_b	Brake power
P_i	Indicated power
P_k	Production term of kinetic energy
Q_{cond}	Conductive heat transfer
Q_{conv}	Convective heat transfer
Q_{evap}	Evaporative heat transfer
R	Universal gas constant
$\dot{S}_{h_t}$	Source term total enthalpy equation
S_{ij}	Rate of strain tensor
$\dot{S}_m$	Source term mass equation
$\dot{S}_u$	Source term momentum equation
T	Temperature
T	Time interval

T	Engine torque
T_{pA}	Pure adhesion temperature
T_{pR}	Pure rebound temperature
Tr	Tracer
UI_{ϕ}	Uniformity index
$V_{k,i}$	Diffusion velocity of species k in direction i
V	Volume
V	Soot particle volume
V_d	Cylinder displacement volume
V_i	Position i of Dirac delta function
Vol_{cv}	Volume of wall element
V_{tot}	Total cylinder volume
W	Molecular weight of the mixture
W_k	Molecular weight of species k
X_k	Mole Fraction of species k
$X_{s,k}$	Mole Fraction at the particle/parcel surface of species k
Y_k	Mass Fraction of species k
$Y_{s,k}$	Mass Fraction at the particle/parcel surface of species k
Z	Mixture fraction
Z''^2	Variance of the mixture fraction
Z_{st}	Stoichiometric mixture fraction
a_1	SST model constant
b_1	Model constant
b_3	Model constant
$bmep$	Brake mean effective pressure
c	Reaction progress
c'	Additional progress variable
c_{μ}	Model constant
c_p	Heat capacity at constant pressure
c_s	Model constant
d_p	Particle/parcel diameter
e	Specific internal energy
f_v	Soot volume fraction
g_i	Gravitational acceleration in direction i
h	Specific enthalpy
h	Heat transfer coefficient
$h^0_{f,k}$	Standard enthalpy of formation of species k

h_t	Specific total enthalpy
$\Delta h_{v,k}$	Specific enthalpy of evaporation of species k
i	Number of engine cycles per crankshaft revolution
$imep$	Indicated mean effective pressure
k	Mass transfer coefficient
k	Turbulent kinetic energy
l^*	Length ratio
l_f	Laminar flame thickness
$l_{f,t}$	Turbulent flame brush thickness
m	Number of carbon atoms
$\dot{m}$	Mass flow
$\dot{m}_f$	Consumed fuel mass flow
m_k	Moment of the order of k
m_p	Particle/parcel mass
n	Number density function
n	Number of hydrogen atoms
n	Engine speed
$\mathbf{n}, n_i$	Normal vector in direction i
n^*	Approximated number density function
p	Pressure
$p_{vap,k}^{pure}$	Vapor pressure of the pure phase of species k
p_{vap}	Total vapor pressure
$p_{vap,k}$	Partial vapor pressure of component k
q_i	Energy flux in direction i
q	Model constant
r_{pw}	Volume fraction of all wall particles in wall element
sfc	Specific fuel consumption
s_L	Laminar burning velocity
s_T	Turbulent burning velocity
s_T^0	Unstreched turbulent burning velocity
t	Time
$\mathbf{u}, u_i$	Velocity in direction i
$u_{p,i}$	Particle/parcel velocity in direction i
$u_{g,i}$	Gas phase velocity in direction i
$u_{s,i}$	Slip velocity in direction i
w_i	Weight i of Dirac delta function
$\mathbf{x}, x_i$	Spatial coordinate in direction i

$\mathbf{x}_f$	Spatial coordinate of the flame front
x_n	Normal flamelet coordinate
y	Spatial coordinate in wall normal direction
z	Number of engine cylinders

Subscripts

$\square_{EGR}$	Recirculated exhaust gas
$\square_F$	Fuel
$\square_{Ox}$	Oxidizer
$\square_{b,burnt}$	Burnt state
$\square_{fresh}$	Fresh unburnt species
$\square_g$	Gas phase variable
$\square_{i,j}$	Direction index
$\square_k$	Species index
$\square_p$	Particle/parcel variable
$\square_{st}$	Stoichiometric conditions
$\square_{u,unb}$	Unburnt state
$\square_w$	Wall element variable
$\square_{wp}$	Wall particle/parcel variable

Superscripts

$\square^L$	Liquid phase
$\square^V$	Vapor phase

List of Acronyms

AALH	Aromatic aliphatic linked hydrocarbon
BDC	Bottom dead center
CCV	Cycle-to-cycle variation
CFD	Computational Fluid Dynamics
ECU	Engine control unit
EGR	Exhaust gas recirculation/ Recirculated exhaust gas
EVO	Exhaust valve opens
FOV	Field of view
GDI	Gasoline direct-injection
HACA	H-absorption-C_2H_2-addition
ICE	Internal combustion engine
IVC	Intake valve closes
IVO	Intake valve opens
LOS	Line-of-sight
MOMIC	Method of moments with interpolative closure
MPM	Moment projection methods
NDF	Number density function
PAH	Polycyclic aromatic hydrocarbon
PBE	Population balance equation
PCAH	Pericondensed aromatic hydrocarbon
pdf	Probability density function
PN	Particulate number
QMOM	Quadrature method of moments
RDE	Real driving emissions
SOI	Start of injection
SST	Shear-stress-transport
TDC	Top dead center
TPA	Three-pressure-analysis

URANS	Unsteady Reynolds averaged Navier-Stokes equation

List of Figures

List of Tables

Bibliography

[1] **F. Held**, J. Reusch, S. Salenbauch, and C. Hasse. “A 3D Computational Study of the Formation, Growth and Oxidation of Soot Particles in an Optically Accessible Direct-Injection Spark-Ignition Engine Using Quadrature-Based Methods of Moments”. In: *Fuel Processing Technology* 254 (Feb. 2024), p. 107923. DOI: `10.1016/j.fuproc.2023.107923`.

[2] M. U. Ali, G. Liu, B. Yousaf, H. Ullah, Q. Abbas, and M. A. M. Munir. “A Systematic Review on Global Pollution Status of Particulate Matter-Associated Potential Toxic Elements and Health Perspectives in Urban Environment”. In: *Environmental Geochemistry and Health* 41.3 (June 2019), pp. 1131–1162. DOI: `10.1007/s10653-018-0203-z`.

[3] S. Heydari, M. Tainio, J. Woodcock, and A. De Nazelle. “Estimating Traffic Contribution to Particulate Matter Concentration in Urban Areas Using a Multilevel Bayesian Meta-Regression Approach”. In: *Environment International* 141 (Aug. 2020), p. 105800. DOI: `10.1016/j.envint.2020.105800`.

[4] Commission Regulation (EU) 2023/443. *Commission Regulation (EU) 2023/443 of 8 February 2023 Amending Regulation (EU) 2017/1151 as Regards the Emission Type Approval Procedures for Light Passenger and Commercial Vehicles*. 2023.

[5] European Commission. Directorate General for Internal Market, Industry, Entrepreneurship and SMEs. *Euro 7 Standards: New Rules for Vehicle Emissions*. LU: Publications Office, 2022.

[6] E. G. G. Constantine D. Rakopoulos. *Diesel Engine Transient Operation*. Springer-Verlag GmbH, 2009.

[7] R. Stone. *Introduction to Internal Combustion Engines*. 3rd ed. Warrendale, Pa: Society of Automotive Engineers, 1999.

[8] A. Scholtissek, S. Buhl, D. Hain, and C. Hasse. “Internal Combustion Engine - Cause and Effect Chain”. In: (2017). DOI: `10.6084/m9.figshare.5170480.v3`.

[9] G. Faeth, L.-P. Hsiang, and P.-K. Wu. “Structure and Breakup Properties of Sprays”. In: *International Journal of Multiphase Flow* 21 (Dec. 1995), pp. 99–127. DOI: `10.1016/0301-9322(95)00059-7`.

[10] E. Stevens and R. Steeper. “Piston Wetting in an Optical DISI Engine: Fuel Films, Pool Fires, and Soot Generation”. In: *SAE 2001 World Congress*. Mar. 2001, pp. 2001-01–1203. DOI: `10.4271/2001-01-1203`.

[11] P. Merker. *Grundlagen Verbrennungsmotoren*. 2019. DOI: `10.1007/978-3-658-23557-4`.

[12] J. B. Heywood. *Internal Combustion Engine Fundamentals*. Second edition. New York: McGraw-Hill Education, 2018.

[13] K.-H. Dietsche, K. Reif, and R. B. GmbH, eds. *Kraftfahrtechnisches Taschenbuch: Kfz-Fachwissen kompakt*. 28., überarb. und erw. Aufl. Studium und Praxis. Wiesbaden: Springer Vieweg, 2014.

[14] K. Reif, ed. *Abgastechnik für Verbrennungsmotoren*. Wiesbaden: Springer Fachmedien Wiesbaden, 2015. DOI: `10.1007/978-3-658-09522-2`.

[15] S. Gordon and B. J. McBride. *Computer Program for Calculation of Complex Chemical Equilibrium Compositions, Rocket Performance, Incident and Reflected Shocks, and Chapman-Jouquet Detonations*. Tech. rep. NASA-SP-273. NASA Langley Research Center, 1971.

[16] R. Kee, F. Rupley, and J. Miller. *The Chemkin Thermodynamic Data Base*. Tech. rep. SAND-87-8215B, 7073290, ON: DE90007953. Mar. 1990, SAND-87–8215B, 7073290, ON: DE90007953. DOI: `10.2172/7073290`.

[17] T. Poinsot and D. Veynante. *Theoretical and Numerical Combustion*. 3. ed. Toulouse: CNRS, 2011.

[18] F. Menter. “Zonal Two Equation K-w Turbulence Models For Aerodynamic Flows”. In: *23rd Fluid Dynamics, Plasmadynamics, and Lasers Conference*. Reston, Virigina: American Institute of Aeronautics and Astronautics, July 1993. DOI: `10.2514/6.1993-2906`.

[19] B. Launder and D. Spalding. “The Numerical Computation of Turbulent Flows”. In: *Computer Methods in Applied Mechanics and Engineering* 3.2 (Mar. 1974), pp. 269–289. DOI: `10.1016/0045-7825(74)90029-2`.

[20] D. C. Wilcox. “Multiscale Model for Turbulent Flows”. In: *AIAA Journal* 26.11 (Nov. 1988), pp. 1311–1320. DOI: `10.2514/3.10042`.

[21] F. Menter, M. Kuntz, and R. Langtry. “Ten Years of Industrial Experience with the SST Turbulence Model”. In: *Turbulencee, Heat and Mass Transfer* 4 (Jan. 2003).

[22] L. Schiller and A. Naumann. “A Drag Coefficient Correlation”. In: *Zeitschrift des Vereins Deutscher Ingenieure* 77 (1935), pp. 318–320.

[23] W. E. Ranz and W. R. Marshall. “Evaporation from Drops”. In: *Chemical Engineering Progress* 48 (1952), pp. 142–146, 173–180.

[24] G. Elsaesser. “Experimentelle Untersuchung Und Numerische Modellierung Der Freien Kraftstoffstrahlausbreitung Und Wandinteraktion Unter Motorischen Randbedingungen”. PhD thesis. 2002.

[25] ANSYS Inc. *ANSYS CFX-Solver Theory Guide - Release 2022 R2*. July 2022.

[26] C. Bai and A. D. Gosman. “Development of Methodology for Spray Impingement Simulation”. In: *International Congress & Exposition*. Feb. 1995, p. 950283. DOI: `10.4271/950283`.

[27] M. Muehlbauer. “Modeling Wall Interactions of a High-Pressure, Hollow Cone Spray”. PhD thesis. Technische Universität Darmstadt, 2009.

[28] N. Peters. “Combustion Theory”. In: *CEFRC Summerschool Princeton*. 2010.

[29] F. A. Williams. “3. Turbulent Combustion”. In: *The Mathematics of Combustion*. Ed. by J. D. Buckmaster. Society for Industrial and Applied Mathematics, Jan. 1985, pp. 97–131. DOI: `10.1137/1.9781611971064.ch3`.

[30] D. Veynante and L. Vervisch. “Turbulent Combustion Modeling”. In: *Progress in Energy and Combustion Science* (2002).

[31] N. Peters. *Turbulent Combustion*. Cambridge University Press, 2000. DOI: `10.1017/cbo9780511612701`.

[32] N. Peters. “The Turbulent Burning Velocity for Large-Scale and Small-Scale Turbulence”. In: *Journal of Fluid Mechanics* 384 (Apr. 1999), pp. 107–132. DOI: `10.1017/S0022112098004212`.

[33] J. Ewald. “A Level Set Based Flamelet Model for the Prediction of Combustion in Homogeneous Charge and Direct Injection Spark Ignition Engines”. PhD thesis. RWTH Aachen, 2006.

[34] S. Toninel, H. Forkel, T. Frank, B. Durst, C. Hasse, and D. Linse. “Implementation and Validation of the G-equation Model Coupled with Flamelet Libraries for Simulating Premixed Combustion in I.C. Engines”. In: *SAE Technical Papers* 2.1 (Apr. 2009), pp. 674–690. DOI: `10.4271/2009-01-0709`.

[35] S. Salenbauch. “Modelling of Soot Formation and Oxidation in Reacting Flows”. PhD thesis. Technische Universität Darmstadt, 2018.

[36] D. R. Tree and K. I. Svensson. “Soot Processes in Compression Ignition Engines”. In: *Progress in Energy and Combustion Science* 33.3 (June 2007), pp. 272–309. DOI: `10.1016/j.pecs.2006.03.002`.

[37] H. Bockhorn, ed. *Soot Formation in Combustion*. Springer Berlin Heidelberg, 1994. DOI: `10.1007/978-3-642-85167-4`.

[38] C. Saggese, N. E. Sánchez, A. Frassoldati, A. Cuoci, T. Faravelli, M. U. Alzueta, and E. Ranzi. “Kinetic Modeling Study of Polycyclic Aromatic Hydrocarbons and Soot Formation in Acetylene Pyrolysis”. In: *Energy & Fuels* 28.2 (Feb. 2014), pp. 1489–1501. DOI: `10.1021/ef402048q`.

[39] G. Blanquart, P. Pepiot-Desjardins, and H. Pitsch. “Chemical Mechanism for High Temperature Combustion of Engine Relevant Fuels with Emphasis on Soot Precursors”. In: *Combustion and Flame* 156.3 (Mar. 2009), pp. 588–607. DOI: `10.1016/j.combustflame.2008.12.007`.

[40] M. Frenklach and H. Wang. “Detailed Modeling of Soot Particle Nucleation and Growth”. In: *Symposium (International) on Combustion* 23.1 (Jan. 1991), pp. 1559–1566. DOI: `10.1016/S0082-0784(06)80426-1`.

[41] M. Frenklach and H. Wang. “Detailed Mechanism and Modeling of Soot Particle Formation”. In: 1994, pp. 165–192. DOI: `10.1007/978-3-642-85167-4_10`.

[42] C. S. McEnally, L. D. Pfefferle, B. Atakan, and K. Kohse-Höinghaus. “Studies of Aromatic Hydrocarbon Formation Mechanisms in Flames: Progress towards Closing the Fuel Gap”. In: *Progress in Energy and Combustion Science* 32.3 (Jan. 2006), pp. 247–294. DOI: `10.1016/j.pecs.2005.11.003`.

[43] H. Richter and J. Howard. “Formation of Polycyclic Aromatic Hydrocarbons and Their Growth to Soot—a Review of Chemical Reaction Pathways”. In: *Progress in Energy and Combustion Science* 26.4-6 (Aug. 2000), pp. 565–608. DOI: `10.1016/S0360-1285(00)00009-5`.

[44] M. Frenklach. “Reaction Mechanism of Soot Formation in Flames”. In: *Physical Chemistry Chemical Physics* 4.11 (May 2002), pp. 2028–2037. DOI: `10.1039/b110045a`.

[45] Y. Yoshihara, A. Kazakov, H. Wang, and M. Frenklach. “Reduced Mechanism of Soot Formation—Applicationto Natural Gas-Fueled Diesel Combustion”. In: *Symposium (International) on Combustion* 25.1 (1994), pp. 941–948. DOI: `10.1016/S0082-0784(06)80730-7`.

[46] M. Sirignano, J. Kent, and A. D’Anna. “Modeling Formation and Oxidation of Soot in Nonpremixed Flames”. In: *Energy & Fuels* 27.4 (Apr. 2013), pp. 2303–2315. DOI: `10.1021/ef400057r`.

[47] H. A. Michelsen, M. B. Colket, P.-E. Bengtsson, A. D'Anna, P. Desgroux, B. S. Haynes, J. H. Miller, G. J. Nathan, H. Pitsch, and H. Wang. "A Review of Terminology Used to Describe Soot Formation and Evolution under Combustion and Pyrolytic Conditions". In: *ACS Nano* 14.10 (Oct. 2020), pp. 12470–12490. DOI: `10.1021/acsnano.0c06226`.

[48] G. Blanquart and H. Pitsch. "A Joint Volume-Surface-Hydrogen Multivariate Model for Soot Formation". In: *Combustion Generated Fine Carbonaceous Particles*. KIT Scientific Publishing, 2009.

[49] K. Neoh, J. Howard, and A. Sarofim. "Effect of Oxidation on the Physical Structure of Soot". In: *Symposium (International) on Combustion* 20.1 (Jan. 1985), pp. 951–957. DOI: `10.1016/S0082-0784(85)80584-1`.

[50] C. A. Echavarria, I. C. Jaramillo, A. F. Sarofim, and J. S. Lighty. "Studies of Soot Oxidation and Fragmentation in a Two-Stage Burner under Fuel-Lean and Fuel-Rich Conditions". In: *Proceedings of the Combustion Institute* 33.1 (2011), pp. 659–666. DOI: `10.1016/j.proci.2010.06.149`.

[51] S. Salenbauch, A. Cuoci, A. Frassoldati, C. Saggese, T. Faravelli, and C. Hasse. "Modeling Soot Formation in Premixed Flames Using an Extended Conditional Quadrature Method of Moments". In: *Combustion and Flame* 162.6 (June 2015), pp. 2529–2543. DOI: `10.1016/j.combustflame.2015.03.002`.

[52] C. Saggese, A. Frassoldati, A. Cuoci, T. Faravelli, and E. Ranzi. "A Wide Range Kinetic Modeling Study of Pyrolysis and Oxidation of Benzene". In: *Combustion and Flame* 160.7 (July 2013), pp. 1168–1190. DOI: `10.1016/j.combustflame.2013.02.013`.

[53] A. Cuoci, A. Frassoldati, T. Faravelli, and E. Ranzi. "A Computational Tool for the Detailed Kinetic Modeling of Laminar Flames: Application to C2H4/CH4 Coflow Flames". In: *Combustion and Flame* 160.5 (May 2013), pp. 870–886. DOI: `10.1016/j.combustflame.2013.01.011`.

[54] M. R. Djokic, K. M. Van Geem, C. Cavallotti, A. Frassoldati, E. Ranzi, and G. B. Marin. "An Experimental and Kinetic Modeling Study of Cyclopentadiene Pyrolysis: First Growth of Polycyclic Aromatic Hydrocarbons". In: *Combustion and Flame* 161.11 (Nov. 2014), pp. 2739–2751. DOI: `10.1016/j.combustflame.2014.04.013`.

[55] H. Chen and R. Dobbins. "Crystallogenesis of Particles Formed in Hydrocarbon Combustion". In: *Combustion Science and Technology* 159.1 (Oct. 2000), pp. 109–128. DOI: `10.1080/00102200008935779`.

[56] M. Mueller, G. Blanquart, and H. Pitsch. "Hybrid Method of Moments for Modeling Soot Formation and Growth". In: *Combustion and Flame* 156.6 (June 2009), pp. 1143–1155. DOI: `10.1016/j.combustflame.2009.01.025`.

[57] A. Wick, T.-T. Nguyen, F. Laurent, R. O. Fox, and H. Pitsch. “Modeling Soot Oxidation with the Extended Quadrature Method of Moments”. In: *Proceedings of the Combustion Institute* 36.1 (2017), pp. 789–797. DOI: `10.1016/j.proci.2016.08.004`.

[58] J. Gao and T.-W. Kuo. “Toward the Accurate Prediction of Soot in Engine Applications”. In: *International Journal of Engine Research* 20.7 (Sept. 2019), pp. 706–717.

[59] S. Fontanesi, M. Del Pecchia, V. Pessina, S. Sparacino, and S. Di Iorio. “Quantitative Investigation on the Impact of Injection Timing on Soot Formation in a GDI Engine with a Customized Sectional Method”. In: *International Journal of Engine Research* 23.4 (Apr. 2022), pp. 624–637. DOI: `10.1177/1468087421993955`.

[60] F. Berni, F. Mortellaro, V. Pessina, S. Paltrinieri, F. Pulvirenti, V. Rossi, M. Borghi, and S. Fontanesi. “Modeling of Gaseous Emissions and Soot in 3D-CFD in-Cylinder Simulations of Spark-Ignition Engines: A Methodology to Correlate Numerical Results and Experimental Data”. In: *International Journal of Engine Research* (July 2022), p. 146808742211125. DOI: `10.1177/14680874221112564`.

[61] M. Frenklach. “Method of Moments with Interpolative Closure”. In: *Chemical Engineering Science* 57.12 (June 2002), pp. 2229–2239. DOI: `10.1016/S0009-2509(02)00113-6`.

[62] M. Frenklach and S. J. Harris. “Aerosol Dynamics Modeling Using the Method of Moments”. In: *Journal of Colloid and Interface Science* 118.1 (July 1987), pp. 252–261. DOI: `10.1016/0021-9797(87)90454-1`.

[63] D. L. Marchisio, J. T. Pikturna, R. O. Fox, R. D. Vigil, and A. A. Barresi. “Quadrature Method of Moments for Population-Balance Equations”. In: *AIChE Journal* 49.5 (May 2003), pp. 1266–1276. DOI: `10.1002/aic.690490517`.

[64] D. L. Marchisio and R. O. Fox. “Solution of Population Balance Equations Using the Direct Quadrature Method of Moments”. In: *Journal of Aerosol Science* 36.1 (Jan. 2005), pp. 43–73. DOI: `10.1016/j.jaerosci.2004.07.009`.

[65] J. C. Cheng and R. O. Fox. “Kinetic Modeling of Nanoprecipitation Using CFD Coupled with a Population Balance”. In: *Industrial & Engineering Chemistry Research* 49.21 (Nov. 2010), pp. 10651–10662. DOI: `10.1021/ie100558n`.

[66] H. Barths, C. Hasse, G. Bikas, and N. Peters. “Simulation of Combustion in Direct Injection Diesel Engines Using a Eulerian Particle Flamelet Model”. In: *Proceedings of the Combustion Institute* 28.1 (Jan. 2000), pp. 1161–1168. DOI: `10.1016/s0082-0784(00)80326-4`.

[67] H. Barths, C. Hasse, and N. Peters. "Computational Fluid Dynamics Modelling of Non-Premixed Combustion in Direct Injection Diesel Engines". In: *International Journal of Engine Research* 1.3 (June 2000), pp. 249–267. DOI: `10.1243/1468087001545164`.

[68] G. Nakov et al. "Soot Simulation under Diesel Engine Conditions Using a Flamelet Approach". In: *SAE International Journal of Engines* 2.2 (Nov. 2009), pp. 89–104. DOI: `10.4271/2009-01-2679`.

[69] M. Balthasar, F. Mauss, M. Pfitzner, and A. Mack. "Implementation and Validation of a New Soot Model and Application to Aeroengine Combustors". In: *Journal of Engineering for Gas Turbines and Power* 124.1 (Jan. 2002), pp. 66–74. DOI: `10.1115/1.1377596`.

[70] S. Wu, D. Zhou, and W. Yang. "Implementation of an Efficient Method of Moments for Treatment of Soot Formation and Oxidation Processes in Three-Dimensional Engine Simulations". In: *Applied Energy* 254 (Nov. 2019), p. 113661. DOI: `10.1016/j.apenergy.2019.113661`.

[71] S. Wu, W. Yang, H. Xu, and Y. Jiang. "Investigation of Soot Aggregate Formation and Oxidation in Compression Ignition Engines with a Pseudo Bi-Variate Soot Model". In: *Applied Energy* 253 (Nov. 2019), p. 113609. DOI: `10.1016/j.apenergy.2019.113609`.

[72] S. Wu, S. Yang, K. L. Tay, W. Yang, and M. Jia. "A Hybrid Sectional Moment Projection Method for Discrete Population Balance Dynamics Involving Inception, Growth, Coagulation and Fragmentation". In: *Chemical Engineering Science* 249 (Feb. 2022), p. 117333. DOI: `10.1016/j.ces.2021.117333`.

[73] R. McGraw. "Description of Aerosol Dynamics by the Quadrature Method of Moments". In: *Aerosol Science and Technology* 27.2 (Jan. 1997), pp. 255–265. DOI: `10.1080/02786829708965471`.

[74] M. E. Mueller and H. Pitsch. "LES Model for Sooting Turbulent Nonpremixed Flames". In: *Combustion and Flame* 159.6 (June 2012), pp. 2166–2180. DOI: `10.1016/j.combustflame.2012.02.001`.

[75] S. Salenbauch, C. Hasse, M. Vanni, and D. L. Marchisio. "A Numerically Robust Method of Moments with Number Density Function Reconstruction and Its Application to Soot Formation, Growth and Oxidation". In: *Journal of Aerosol Science* 128 (Feb. 2019), pp. 34–49. DOI: `10.1016/j.jaerosci.2018.11.009`.

[76] F. Ferraro, S. Gierth, S. Salenbauch, W. Han, and C. Hasse. "Soot Particle Size Distribution Reconstruction in a Turbulent Sooting Flame with the Split-Based Extended Quadrature Method of Moments". In: *Physics of Fluids* 34.7 (July 2022), p. 075121. DOI: `10.1063/5.0098382`.

[77] M. E. Mueller and H. Pitsch. “Large Eddy Simulation of Soot Evolution in an Aircraft Combustor”. In: *Physics of Fluids* 25.11 (Nov. 2013), p. 110812. DOI: `10.1063/1.4819347`.

[78] Ö. H. Cokuslu, C. Hasse, K. P. Geigle, and F. Ferraro. “Soot Prediction in a Model Aero-Engine Combustor Using a Quadrature-based Method of Moments”. In: *AIAA SCITECH 2022 Forum*. San Diego, CA & Virtual: American Institute of Aeronautics and Astronautics, Jan. 2022. DOI: `10.2514/6.2022-1446`.

[79] D. L. Marchisio and R. O. Fox. *Computational Models for Polydisperse Particulate and Multiphase Systems*. Cambridge: Cambridge University Press, 2013. DOI: `10.1017/CBO9781139016599`.

[80] W. Gautschi. *Orthogonal Polynomials Computation and Approximation*. Vol. 39. Oxford University Press, 2008.

[81] M. Balthasar and M. Kraft. “A Stochastic Approach to Calculate the Particle Size Distribution Function of Soot Particles in Laminar Premixed Flames”. In: *Combustion and Flame* 133.3 (May 2003), pp. 289–298. DOI: `10.1016/S0010-2180(03)00003-8`.

[82] J. Appel, H. Bockhorn, and M. Frenklach. “Kinetic Modeling of Soot Formation with Detailed Chemistry and Physics: Laminar Premixed Flames of C2 Hydrocarbons”. In: *Combustion and Flame* 121.1-2 (Apr. 2000), pp. 122–136. DOI: `10.1016/S0010-2180(99)00135-2`.

[83] M. Storch, L. Zigan, M. Wensing, and S. Will. “Systematic Investigation of the Influence of Ethanol Blending on Sooting Combustion in DISI Engines Using High-Speed Imaging and LII”. In: *SAE Technical Papers* 2014-Octob (2014). DOI: `10.4271/2014-01-2617`.

[84] M. Storch, F. Hinrichsen, M. Wensing, S. Will, and L. Zigan. “The Effect of Ethanol Blending on Mixture Formation, Combustion and Soot Emission Studied in an Optical DISI Engine”. In: *Applied Energy* 156 (Oct. 2015), pp. 783–792. DOI: `10.1016/j.apenergy.2015.06.030`.

[85] M. Storch, S. Erdenkäufer, M. Wensing, S. Will, and L. Zigan. “The Effect of Ethanol Blending on Combustion and Soot Formation in an Optical DISI Engine Using High-speed Imaging”. In: *Energy Procedia* 66 (2015), pp. 77–80. DOI: `10.1016/j.egypro.2015.02.041`.

[86] M. Storch. “Optische Untersuchungen Zum Einfluss von Biokraftstoffen Auf Die Rußbildung Bei Ottomotorischen Verbrennungsvorgängen”. PhD thesis. Firedrich-Alexander-Universität Erlangen-Nürnberg, 2017.

[87] M. Koegl, B. Hofbeck, S. Will, and L. Zigan. "Investigation of Soot Formation and Oxidation of Ethanol and Butanol Fuel Blends in a DISI Engine at Different Exhaust Gas Recirculation Rates". In: *Applied Energy* 209 (Jan. 2018), pp. 426–434. DOI: `10.1016/j.apenergy.2017.11.034`.

[88] M. Koegl, B. Hofbeck, S. Will, and L. Zigan. "Influence of EGR and Ethanol Blending on Soot Formation in a DISI Engine". In: *Proceedings of the Combustion Institute* (Aug. 2018). DOI: `10.1016/j.proci.2018.07.103`.

[89] B. Choi, S. Choi, and S. Chung. "Soot Formation Characteristics of Gasoline Surrogate Fuels in Counterflow Diffusion Flames". In: *Proceedings of the Combustion Institute* 33.1 (2011), pp. 609–616. DOI: `10.1016/j.proci.2010.06.067`.

[90] M. Storch, M. Koegl, M. Altenhoff, S. Will, and L. Zigan. "Investigation of Soot Formation of Spark-Ignited Ethanol-Blended Gasoline Sprays with Single- and Multi-Component Base Fuels". In: *Applied Energy* 181 (2016), pp. 278–287. DOI: `10.1016/j.apenergy.2016.08.059`.

[91] ANSYS Inc. *IC Engine Simulations with ANSYS CFX and ANSYS ICEM CFD: Setup Documentation, Release 15, Version2.3*. 2013.

[92] S. Buhl, D. Hain, F. Hartmann, and C. Hasse. "A Comparative Study of Intake and Exhaust Port Modeling Strategies for Scale-Resolving Engine Simulations". In: *International Journal of Engine Research* 19.3 (May 2018), pp. 282–292. DOI: `10.1177/1468087417707452`.

[93] Gamma Technologies. *GT-SUITE Engine Performance Application Manual Version 2018*. 2017.

[94] G. Woschni. "A Universally Applicable Equation for the Instantaneous Heat Transfer Coefficient in the Internal Combustion Engine". In: *National Fuels and Lubricants, Powerplants, Transportation Meetings*. Feb. 1967, p. 670931. DOI: `10.4271/670931`.

[95] S. Neumann. "3D CFD Simulation of Spray and Mixture Formation in Direct-Injection Gasoline Engines". MA thesis. Technische Universität Bergakademie Freiberg, 2012.

[96] D. Hain. "Investigation of Soot Formation Processes in DISI Engines Using Ethanol-based Fuels". MA thesis. Technische Universität Bergakademie Freiberg, 2015.

[97] D. Linse, B. Durst, C. Hasse, S. Toninel, T. Frank, and H. Forkel. "Simulating Combustion in Spark Ignition Engines". In: *4th European Automotive Simulation Conference*. 2009.

[98] C. Hasse, V. Sohm, and B. Durst. "Numerical Investigation of Cyclic Variations in Gasoline Engines Using a Hybrid URANS/LES Modeling Approach". In: *Computers & Fluids* 39.1 (Jan. 2010), pp. 25–48. DOI: `10.1016/j.compfluid.2009.07.001`.

[99] C. Hasse. “Scale-Resolving Simulations in Engine Combustion Process Design Based on a Systematic Approach for Model Development”. In: *International Journal of Engine Research* 17.1 (Aug. 2015), pp. 44–62. DOI: `10.1177/1468087415597842`.

[100] S. Buhl, F. Gleiss, M. Köhler, F. Hartmann, D. Messig, C. Brücker, and C. Hasse. “A Combined Numerical and Experimental Study of the 3D Tumble Structure and Piston Boundary Layer Development During the Intake Stroke of a Gasoline Engine”. In: *Flow, Turbulence and Combustion* 98.2 (Mar. 2017), pp. 579–600. DOI: `10.1007/s10494-016-9754-1`.

[101] S. Salenbauch, M. Storch, D. Hain, S. Will, M. Wensing, C. Hasse, and L. Zigan. “Experimental and Numerical Investigation on the Effect of Ethanol-Based Fuel Mixtures on Soot Formation in Gasoline Direct-Injection Engines”. In: *15th Conference "The Working Process of the Internal Combustion Engine"*. 2016.

[102] J. Reusch. “3D CFD Simulation Der Lokalen Partikelbildung in Einem Direkteinspritzenden Ottomotor”. MA thesis. Technische Universität Darmstadt, 2019.